TU UB
Die approbierte Originalversion dieser Diplom-/Masterarbeit ist in der Hauptbibliothek der Technischen Universität Wien aufgestellt und zugänglich.
http://www.ub.tuwien.ac.at
TU UB WIEN Universitätsbibliothek
The approved original version of this diploma or master thesis is available at the main library of the Vienna University of Technology.
http://www.ub.tuwien.ac.at/eng

Diplomarbeit

Investigation of Surface Oxidation of III-N Materials by AES

ausgeführt zum Zwecke der Erlangung des akademischen Grades eines Master of Science am

E 134 - Institut für Angewandte Physik

in Kooperation mit der

Infineon Technologies Austria AG

unter der Anleitung von

ao.Univ.-Prof. Dr.techn. Wolfgang WERNER
und
Mag. Maria REINER, Dr. Clemens OSTERMAIER

erstellt an der

Technische Universität Wien
Fakultät für Technische Physik von

Christian KOLLER
0927161
Zwettler Straße 15
3931 Schweiggers

Wien, am 08.05.2015

Abstract

III-N materials such as gallium nitride (GaN) have gained great attention since the 1990s, mostly due to their importance for optoelectronics. GaN-based materials enabled the fabrication of high-efficiency blue light-emitting diodes which has been honored with the 2014 Nobel Prize in physics. The combination of superior physical properties such as a wide band gap and high electrical breakdown field with high electron saturation velocity makes it further interesting for high-power and high-temperature electronics. Combining GaN with the alloy aluminium gallium nitride ($Al_xGa_{1-x}N$) enables the fabrication of AlGaN/GaN heterostructures that are used for high-electron-mobility transistors (HEMTs). One common problem in these devices is that the AlGaN barrier, even though it has a wide band gap, needs additional passivation in order to suppress parasitic gate leakage current. Passivation by deposition of dielectrics causes high interface state densities and as a consequence dynamic effects such as a threshold voltage drift. Therefore, the usage of directly oxidized layers is considered. Their oxide/semiconductor interface is never exposed to any environment, inhibiting contamination and resulting in less interface states. However, these oxide layers exhibit inhomogeneous oxidation which causes rough surfaces and interfaces.

The purpose of this thesis is to reveal the origin of this high inhomogeneity. Therefore systematic investigation of the oxidation of GaN and AlGaN is performed with a focus on the early stages of growth. The dependence on different oxidation parameters is point of interest as well as the choice of the oxidation technique.

Experimental data show preferred oxidation at threading dislocation sites for thermal oxidation above 800 °C to be the origin of the high interface roughness. Annealing in N_2 atmosphere exhibits that also decomposition is favored at these chemically reactive spots. Therefore oxidation is suggested to be enhanced at dislocation sites by the decomposition of GaN and the subsequent oxidation of the remaining liquid Ga.

An oxide growth model that considers the enhanced oxidation rate at threading dislocations is proposed and can explain the highly nonlinear oxide growth, observed in early stages. This is supposed to end as oxidic craters are coalescing laterally and the overall oxidation rate is eventually solely determined by the decomposition enhanced oxidation rate at dislocations.

Analysis is predominantly performed by Auger electron spectroscopy (AES), which is predestinated for flat layers of well-known stable materials with similar sputter rates and information depths. As oxidized GaN layers do not show any of these features, interpretation of the gained data is challenging. Determination and comparison of sputter rates for GaN and its oxide Ga_2O_3 exhibits great differences. This causes along with the favored sputtering of N over Ga within the GaN crystal severe artifacts in AES depth profiles. Further artifacts originate from the large mismatch in information depths between N and Ga as well as surface charging due to sputtering and electron bombardment.

Kurzfassung

III-N Materialien wie Galliumnitrid (GaN) erregen, vorwiegend aufgrund ihrer außerordentlichen Relevanz in der Optoelektronik, seit den 1990ern verstärkt Aufmerksamkeit. GaN-basierte Materialien ermöglichten die Herstellung von hocheffizienten blauen Lichtdioden, was 2014 mit der Verleihung des Nobelpreises in Physik honoriert wurde. Die hervorragenden physikalischen Eigenschaften wie die große Bandlücke und das hohe kritische elektrische Feld mit der hohen Elektronensättigungsgeschwindigkeit sind zudem von Interesse für Hochleistungs- und Hochtemperaturelektronik. Die Kombination von GaN mit der Legierung Aluminiumgalliumnitrid ($Al_xGa_{1-x}N$) ermöglicht AlGaN/GaN Heterostrukturen, die in $high-electron-mobility\ transistors$ (HEMTs, dt. »Transistoren mit hoher Elektronenbeweglichkeit«) Verwendung finden. Ein bekanntes Problem in diesen Bauteilen ist, dass trotz der großen Bandlücke der AlGaN-Barriere zusätzliche Passivierung notwendig ist um den parasitären Gate-Leckstrom einzudämmen. Die Passivierung durch Abscheiden von Dielektrika verursacht hierbei hohe Grenzflächenzustandsdichten, was in weiterer Folge zu dynamischen Effekten wie einem Driften der Einsatzspannung führt. Aus diesem Grund wird der Einsatz von direkt oxidierten Schichten in Erwägung gezogen. Deren Oxid/Halbleiter-Grenzfläche ist zu keinem Zeitpunkt der Umwelt ausgesetzt, sodass Kontamination verhindert wird, was in einer geringeren Anzahl von Grenzflächenzuständen resultiert. Nichtsdestotrotz weisen diese Oxidschichten aufgrund von inhomogener Oxidation raue Oberflächen und Grenzflächen auf.

Ziel dieser Arbeit ist, die Ursache für die hohe Inhomogenität herauszufinden. Dafür wird die Oxidation von GaN und AlGaN systematisch untersucht, wobei der Fokus auf das Frühstadium des Oxidwachstums gelegt wird. Weiters ist die Abhängigkeit von verschiedenen Oxidationsparametern sowie die Wahl der Oxidationsmethode von Interesse.

Experimentelle Daten für Oxidation über 800 °C zeigen, dass die Ursache für die hohe Rauheit der Grenzfläche die bevorzugte Oxidation an Versetzungslinien ist. Beim Tempern in N_2-Atmosphäre wird ebenfalls bevorzugte Zersetzung an diesen chemisch reaktiven Stellen festgestellt. Dies legt den Schluss nahe, dass die erhöhte Oxidation an Versetzungsstellen durch die Zersetzung von GaN und die anschließende Oxidation des verbleibenden flüssigen Galliums verursacht wird. Es wird ein Oxidwachstumsmodell vorgeschlagen, das die erhöhte Oxidationsrate an Versetzungslinien berücksichtigt und dadurch das beobachtete, höchst nichtlineare Oxidwachstum im Frühstadium beschreibt. Es wird vermutet, dass sich dieses Verhalten durch das laterale Zusammenwachsen von Oxidkratern ändert und die Oxidationsrate der Gesamtstruktur sodann ausschließlich durch die zersetzungsbedingt erhöhte Oxidationsrate an Versetzungen bestimmt wird.

Die Analyse basiert zum Großteil auf Augerelektronenspektroskopie (AES), welche prädestiniert ist für die Untersuchung von flachen Schichten aus wohlbekannten stabilen Materialien mit ähnlichen Sputter-Raten und Informationstiefen. Da oxidierte GaN-Schichten keine dieser Eigenschaften aufweisen, stellt die Interpretation der gewonnenen Daten eine große

Herausforderung dar. Die Bestimmung und der Vergleich der Sputter-Raten zwischen GaN und dessen Oxid Ga_2O_3 zeigt große Unterschiede, die gemeinsam mit dem bevorzugten Sputtern von N gegenüber Ga innerhalb des Kristalls massive Artefakte in AES-Tiefenprofilen hervorrufen. Weitere Artefakte stammen von der großen Diskrepanz zwischen den Informationstiefen für N und Ga sowie der Aufladung der Oberfläche durch Sputtern und Elektronenbeschuss.

Contents

1 Introduction **1**
1.1 III-N Materials . . . 1
1.1.1 Crystal Structure . . . 1
1.1.2 Polarization . . . 2
1.1.3 2DEG Formation . . . 4
1.1.4 Surface Donor States . . . 4
1.2 III-N based Transistors: HEMTs . . . 5
1.2.1 Advantages of GaN over other Semiconductors . . . 5
1.2.2 Possible Applications . . . 7
1.2.3 III-N Transistors: HEMTs . . . 7
1.2.4 Problems concerning HEMTs . . . 9
1.2.5 Natively grown Gate Oxides . . . 9
1.3 Objectives of this Thesis . . . 10
1.4 Outline of this Thesis . . . 10

2 Theory **12**
2.1 Sample Preparation . . . 12
2.1.1 Substrate . . . 12
2.1.2 Epitaxy . . . 13
2.1.3 Surface Contamination . . . 14
2.2 GaN Surface Treatment . . . 15
2.2.1 Oxidation . . . 15
2.2.2 Decomposition . . . 20
2.2.3 Surface Cleaning and Oxide Removal . . . 22
2.3 Analysis . . . 22
2.3.1 AES Analysis . . . 22
2.3.2 other Analysis Methods . . . 26

3 Experimental **28**
3.1 Sample Preparation . . . 28
3.1.1 Oxidation . . . 28
3.1.2 Oxide Removal . . . 29
3.2 Surface sensitive Analysis by AES . . . 29
3.3 other Analysis Methods . . . 30

4 Results **31**
4.1 Raw Sample . . . 31
4.2 Surface Treatments . . . 32
4.2.1 Oxidation . . . 32
4.2.2 Decomposition . . . 52
4.2.3 Oxide Removal/Etching Artifacts . . . 56
4.3 Analysis . . . 56
4.3.1 AES Analyis . . . 58
4.3.2 EDX Analysis . . . 67
4.3.3 AFM . . . 68

4.3.4 Layer Thickness Measurements 69

5 Conclusion **71**

5.1 Outlook 72

1 Introduction

The superior material properties of gallium nitride (GaN) such as the wide band gap (3.4 eV), high electrical breakdown field (3.3 MV/cm) and electron saturation velocity ($3{\cdot}10^7$ cm/s) are known for decades as are techniques to grow GaN crystals [Ost07]. However, electronic device manufacturing was inhibited by growth difficulties for a long time. As these growth difficulties could be solved, GaN devices led to a great breakthrough in optoelectronics. The fabrication of high-efficiency blue light-emitting diodes (LED) started in 1991, due to its technical relevance this was awarded with the 2014 Nobel Prize in physics. GaN forms continuous alloys with aluminum nitride (AlN) and indium nitride (InN) so that due to the wide range of thus available band gaps (1.9-6.2 eV) the entire spectrum from red to deep ultraviolet can be covered.

However, the superior material properties of GaN are not only of interest for optoelectronics but also for other electronic devices such as transistors. In 1993 the first GaN-based transistor was manufactured but there are still serious issues to solve prior to a broad market introduction and acceptance. One issue, concerning the reliability, is the fabrication of high-quality gate dielectrics. For this purpose, natively grown oxides on (Al)GaN are desired but show low quality. This is the initial situation for the present thesis. In order to enhance the quality of these oxides, general understanding of the nature of the oxidation process and the origin for the low oxide quality is required.

This chapter gives an introduction of the peculiarities of GaN, which are responsible for the superiority over well-established semiconductors. Transistors based on GaN-based materials are introduced and still unsolved problems pointed out. This leads to the objectives and an outline of this thesis.

1.1 III-N Materials

1.1.1 Crystal Structure

Group III-N materials, which are commonly referred to as III-N materials, consist of a metal-ion of the group 13 in the periodic table (which is colloquially also referred to as a group III ion) and a nitrogen atom. For the metal gallium, aluminum and for optoelectronic devices also indium as well as alloys are commonly used. The most relevant alloy is $Al_xGa_{1-x}N$, which is, independent of the Al content x referred to as "AlGaN".

III-N materials can exist in the cubic rock-salt, cubic Zincblende or the hexagonal wurtzite crystal structure. The cubic structures require more sophisticated fabrication techniques and do not exhibit spontaneous polarization, contrary to wurtzite structures. As spontaneous polarization is desired for many applications such as transistors, standard applications use wurtzite crystals. Wurtzite crystal structures consist of two interlacing hexagonal close packed (hcp) sublattices that are shifted against each other (fig. 1.1). For III-N materials

one is occupied by group 13 metal ions and one by N ions.

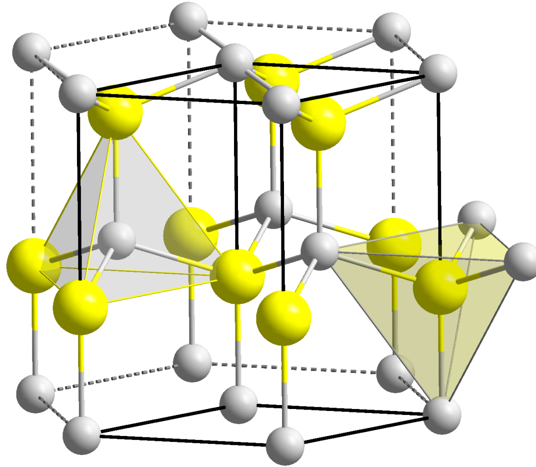

Figure 1.1: III-N wurtzite crystal structure [Wik14] (grey spheres: Ga^{3+}; yellow spheres: N^{3-})

The large differences in electronegativity between N and group 13 metals make N become partly negatively charged and the metal positively. This induces a mixed binding mechanism with covalent and ionic components with very high binding energies per atom (GaN: 9.8 eV/atom, AlN: 11.5 eV/atom). The high binding energy results in the high chemical and thermal stability of III-N materials [Ost07], its wide band gap (3.4 eV) as well as its low intrinsic charge carrier concentration ($1.9 \cdot 10^{-10}$ cm^{-3}), high thermal conductivity and high breakdown field (3.3 MV/cm) [Hen14].

1.1.2 Polarization

The electronegativity difference induces microscopic electrical dipole moments. Since in III-N crystals the bonding length between the metal ion and the N ion in the [0001] direction is slightly larger than for the other three, dipole moments do not cancel out but sum up. This leads to macroscopic polarization in z-direction, which is referred to as spontaneous polarization. For many sequences of atomic layers, polarization within the material is negligible, the charges occur at surfaces and interfaces, if the adjacent layers show different polarization.

As the electronegativity difference of Al and N is far higher than between Ga and N, AlN shows higher polarization and charge accumulates at AlGaN/GaN interfaces (fig. 1.2).

Independent of spontaneous polarization a second polarization mechanism is observed, referred to as piezoelectric polarization. It also originates from distorted bonding lengths, causing electrical dipole moments. Here the bonding length distortion is induced by mechanical stress, originating e.g. from the pseudomorphical growth of AlGaN on GaN. Due to the different lattice constants of AlN and GaN, the pseudomorphically grown AlGaN layer is deformed in a- and c-direction. As shown in fig. 1.2, GaN is usually grown on substrates with different lattice constants. To avoid undesired piezoelectric polarization in the GaN

layer, sophisticated growth design, consisting of many layers, is required in order to provide a relaxed GaN layer on top.

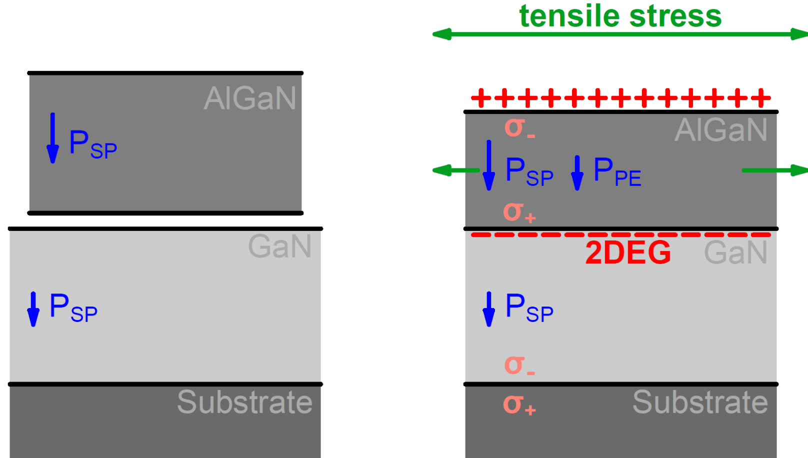

Figure 1.2: demonstration of the origins and effects of spontaneous and piezoelectric polarization in an exemplary III-N stack [Hen14]

In general, wurtzite crystals can be produced in two different forms regarding the order of the interpenetrating sublattices (fig. 1.3). For III-N materials it is differentiated between metal-phase and N-phase. Regardless of the phase, piezoelectric polarization in AlGaN layers on top of GaN leads to polarization in [$000\bar{1}$] direction. For N-phase structures polarization is directed along [0001], contrary to the [$000\bar{1}$] direction in metal-phase structures. Thus, the sum of both types of polarization is enhanced in metal-phase structures (fig. 1.2), which is desirable for its use in transistors.

III-N surfaces are always terminated by metal layers since N adlayers are not stable. As shown in fig. 1.3, for N-phase structures Ga surface atoms have three remaining unsaturated bonds, while they have only one in Ga-phase structures. This makes metal-phase surfaces smoother and more resistant against oxidation and wet etching [Ost07]. For standard applications only metal-phase structures are considered.

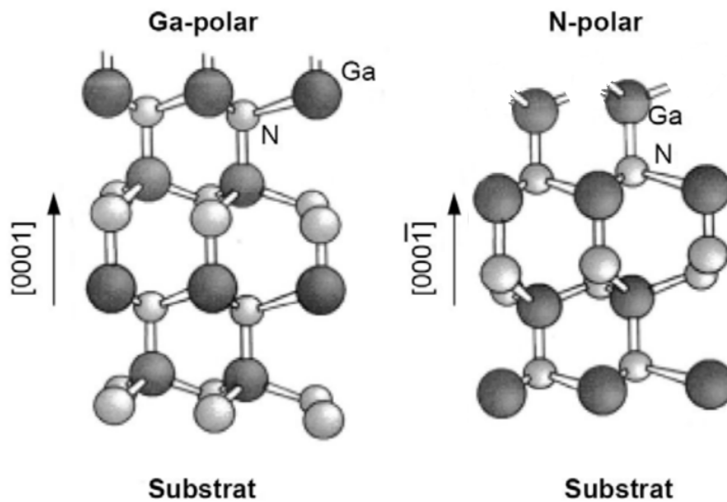

Figure 1.3: Ga ([0001]) and N phase ([$000\bar{1}$]) GaN wurtzite crystal structures [Ost07]

1.1.3 2DEG Formation

Polarization induces an electric field within III-N materials that adjusts the band diagram as shown in fig. 1.4. For idealistic freestanding metal-phase III-N materials or in general polar materials, with increasing layer thickness the valence band maximum VBM at the top surface rises until it exceeds the Fermi level E_F (fig. 1.4). Electrons migrate then from the top surface to the bottom, generating a hole channel at the top surface and an electron channel at the bottom, compensating the polarization charges. The critical layer thickness for the emerging depends on the band gap and is approximately 10 nm for GaN [WJ07].

For non-idealistic, real materials additional surface states and states in the bulk within the band gap exist so that dipole formation occurs at even thinner layers. The valence band maximum does not have to reach E_F, but only the level of surface donor states at the surface.

In analogy to freestanding III-N materials, for idealistic AlGaN/GaN heterostructures with AlGaN layers exceeding a critical thickness, a hole and electron channel is formed. The electron channel is therefore located at the AlGaN/GaN interface. As electrons can move almost freely within the spatially two-dimensional electron channel, it is referred to as two-dimensional electron gas (2DEG). For non-idealistic materials, electrons for the 2DEG originate from surface donor states.

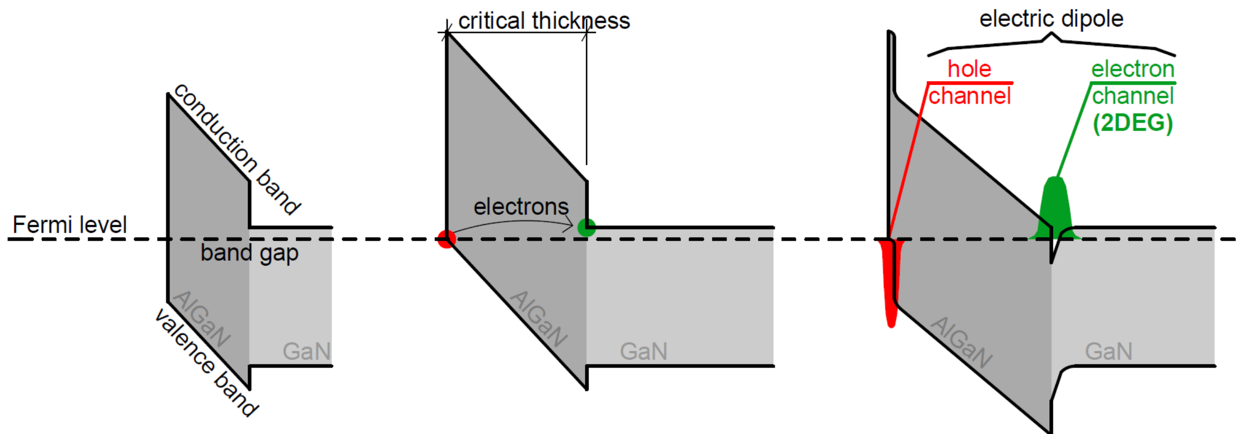

Figure 1.4: schematic band diagram of an idealistic AlGaN layer on top of GaN: formation of an electric dipole for layer thicknesses exceeding critical values [WJ07] [Lag14]

1.1.4 Surface Donor States

When the 2DEG at the interface was first introduced by Khan et al. [KVHKO91] in 1991, no knowledge existed about the origin of its electrons. There were many theories discussed until 2000, when Ibbetson et al. [IFN+00] proposed surface donor states to act as electron source, which is now widely accepted by the community.

However, this does not reveal where these surface donor states originate from. A promising way to gain knowledge about their origin is the observation of surface barrier heights SBH,

which is the difference of the conduction band minimum CBM and EF. Therefore the distribution of surface states can be obtained; fig. 1.5 schematically shows two extreme samples of distributions. By comparison of these heights with surface states for potential surface donor state sources, their origin can be found.

Although the exact distribution of surface donor states is widely discussed [GMC+10] [KRL+02] [DFN06a], most groups have accepted oxygen as a highly potential candidate for the electron source.

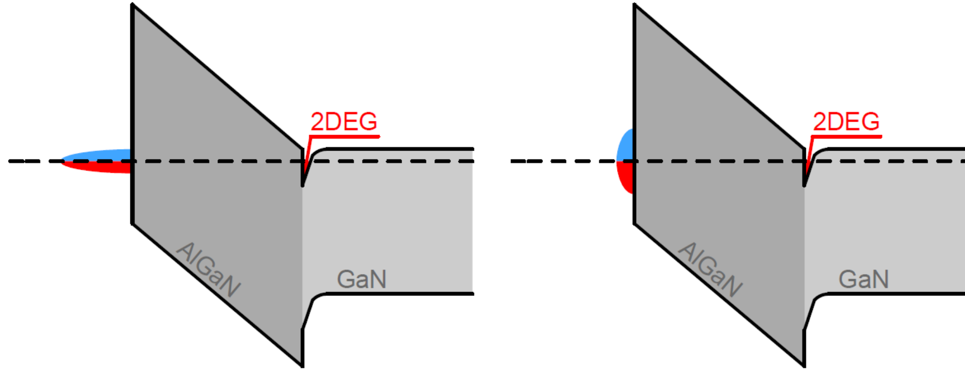

Figure 1.5: schematic band diagram for different surface donor states distributions: high density of states in a narrow energy range (left) vs. low density of states in a broad energy range (right) [GMC+10]

1.2 III-N based Transistors: HEMTs

1.2.1 Advantages of GaN over other Semiconductors

Most of the advantageous macroscopic material properties of III-N materials originate from its microscopic properties, especially the short, strong bonding due to the high electronegativity difference of group 13 and N atoms. This leads to macroscopic properties such as the wide band gap and to high chemical stability. The wide band gap enables high critical electric fields and low intrinsic carrier generation, suppressing leakage current at high temperatures. Combined with the small mass, a large phonon energy is introduced that suppresses lattice scattering and leads to high thermal conductivity and high saturation drift velocity. These material characteristics make III-N materials predestinated for high frequency, high power, high voltage, high temperature and low loss operating devices [Vis11] [Oku06].

The superiority of III-N materials such as GaN over other important wide band gap materials can be extracted from tab. 1.6. GaN as well as silicon carbide (SiC) have larger band gaps than traditional semiconductors such as Si and GaAs, resulting in higher critical electric fields. High current and high frequency operation require high electron mobility and high saturation velocity, where GaAs shows the largest values. Especially the modern wide band gap materials GaN and SiC are inferior with electron mobility values of only a fraction of GaAs. However, due to the polarization induced 2DEG in III-N devices the mobility is enhanced in this electron channel, being the main advantage of GaN over SiC. The thermal conductivity of SiC on the other hand is superior to all other listed materials, especially

GaAs conducts heat very badly, leading to faster device degradation at high temperatures, important for high power applications. Even though GaN does not have any single exceptional property, their combination results in the superior behavior that is further observable in various figures of merit (FOM) as shown in tab. 1.7 [Vis11] [Oku06].

material	Si	6H-SiC	GaN	GaAs
band gap [eV]	1.1	3.0	3.4	1.4
critical electric field [MV/cm]	0.3	2.4	3.3	0.4
rel. dielectric constant []	11.8	9.7	9.0	12.8
electron mobility [$cm^{-2}V^{-1}s^{-1}$]	1 400	400	900, 2 000*	8 500, 10 000*
saturated drift velocity [10^7 cm/s]	1.0	2.0	2.5	2.0
thermal conductivity [W $cm^{-1}K^{-1}$]	1.5	4.5	1.3	0.5

Figure 1.6: comparison of material properties between wide band gap materials such as SiC and GaN with traditional semiconductors such as Si and GaAs (* values within the 2DEG) [Oku06]

A FOM combines most relevant material properties in order to compare different materials regarding their ability for use in a specific application field. For reasons of clarity and comprehensibility all values are normalized to the Si value. More details about the calculation and meaningfulness of these FOM are found in [Bal89]. Johnson's FOM expresses the capability of a material for high-frequency-, Keyes's FOM for high-temperature- and the two Baliga's FOM for high-power-handling at low and at high frequencies [Vis11]. From this point of view SiC is competitive to GaN, but SiC has some practical disadvantages such as its high intrinsic material costs, its limited size and other fabrication related issues [Vis11].

material	Si	6H-SiC	GaN	GaAs
Johnson	1	260	760	7.1
Keyes	1	4.7	1.6	0.5
Baliga (low frequency)	1	110	60	15.6
Baliga (high frequency)	1	16.9	77.8	10.8

Figure 1.7: comparison of various FOMs of wide band gap materials such as SiC and GaN with traditional semiconductors such as Si and GaAs (FOMs are normalized to values for Si) [Oku06]

Another important parameter is the specific on-resistance ($R_{DS,on}$), which is desired to be as small as possible, but is in general linearly proportional to the breakdown voltage (V_{BD}), which is wanted as high as possible. Therefore either a reasonable compromise has to be made or by using advanced device concepts such as superjunction MOSFETs or IGBTs this material characteristic limitation can be exceeded as seen in fig. 1.8. Another possibility is the use of superior materials such as SiC or GaN, whereby GaN shows best material characteristics [Lag14] [HPE10].

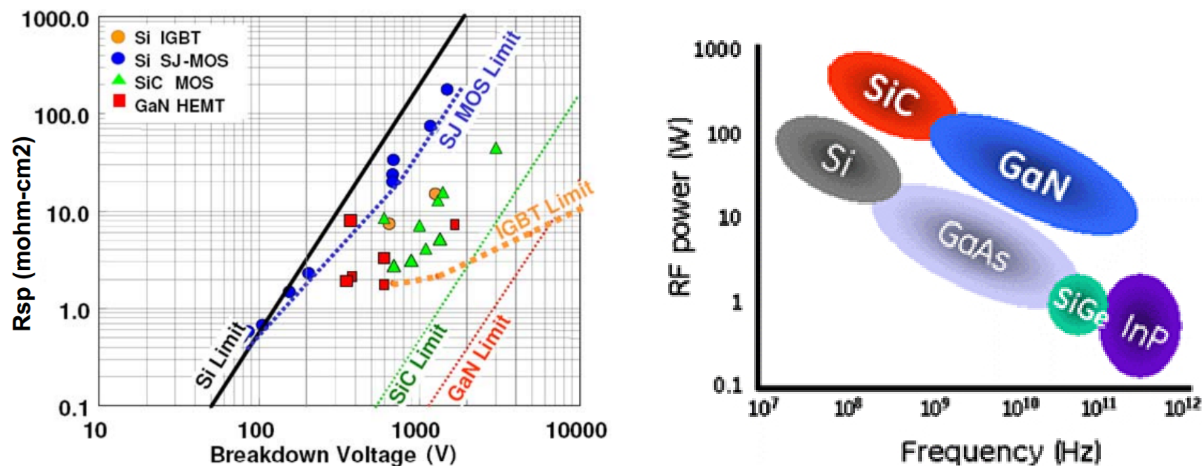

Figure 1.8: demonstration of the superiority of GaN over other semiconductors for high power, high frequency applications due to a) the better R_{sp}/V_{BD}-characteristic (R_{sp}...specific on-resistance R_{DSon}) [HPE10] and b) the combination of high RF output power and frequency [Hon14]

1.2.2 Possible Applications

GaN and GaN-based materials are already well-established in the optoelectronic industry, predominantly for LEDs and lasers. Due to their exceptional material properties, the industrial GaN technology market is also expanding into power electronics, high power RF applications and harsh environment electronics [Hon14]. Approximately 15 years ago, the first GaN devices for RF applications were developed where they can replace Si transistors in some selected systems [Bri08]. Especially for the combination of high frequencies and high output power, GaN is superior over other semiconductors as demonstrated in fig. 1.8b). Since then, GaN devices are also diffusing into power electronics. Over the last 40 years, power electronics have been dominated by Si devices such as MOSFET, GTO and IGBT, but due to the superior material properties of GaN, some Si devices could be replaced by GaN. Some potential fields for GaN devices within the power electronics segment are shown in fig. 1.9.

1.2.3 III-N Transistors: HEMTs

The introduction of the 2DEG between an AlGaN and GaN layer can be used to fabricate high electron mobility transistors (HEMTs). A schematic HEMT is depictured in fig. 1.10. Source and gate are contacted directly to the 2DEG, while the gate is separated by the AlGaN layer. Simple HEMT structures are "normally-on", implying that without applying gate bias the device is "switched on" and current can flow between source and gate. By applying negative gate bias the 2DEG gets depleted and current flow is inhibited.

All essential parts for AlGaN/ HEMTs are depictured in fig. 1.10:

First of all, due to the very challenging and cost-intensive procedure of producing high-quality monocrystalline GaN wafers, GaN is commonly epitaxially grown on another suitable substrate material. The main purpose of the GaN buffer is to provide the polarization charge.

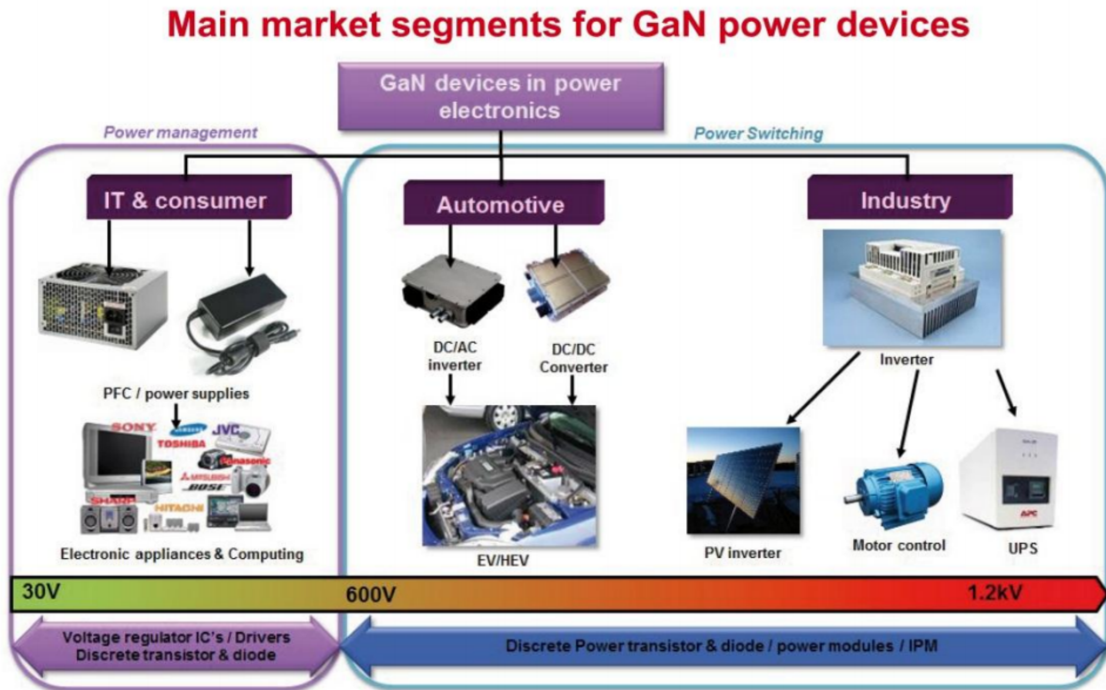

Figure 1.9: potential application fields for GaN devices in power electronics [Hon14]

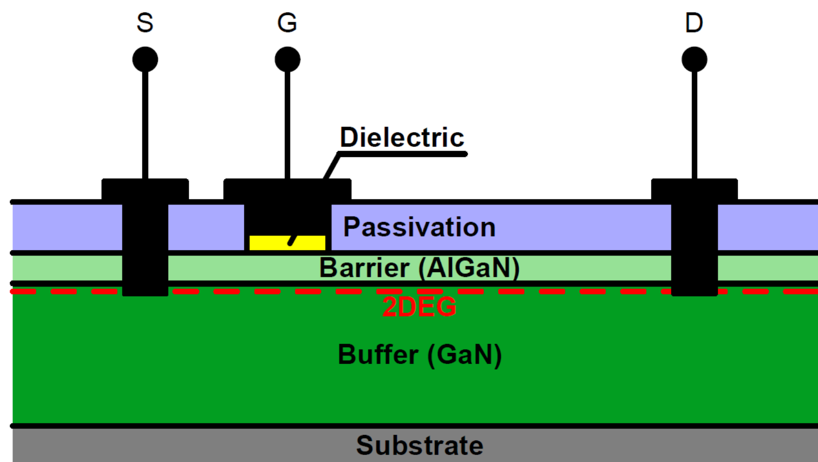

Figure 1.10: schematic structure of an AlGaN/GaN-MIS-HEMT

Besides it has some additional function. It relaxes the high field strength under the drain and gate contacts, reduces the dislocation density and in general the mechanical stress due to the lattice mismatch with the substrate. Furthermore, it suppresses current leakage between the substrate and the 2DEG as well as between gate and drain in off-state operation in order to increase the breakdown and degradation behavior of the HEMT [Hen14]. Due to its intrinsic polarization the AlGaN layer enables the formation of the 2DEG at its interface to the GaN buffer.

The contacts for source, gate and drain are carried out by etching and metal deposition as shown in fig. 1.10.

As demonstrated in fig. 1.2, maintaining positive surface charge is essential for the existence of the 2DEG. In order to prevent neutralization of these positively charged surface states by trapped electrons, an additional passivation layer is deposited on the AlGaN layer [Vet00] [Jar06].

If an electric field is applied, electrons can leak from the gate metal and get trapped in the gate stack. This results in reduced surface charge and thus reduced 2DEG charge and channel current. High-quality passivation can also prevent this effect. The commonly used material is Si_3N_4 [LM12].

1.2.4 Problems concerning HEMTs

First HEMTs by Khan et al. [AKBKO93] were carried out with a direct gate metal/AlGaN contact, referred to as Schottky contact. These Schottky contacts exhibit low Schottky barrier heights and/or poor interface quality can introduce parasitic gate leakage current and low breakdown voltage [LM12]. In order to solve these problems, dielectrics can be deposited between the gate metal and the AlGaN barrier as shown in fig. 1.10. Such structures are referred to as metal-insulator-semiconductor (MIS)-HEMT. Deposited materials have to form uniform layers with large band gaps and a suitable band alignment. Some frequently reported dielectrics are e.g. SiO_2, Si_3N_4, Al_2O_3, La_2O_3, Ga_2O_3, ZrO_2 and HfO_2 [LM12] [Lag14]. Deposition is predominantly performed by atomic layer deposition ALD. All these materials are observed to reduce parasitic gate leakage and show additional advantages such as increased drain current, immunity to current collapse, transconductance and breakdown voltage. However deposited dielectrics also have drawbacks. The dielectric is directly deposited on the AlGaN surface, which exhibits always some amount of contamination. This leads to a high amount of defect states at the dielectric/AlGaN interface, which is further responsible for a tremendous threshold voltage drift due to applying forward gate bias [Lag14]. A possible way to solve this problem is the use of natively grown gate oxides.

1.2.5 Natively grown Gate Oxides

Gallium oxide (Ga_2O_3) is reported to be a potential candidate as dielectric and it cannot only be deposited but also natively grown on GaN. There are different processing methods such as thermal, plasma or anodic oxidation, whereby thermal oxidation is the most simple and therefore desirable form of all. As oxidation partly consumes the initial material, foreign contaminants can be avoided at the interface [OC12], which is desirable in order to significantly reduce interface states. Nakano et al. [NJ03] claim an interface state density

of $5.5 \cdot 10^{10}$ $eV^{-1}cm^{-2}$ for thermally oxidized Ga_2O_3/GaN metal-oxide-semiconductor (MOS) samples compared to $2.2 \cdot 10^{12}$ $eV^{-1}cm^{-2}$ for sputtered SiO_2/GaN MOS samples, Zhou et al. [ZAIS+08] also present a decrease of more than one order of magnitude.

However, natively grown gate oxides show some additional problems. First of all Ga_2O_3 has a band gap of 4.4 eV, but ordered surface oxides are reported to show band gaps similar to GaN with only 3.4 eV [DFN06a]. Even a conduction band offset of 0.5 eV might not be sufficient to suppress gate leakage current effectively; an offset of greater 1 eV is suggested by Long et al. [LM12]. Al_2O_3 is the native oxide of AlN and also a potential candidate for a gate oxide with a sufficient band offset of 2.1 eV [EKN+11]. The oxidation of AlGaN leads to a mixture of Al_2O_3 and Ga_2O_3, but there is also the possibility to oxidize an additionally grown AlN top layer [Lag14].

A further problem concerns the oxidation process, which is reported to be not homogenous. Threading dislocation sites are preferably oxidized, resulting in high roughness of surfaces and interfaces [ZAIS+08] [WDM+00] [OC12] [LLLL06]. The quality of the oxide and especially its interface to the underlying semiconductor is observed to have great effect on the interface state density and electrical properties such as the breakdown characteristic [ZAIS+08] and the voltage threshold drift [Lag14].

1.3 Objectives of this Thesis

The main objective of this thesis is to understand the behavior and physics of oxide growth on III-N materials, in particular on GaN and AlGaN. To exhibit the origin of the high roughness of III-N surfaces and their interfaces with the remaining semiconductor, especially the early stages of growth are of interest. The dependency of oxide growth on various oxidation parameters as well as its correlation with to phenomena such as decomposition, Ga droplet formation and surface and interface roughening are investigated.

A great part of this thesis is dedicated to the analysis of these thin oxidic layers. For this purpose the focus is clearly laid on the usage of Auger electron spectroscopy (AES).

1.4 Outline of this Thesis

Chapter 1 covers the physical background for the superiority of III-N materials over other semiconductors. The polarity of III-N materials enables the fabrication of HEMTs, whereby the role of oxygen for the development of a 2DEG is discussed. The concept of the usage of natively grown oxides as gate oxides, potentially resulting in lower interface state density, is introduced. However, fabricated oxides show low quality which leads to the aim of this thesis; the investigation and understanding of oxide growth, predominantly by AES analysis.

The second chapter provides state-of-the-art knowledge on various relevant fabrication and treatment processes. The fabrication of III-N layers on different substrates is discussed, followed by an introduction of various III-N surface treatments such as oxidation, decomposition and oxide removal. The focus is laid on a literature review of oxide growth with all

its dependencies.

Furthermore the principle of AES is introduced with a focus on obtaining depth information. Since AES is not capable of obtaining all relevant information, supporting analysis methods are briefly introduced.

In chapter 3 relevant experimental setups, manufacturing and process conditions are described in greater detail. Furthermore, the used AES setup is introduced and relevant details for other analysis devices are mentioned.

In chapter 4 all results are presented and discussed. Oxidation is found to preferably take place at threading dislocation sites and therefore, besides a uniform oxide layer, causes large oxidic structures, which result in the obtained high roughness of surfaces and oxide/semiconductor interfaces. An oxide growth model is proposed that considers this issue and can explain the strong nonlinearity in oxidation rate observed in early growth stages. Furthermore, for the analysis of III-N materials some issues have to be considered that cause artifacts for the used analysis techniques. This is discussed in detail with a focus on AES.

Finally, chapter 5 gives summary and conclusion of this thesis and an outlook for future research.

2 Theory

This chapter provides state-of-the-art knowledge on oxidation of GaN and its investigation, predominantly by AES. Furthermore the first section introduces briefly the growth of GaN.

2.1 Sample Preparation

GaN layers for electronic devices are usually epitaxially grown on substrates, but there are various ways to achieve this. There are different substrate materials as well as different epitaxy techniques. The way of manufacturing influences the initial material's properties, which has to be considered in order to compare investigations from different groups.

2.1.1 Substrate

Due to the very high financial effort for synthesizing GaN wafers, GaN is usually grown on substrate wafers of a different material with thermal and mechanical properties close to GaN as shown in tab. 1 [Vis11]. In the early days sapphire (Al_2O_3) has been used most commonly, it is semi-insulating and resisting the high growth temperatures, but a drawback is the very low thermal conductivity, which prohibits high power applications [Vis11]. Silicon carbide (SiC) shows superior material properties but for a far higher financial effort than Al_2O_3. Silicon (Si) is by far the cheapest substrate material. Occurring problems originate from the large lattice mismatch, which leads to a large number of defects as well as the large thermal mismatch, causing wafer bowing or layer cracking, limiting the GaN buffer layer thickness [Vis11]. For its usage as substrate, Si has to be grown in (111) direction, leading to a hexagonal surface symmetry. The c-axis (0001) of GaN then aligns to the (111) Si direction.

substrate	Si (111)	Al2O3	6H-SiC	GaN (0001)
lattice constant a [Å]	3.846	4.758	3.081	3.189
lattice mismatch [%]	-17	-33	3.5	-
thermal expansion coefficient α [10^{-6} K^{-1}]	2.6	7.3	4.5	5.6
thermal expansion mismatch [%]	116	-23	24	-
thermal conductivity κ [W $cm^{-1}K^{-1}$]	1.5	0.5	4.5	1.3
wafer size	2-12"	2-8"	2-6"	2"
price	low	medium	high	very high

Table 1: comparison of relevant substrate properties [Vis11]

2.1.2 Epitaxy

Independent of the substrate, GaN is grown epitaxially on top of it, where in general two different techniques are dominating, more exotic techniques such as hydride vapor phase epitaxy (HVPE) are described in [Mar08] and not further considered. The two common ways to deposit thin films of GaN are molecular beam epitaxy (MBE), which is a physical vapor deposition (PVD) method and metalorganic vapor phase epitaxy (MOCVD), which is a chemical vapor deposition (CVD) method.

MBE (fig. 2.1) is a physical vapor deposition technique in which Knudsen effusion cells can be heated in order to sublimate the containing material and form the gaseous particles to a molecular beam, directed onto the substrate, where they condense and cause epitaxial growth. To ensure that evaporated particles do not interact with any other particles or themselves, MBE is performed in an ultra-high vacuum (UHV) chamber. The UHV condition combined with slow deposition rates allow the best crystal quality in terms of a low impurity concentration with this form of epitaxy [Wik14].

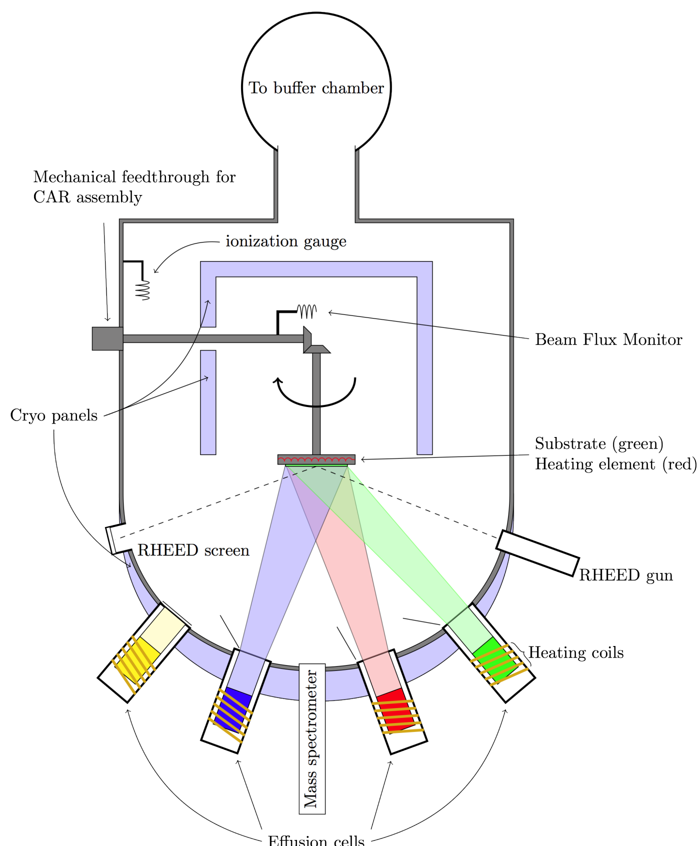

Figure 2.1: schematic MBE-system [Wik14]

The other epitaxy technique is MOCVD, also referred to as metalorganic vapor phase epitaxy (MOVPE). The main difference to MBE is that MOCVD is a chemical vapor deposition method. Since the crystal does not grow by physical deposition but by chemical reactions there is no need of high vacuum, which is usually in a range of 50-250 mbar [Hen14] [Ost07]. This leads to both, the main advantage of this technique because of the simpler setup as

well as to the main disadvantage, the worse crystal quality [Bar14].

For the MOCVD-epitaxy-process (fig. 2.2) first a gaseous metalorganic precursor as well as the substrate is heated to temperatures in a range of about 550 to 1200 °C [Ost07] [Hen14], followed by the injection of the precursor into the reactor chamber. It reaches the surface by convection and diffusion, where some molecules are adsorbed to the substrate by physi- or chemisorption. Due to the high temperature of the substrate the precursor decomposes and the deposited particles migrate by surface diffusion to energetic favored regions which consequently leads to nucleation and island growth. Volatile surface reaction products are desorbed and pumped out of the reaction chamber. More and more atoms are deposited so that in the end a continuous film is created [Bar14].

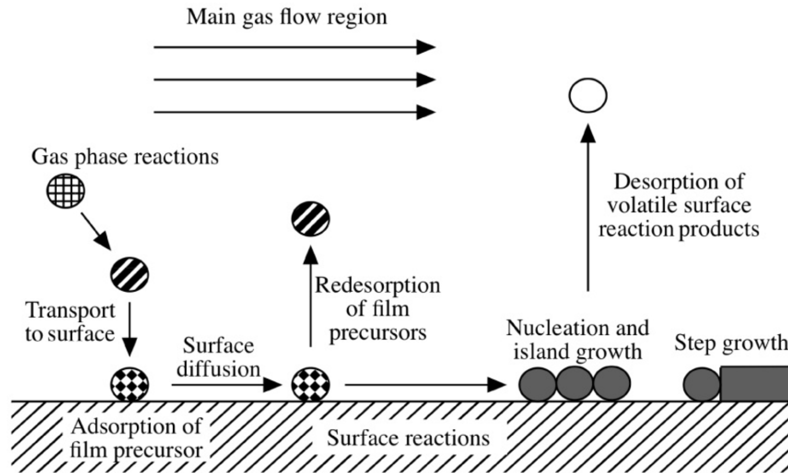

Figure 2.2: scheme of the occuring processes during MOCVD [Bar14]

Precursor materials for Ga are usually Trimethylgallium (TMGa) or Triethylgallium (TEGa), while for N ammonia (NH_3) and for Al Trimethylaluminium (TMAI) are used. As an inert carrier gas, molecular Nitrogen N_2 is predominantly used. The reaction kinetics, atomic contents and growth and sheet parameters can be controlled by varying temperature, pressure, involved gases and their ratios. Thus GaN, AlN and $Al_xGa_{1-x}N$ with arbitrary Al content x can be grown with a typical growth rate of about 1 μm/h [Hen14].

2.1.3 Surface Contamination

The GaN bulk is thermally and chemically very stable due to the high electronegativity difference of Ga and N and the resulting small bonding length and high binding energy. However, at the surface unsaturated surface bonds (dangling bonds) remain. density functional theory (DFT) studies reveal N adatoms to be thermodynamically unstable so that the GaN layer always terminates with a complete Ga surface layer [ZNS99]. Due to the high reactivity of superficial Ga atoms due to their unsaturated surface bonds and the high electronegativity difference between Ga and O, combined with the high amount of O in the atmosphere, exposure of GaN to the atmosphere causes O adsorption. Superficial native oxide layers with thicknesses of about 1 to 20 Å form [WWG99] [EBW+96]. On top of this oxide a thin overlayer of organic and anorganic contamination in a comparable amount is

built [EBW+96]. This is the actual initial provided surface, on which subsequent treatments are performed.

2.2 GaN Surface Treatment

2.2.1 Oxidation

In general the oxidation of III-V-semiconductors is more complex than for Si because one element can diffuse, evaporate or dissolve faster than the other one, causing highly nonuniform oxide layers [Bae03]. In III-N semiconductors N evaporates faster than Ga, resulting in Ga-oxides, whereby also some N-O bonding might occur [KBB+98].

The oxidation reaction for thermal oxidation in O_2 is [JW13] [RTN+00]:

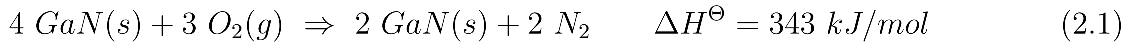

$$4\ GaN(s) + 3\ O_2(g)\ \Rightarrow\ 2\ GaN(s) + 2\ N_2 \qquad \Delta H^{\Theta} = 343\ kJ/mol \tag{2.1}$$

here O_2 originates from the environment and N_2 desorbs from the solid into the gaseous atmosphere, leaving β-Ga_2O_3 behind. For oxidation in different atmospheres the required O atoms can come from other O compounds such as N_2O [OC12], which is also referred to as the oxidizing agent. This may also result in different N compounds being formed after desorption of N, but however, Ga_2O_3 remains.

a) Intrinsic Ga_2O_3

There are five different structural modifications of Ga_2O_3, denoted with Greek letters α to ϵ [ASA96], whereby the β modification is thermodynamically most stable and no other form is found for the oxidation of GaN [ZAIS+08] [OC12]. The oxide has a quite complex monoclinic crystal structure as depicted in fig. 2.3.

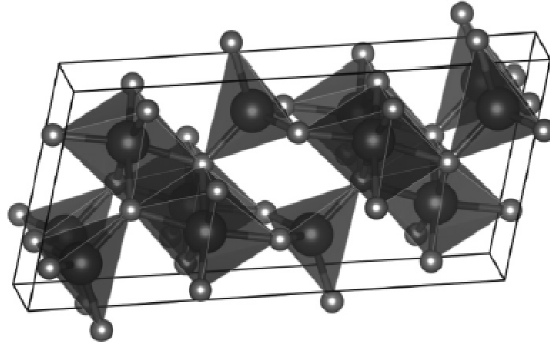

Figure 2.3: unit cell of monoclinic β-Ga_2O_3: dark spheres represent Ga^{3+} and brighter ones O^{2-} ions [JW13]

As chemically shown in fig. 2.4, O^{2-} anions form a slightly distorted fcc structure while Ga^{3+} cations show tetrahedral and octahedral sites [Gel60].

b) Oxide Growth Model

In general there are three thin film epitaxial growth modes. The simplest one is the layer-by-layer growth, also called Frank-van der Merwe growth, and applies for the oxidation of

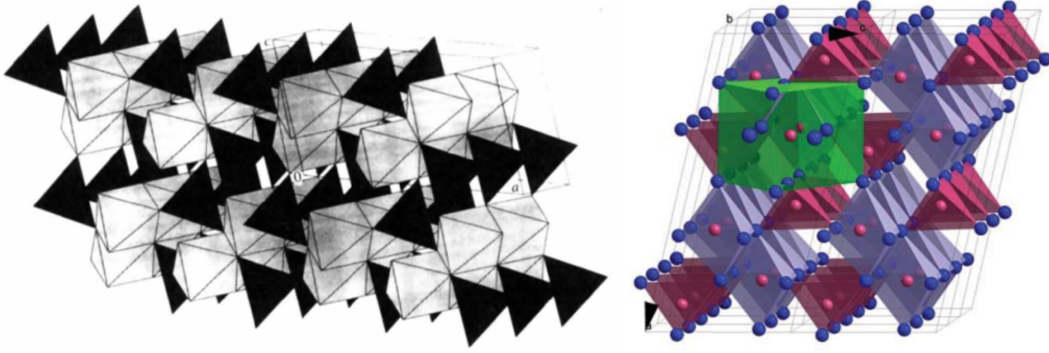

Figure 2.4: Ga_2O_3 unit cell showing that a) Ga^{3+} ions exist in tetrahedral and octahedral coordination [ASA96] and b) O^{2-} ions form a distorted fcc crystal structure (green) [KM03]

Si. On the other hand there is the Volmer-Weber growth, where islands occur and grow on the surface. For GaN oxidation a third mode, called Stranski-Krastanov (SK) or layer-plus-island growth is observed. This is a combination of the former two, where first a thin film grows layer-by-layer up to a critical thickness and continues by nucleation and coalescence of islands [WDM+00].

Oxide layer growth starts with an oxynitride layer ($Ga_{x+2}N_{3x}O_{3-3x}$) of a thickness of 1.5-3.0 nm [WDM+00]. On top of this uniform layer, discrete oxide crystallites with a monoclinic Ga_2O_3 crystal structure form [ZAIS+08]. These crystallites form hillocks, which are preferentially located at dislocation sites and grow in size as well as in number with ongoing oxidation. They eventually impinge to a uniform layer with serious roughness [WDM+00] [ZAIS+08].

The oxide growth rate is determined by two different processes which are the actual interfacial reaction as well as diffusion of participating elements. While for small oxide thickness the interfacial reaction rate controls the oxidation rate, with increasing thickness the limited diffusion becomes more and more rate limiting. This behavior is dependent on different oxidizing parameters such as the temperature, time and pressure for a given oxidizing agent.

c) Oxidation Parameters

The main oxidation parameters are the oxidation temperature, time, pressure and oxidizing agent, which affect the main oxidation properties such as growth rate, surface and interface roughness as well as its electronic properties. Independent of these parameters only monoclinic β-Ga_2O_3 is found on top of the oxynitride layer [ZAIS+08] [OC12].

In general there is much literature available regarding the influence of oxidation parameters, whereby the oxidation temperature is varied between 700 and 1.100 °C with times ranging from 1 min [HCSM10] up to 50 h [RWW+99] in different oxidizing agents such as O_2 with or without H_2O vapor or N_2O [OC13] [OC12]. The resulting growth rate starts at negligible rates, reaching values of up to over 800 nm/h (1000 °C, 30 min, N_2O [OC13]), while the surface roughness (root mean square (RMS)) varies between 1.8 nm ($10{\cdot}10\ \mu m^2$) [OC13] for untreated surfaces and about 80 nm ($10{\cdot}10\ \mu m^2$; 1000 °C; 120 min; atm. pr.;

N_2O) for oxidized ones [OC13].

Temperature and Time Behavior:
The temperature is by far the most influential parameter for oxidation of GaN. Besides also time, pressure, initial material and the oxidizing agent play a role, but the temperature dictates the qualitative oxidation behavior, while other parameters mostly affect quantitative parameters.

Oxidation starts at a certain threshold of about 750-800 °C and the oxide layer thickness can be calculated by the following formulas [ZAIS+08] [OC12]:

$$d = d_0 \, e^{\frac{-E_A}{k\,T}} \quad (2.2)$$

$$d^n = r \, t \quad (2.3)$$

d is the oxide thickness, d_0 the initial oxide thickness, E_A the activation energy of the oxide layer formation, k the Boltzmann constant, T the temperature, r the reaction rate constant, t the oxidation time and n the reaction order, which is an indicator for the rate limiting process.

While the oxide layers thickness increases exponentially with temperature, the time dependency is linear, at least below a certain threshold as depicted in fig. 2.5.

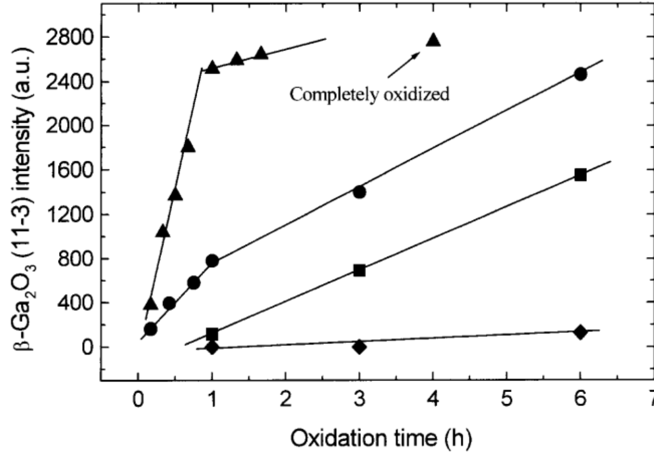

Figure 2.5: intensity of the β-Ga_2O_3 peak in X-ray diffraction (XRD) analysis, which is proportional to the oxide layer thickness, as a function of the oxidation time for various temperatures (diamond: 800 °C; square: 900 °C; circle: 1000 °C; triangle: 1050 °C); the knee for temperatures greater than 900 °C indicates a change of the oxidation limiting process) [CZX+00]

The oxidation reaction is described by eq. 2.1 but there are two different processes that can limit the reaction [ZAIS+08] [CZX+00]. First, if enough O is available and emerging N can evaporate fast enough, the oxidation rate is limited by the interfacial reaction rate r, dictating linear oxide growth with time and being indicated by a value of 1 for n. If the oxide thickness reaches a critical value, the diffusion rate of oxygen or nitrogen is too low to provide sufficient new reactants for the oxidation reaction or to dissipate emerging side products. Thus the oxidation rate becomes diffusion limited, causing the oxide layer growth to be proportional to the square root of the oxidation time, indicated by an n-factor of 2

[CZX+00] [ZAIS+08]. This transition is very temperature sensitive and is only observed for oxidation at high temperatures.

For temperatures below 950 °C even after 12 h the value of n, which is about 1 and thus indicating interface reaction limited oxidation, does not change significantly. The reported value of n in this region differs significantly for various groups, which e.g. find for oxidation at 900 °C values between 0.7 [CZX+00] and 1.3 [ZAIS+08] and also within one group n is varying between 0.7 and 1.1 [CZX+00] or 0.9 and 1.3 [ZAIS+08] for various temperatures. Though different quantitative information is gained, qualitative observations are identical.

At 950 °C after 8 h an immediate increase of n from 1.1 to 2.8 occurs, which is a clear indication for the change from interfacial reaction to diffusion limitation [ZAIS+08]. For higher temperatures of 1000 and 1050 °C the critical time of the transition decreases to about 1 h, but observed by a different group [CZX+00]. Within one group no shift is observed for different temperatures.

For an oxidation temperature of 1050 °C n increases from 0.9 up to 7.8, which is presumably far too high to be explained just by a change of the reaction limitation. In combination with the massively increased oxidation rate at 1100 °C it may be concluded that these are effects of decomposition [CZX+00]. It is remarkable that all these processes are far beneath the melting point of 2518 °C [ABD+96].

Increasing temperature not only causes enhanced oxide layer growth but also severe roughening of both, the oxide surface as well as the oxide/semiconductor interface. The surface roughness (RMS) increases slowly at moderate temperatures, while at 1000 °C the roughness becomes far higher, probably due to GaN decomposition. The interface on the other hand stays smooth except some pits due to preferential oxidation at dislocations up to 900 °C. Starting at 950 °C severe roughening is observed, caused by bubble-like domains, which are not related to dislocation, but presumably to GaN decomposition [ZAIS+08].

The morphology is also reported to change with oxidation temperature, while at room temperature amorphous oxide layers form, with increasing temperature more ordered structures are found [DFN06b] [OC12]. Due to the thin oxide layer it is criticized that this might be an artifact due to the small thickness of these layers [OC12].

The dependency of the electrical behavior has also been investigated, e.g. on GaN MOS capacitors with 100 nm thick oxides, formed at oxidation temperatures between 750 and 850 °C and times of several hours [LLLL06]. Samples formed at 800 °C are found to be most suitable for devices due to the best electric behavior (I-V and C-V characteristics) and surface morphology. While lower temperatures show incomplete oxidation and thus a lack of crystallinity, higher temperatures lead to better interface quality due to more complete oxidation but on the other hand show decomposition of both GaN and oxide [LLLL06]. More detailed information about electronic characterization is found in [Kol15] [ZAIS+08] [HCSM10] [MWVdW10].

Oxidizing Agents:
The main reason for the use of different oxidizing agents is usually to enhance the oxide growth rate. In order to show the superior behavior of oxidizing agents other than O_2 in terms of higher oxide growth rates, the calculation of the temperature independent activation energy is reasonable. This information can be extracted from the slope of an Arrhenius plot

by usage of eq. 2.2 in a different form:

$$E_A = \frac{ln(d_0) - ln(d)}{\frac{1}{k \cdot T}} \tag{2.4}$$

Under comparable conditions activation energies of 300 kJ/mol for dry (O_2) [OC12], 210 kJ/mol for wet (H_2O vapor assisted O_2) [RWW+99] and 160 kJ/mol for N_2O-oxidation [OC12] are gained. This enables higher growth rates for N_2O than for wet and far higher than for dry oxidation in O_2.

The activation energy for extracting O out of N_2O (2.51 eV) is less than half as for O_2 (5.12 eV), causing the highly reduced activation energy for the oxidation of GaN and the strongly enhanced oxidation rate [OC13]. Further, the partial pressure of nitrogen is higher due to dissociation of N_2O, causing suppression of GaN-decomposition [OC13].

The oxide growth is similar to dry oxidation in O_2, but there are some distinctions. Hillocks are also growing, but in random distribution. The reaction limitation changes from interfacial reaction to diffusion limited and takes place for oxidation at 1000 °C after 60 min. While for moderate temperatures in a range of 700-900 °C only Ga_2O_3 and GaON components form, they become nonstoichiometric Ga_xO_y and $Ga_xO_yN_z$ compounds at 1000 °C [OC12].

Due to the lower activation energy, wet thermal oxidation shows 15 times higher growth rates as well as smoother surfaces compared to dry oxidation. On the other hand the GaN/oxide interface becomes rougher, resulting in poorer electronic behavior [RWW+99].

d) Plasma Oxidation

The main advantage of plasma oxidation is that lower temperatures are required since activation energies for chemical reactions are far lower because of the existence of free ions. While thermal oxidation takes place in a temperature range where surface degradation due to decomposition plays a major role, this issue does not occur in plasma ovens with temperatures of about 300 °C or less, depending on the chamber pressure. On the other hand the experimental setup is more complex and ions have high energies, resulting in possible sputtering of the surface and thus reduced growth rates and a modification of the surface stoichiometry by preferential sputtering of the nitride component [KP15].

In the literature, oxide layers with a wide range of thicknesses from very thin oxides in the range of a few monolayer up to thicknesses of several hundred nm are reported. Contrary to thermal oxidation in annealing ovens, plasma ovens have numerous processing parameters affecting the oxidation behavior. In tab. 2 different processing parameters from different groups are listed in order to demonstrate their importance to the oxide layer thickness.

Unlike thermal oxides, the oxide thickness of oxides formed by plasma oxidation saturates after a certain time, which depends on the process parameters. For instance, saturation can occur after 20 min for processing parameters as shown in the second row of tab. 2 or after 60 min for conditions shown in the first row of tab. 2. The reason for this phenomenon is the fixed oxygen plasma density [LKS+08].

Furthermore it is remarkable, that in contrast to thermal oxidation the surface roughness decreases with increasing oxidation time [LKS+08] [Bae03].

RF power [W]	RF frequency [MHz]	chamber pressure [Torr]	gas flow rate [sccm]	temperature [°C]	time [min]	oxide thickness [nm]
60	13.56	10^{-6}	100	300	60	200
700	2450	10^{-3}	12	150-200	20	10
60	13.56	0.3	O_2: 20, He: 200	250-300	30	3.5

Table 2: processing parameters for plasma oxidation and the resulting oxide thickness [LKS+08] [PMR+03] [Bae03]

e) Other Oxidation Methods:
Despite thermal and plasma oxidation there are some more exotic forms of oxidation. One of these methods is anodic oxidation, also referred to as electrochemical oxidation, which requires a more complex experimental setup than the other methods. First of all the anodic process is only efficient if in the semiconductor holes exist (type p), for type n materials holes have to be generated. This can be achieved by illumination, also known as photo-enhanced anodic oxidation. Since GaN surface layers are naturally undoped, they have to be doped first in order to grow oxide layers [KP15]. Since anodic oxidation occurs preferentially at troughs while peaks are not harmed, no uniform layer is formed [PST+03].

Chemical oxidation is another oxidation form, but this is only performed for the purpose of surface cleaning and not for the formation of oxide layers.

2.2.2 Decomposition

Relevant surface treatments mostly involve high temperatures, at which decomposition plays a major role. Especially thermal oxidation requires temperatures, where severe decomposition occurs. Since decomposition for GaN depends on the atmosphere, it is first described in vacuum and subsequently differences in H_2 and N_2 ambient are presented.

Vacuum:
In general the high thermal stability of GaN is derived from its wurtzite crystal structure. In this structure every nitrogen atom has four very strong covalent bonds to neighboring Ga atoms causing N to be partly evolved by thermal decomposition in form of free atoms. Since the two closest N atoms in the crystal structure are 3.2 Å apart, far larger than the N-N internuclear distance in the gaseous N_2 molecule with 0.1 Å, it is unlikely that only N_2 molecules evolve from decomposition. The decomposition reaction in vacuum is therefore [L0]

$$GaN(s) \;\Rightarrow\; Ga(g) + 0.5\ N + 0.25\ N_2, \tag{2.5}$$

here the numerical values were taken from comparison of experimentally and theoretically calculated kinetic parameters [L0].

Due to the low equilibrium partial pressure of Ga, gaseous Ga condensates on the GaN

surface and forms stable Ga droplets further enhancing the decomposition of GaN since the condensation energy is transferred to the reactant. This reduces the reaction enthalpy for decomposition (eq. 2.5) from 629.3 to 488.0 kJ/mol and thererfore increases the equilibrium partial pressure of Ga. At the interface Ga(l)/GaN(s), where decomposition is accompanied by Ga vapor condensation, the required temperature of GaN decomposition is reduced from 1027 to 827 °C [L0]. Thus the presence of Ga droplets acts as catalyst for GaN decomposition.

H2:

Decomposition in H_2 is usually described by the following reaction [L0]:

$$GaN(s) + 1.5\ H_2 \ \Rightarrow\ Ga(g) + NH_3 \tag{2.6}$$

Especially for low temperatures or different ambients besides this explained reaction, also other products such as GaH, GaH_2, GaH_3 and N_2 have to be considered [KWH$^+$01]. By adding N_2 or NH_3, decomposition can be suppressed, e.g. by adding 3% NH_3 to an H_2 ambient, the decomposition temperature increases from 600 to 977 °C [L0]. While for temperatures below 830 °C decomposition is controlled by the desorption of GaH_x ($0 \leq x \leq 3$), above this temperature decomposition of Ga becomes the limiting factor.

The formation of liquid Ga droplets shows the same catalytic effect it does in vacuum, whereby additionally H_2 dissociates on liquid Ga, enhancing this effect [KWH$^+$01].

The decomposition not only depends on the temperature, but also on the H_2 pressure. This originates from H_2 dissociation on the surface, followed by the formation and desorption of NH_3. The Ga desorption rate on the other hand stays constant for varying pressure, and the number and size of Ga droplets increases with enhanced H_2 pressure (for pressures exceeding 100 Torr) [KWH$^+$01].

N_2:

Decomposition in N_2 does not depend on the N_2 pressure and is observed to start at about 1000 °C [KWH$^+$01] [ROC$^+$03], although this value differs between 900 [CRC$^+$02] and 1200 °C [MKA$^+$05] according to different groups. The annealing reaction is [ROC$^+$03]:

$$2GaN(s) \ \Rightarrow\ 2Ga(l) + N_2(g) \tag{2.7}$$

N_2 annealing also forms Ga droplets on the surface, which have a size of about a tenth compared to decomposition in H_2 for similar conditions. In N_2 ambient these droplets are in subsequently incorporated by some oxygen, resulting in a mixture of metallic Ga droplets, Ga oxide and gallium oxynitrde, whose composition depends on the annealing temperature.

While for 1000 and 1050 °C some kind of gallium oxynitride ($Ga_2O_{3-x}N_{\frac{2}{3}x}$ [ROC$^+$03]) is predominant, at 1100 °C already an at least 100 nm thick stoichiometric Ga_2O_3 layer is formed. Above 1000 °C not only decomposition with N evaporation but also Ga loss is observed due to the coexistence of metallic Ga droplets and gallium oxide [ROC$^+$03]:

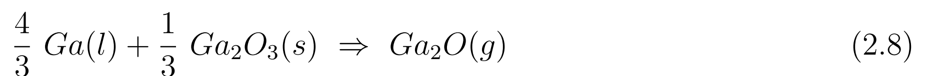

$$\frac{4}{3}\ Ga(l) + \frac{1}{3}\ Ga_2O_3(s) \ \Rightarrow\ Ga_2O(g) \tag{2.8}$$

2.2.3 Surface Cleaning and Oxide Removal

When exposed to air, GaN surfaces always show some amount of contamination, mostly consisting of oxygen and carbon. Great effort is spent in order to find the best method to remove this contamination, but perfectly clean surfaces are not achievable and it is not clear if this would be desirable. There is a great variety of different cleaning methods such as the large number of different wet chemical treatments, plasma etching, thermal desorption, ultrasonically- and photo-enhanced methods as well as combinations thereof. Since most contamination is native Ga-oxide, it seems reasonable that effective cleaning techniques are also successful candidates for the removal of the oxide. Thus wet chemical etching in HCl is not only an appropriate way to clean GaN surfaces but also to remove thick oxides. While HCl at room temperature is sufficient to remove oxide adsorbates, for thick, artificially produced oxide layers, temperatures of up to 250 °C are used in order to increase the etch rate to a reasonable value [ZAIS+08]. More related information on cleaning and oxide removal is found in [Kol15] [KBB+98] [LM12].

2.3 Analysis

In order to analyze surface modifications a variety of different chemical and physical analysis techniques exist, whereby the focus of this thesis lies on Auger electron spectroscopy (AES).

2.3.1 AES Analysis

AES is a very surface sensitive analytical technique, applied for surface composition investigation for all elements except H and He. By adding a sputter gun also depth resolved elemental analysis is available. The apparatus basically consists of an electron gun, an electron detector, optionally an Ar^+-ion gun for sputtering and a sample holder in its center, whereby all of this is mounted in an UHV chamber. The underlying physical process for this technique is the Auger effect, depicted in fig. 2.6.

First of all an inner-shell vacancy has to be generated, in AES by an electron gun, contrary to XPS, which works similar, using photons instead. Emitted electrons from the electron gun have energies usually in a range between 1 and 10 kV and are focused to a small area on the surface where they interact with the solid. Due to their high energies, some transferred energies are higher than the binding energy of inner shell electrons of light elements or higher core levels of heavier elements and lead to ionization and respectively core holes. The atom is then in an excited state, which rapidly relaxes by an outer shell electron falling from a higher energy level to the lower hole as seen in fig. 2.6. The energy difference can be emitted by a photon with a characteristic energy used in EDX analysis, or transferred to another outer core electron which is emitted if the transferred energy exceeds its binding energy. This generates so called Auger electrons with characteristic kinetic energies described by the following formula:

$$E_{kin} = E_i - E_1 - E_2 \tag{2.9}$$

here E_i, E_1 and E_2 are the potential energies of the core level, first level outer shell and second outer shell electron energies, respectively (fig. 2.6). Since three electrons are involved

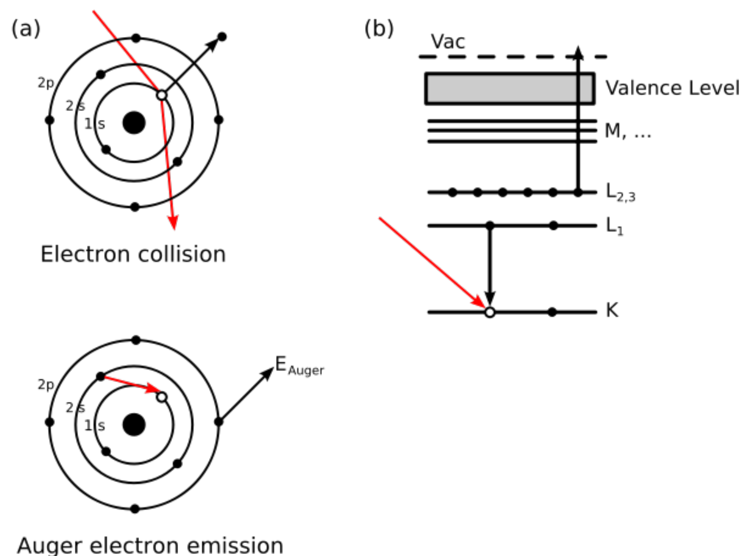

Figure 2.6: demonstration of the Auger effect a) in an atomistic model and b) in an energy band diagram [Wik14]

in this process, only elements with at least three electrons are able to produce Auger electrons so that H and He cannot be recognized by AES analysis. Due to its characteristic kinetic energy, Auger electrons, which are registered energy-resolved in an electron detector, enable elemental analysis. Auger electrons from different elements have different energies, as a consequence the inelastic mean free path and therefore also the information depth depends on the material.

Information Depth:
Due to electron bombardment of a sample, a variety of processes occurs in the surface near layer, causing excitation in the so called activation volume (fig. 2.7).

This excitation goes along with the emission of electrons, whereby besides the predominant amount of backscattered and secondary electrons also Auger electrons are generated. Within this activation volume also X-rays (photons) are emitted and due to their mean free path (MFP) length being larger than the penetration depth of the incident electrons, EDX receives signal from the whole activation volume. In AES the same activation volume is excited and generates Auger electrons, but since their inelastic mean free path (IMFP) length is in the range of few nm, only electrons from a small information volume near the surface reaches the analyzer without losing energy. Though Auger electrons are also formed in the whole activation volume, if their formation takes place in regions deeper than the IMFP, they are inelastically scattered, loose energy and do not contribute to characteristic peaks but to the inelastic background in the spectra.

The IMFP and thus the information depth depend on the electron energy as depicted in fig. 2.8.

In analogy to AES, XPS is performed with X-rays as excitation source and by measuring photoelectrons instead of Auger electrons. Electrons are emitted due to the absorption of photons with energies exceeding the electron's binding energy. The difference between the excitation energy and the binding energy is the kinetic energy of the electron and since

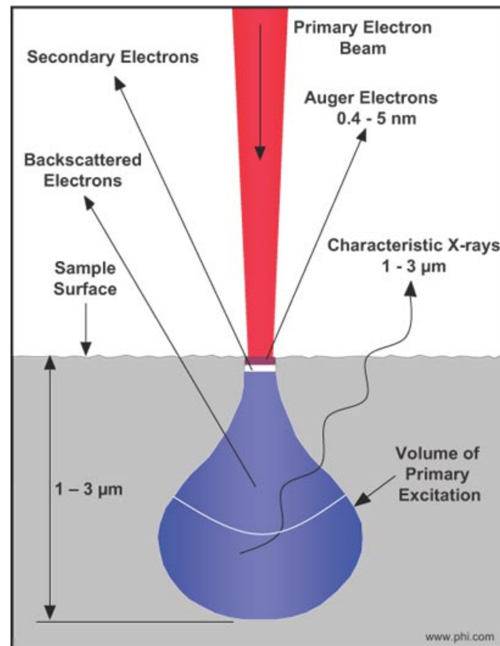

Figure 2.7: activation volume due to electron bombardment [Phi14]

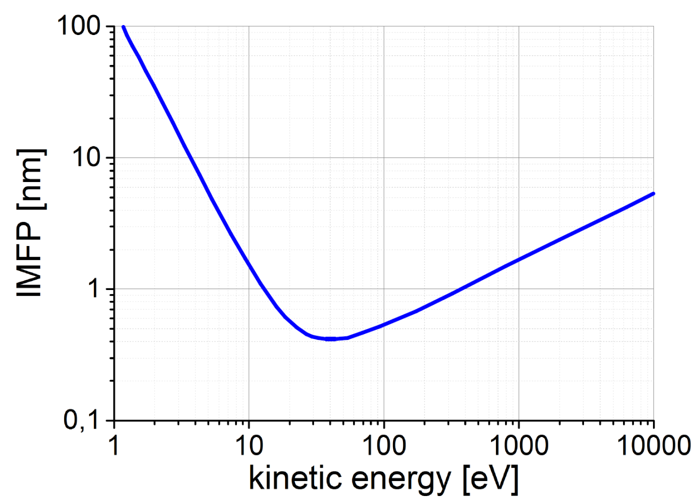

Figure 2.8: inelastic mean free path as a function of the electron energy [Nix14]

the binding energy of a given electronic level is characteristic for the element, elemental information is accessible. Assessment is similar to AES, but while Auger electrons have fixed energies, independent of the excitation energy, the photoelectron energy in XPS depends on the excitation energy. Thus information depths in AES are universal while they are dependent on the excitation energy in XPS.

Furthermore it has to be considered that the dependency of the IMFP on the energy as shown in fig. 2.8 depends on the material.

Assessment/Quantification:
The aim of AES analysis is to reveal the surface composition, where the process of its evaluation from raw data is shown in fig. 2.9 in a simplified way.

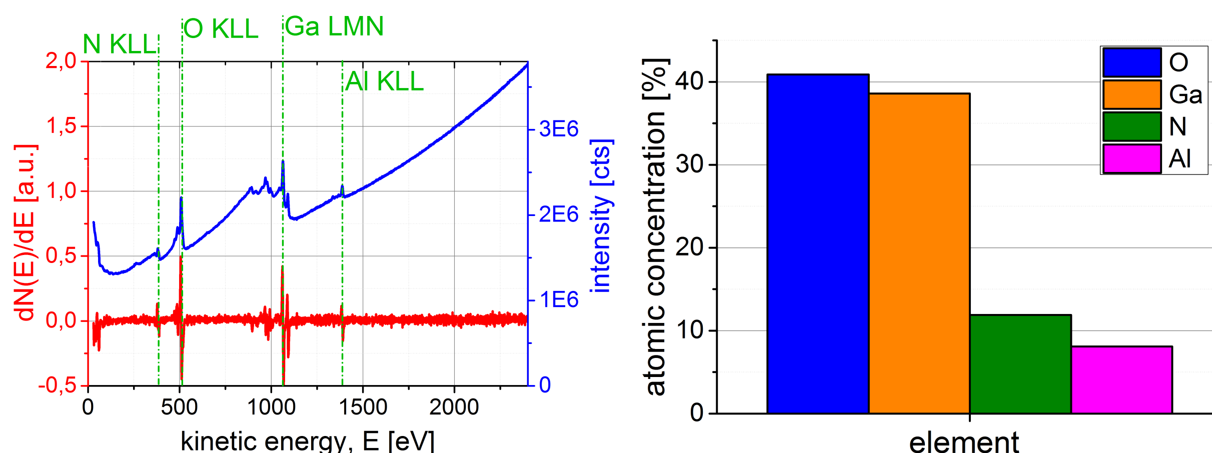

Figure 2.9: oxidation of an AlGaN sample at 900 °C 10 min (RTA): a) raw (blue) and differentiated (red) AES spectrum and b) the gained surface composition

First of all the electron detector measures the electron intensity as a function of its energy, resulting in spectra as shown in fig. 2.9a. Besides Auger peaks, spectra consist high background signal originating from scattered Auger electrons and secondary electrons generated by inelastic scattering. Furthermore Auger processes involve three electrons leading to very complex peak forms, which are also dependent on chemical bonds. Thus, unlike XPS the usage of the peak area for quantification does not deliver reasonable results. Therefore the differentiated spectrum is used for analysis, enhancing the S/N-ratio and the background practically vanishes and does not have to be subtracted. In the differentiated spectrum the difference in differentiated intensity between the peak maximum and minimum is calculated and multiplied by a relative sensitivity factor (RSF). Subsequent normalization finally delivers the surface composition in atomic concentrations. RSF factors are calibrated by samples with known concentrations, enabling quantitative analysis. Since the peak form depends on chemical bonds of an element, the differentiated spectrum also varies leading to different RSF for one element in different chemical surroundings. By this form of quantification physical information gets lost and thus AES is called a semi-quantitative analysis method. Absolute atomic concentrations of unknown samples should only be considered as approximation. However for the comparison of similar samples, small variations in the composition are sensitively revealed.

Auger Depth Profiling:

In order to get depth information, especially for layer thicknesses exceeding the information depth, sputtering is the only option. If the superficial layer is rather homogeneous with a flat surface and interface and thinner than the information depth, depth information can also be gained by surface measurements. If the layer thickness is the main point of interest and references of the underlayer and superficial layer are available, this information is also available from quantitative comparison of surface measurements. Especially for very thin layers, enhanced depth resolved compositional information can be achieved by angle resolved measurements.

a) Sputter Profiles

The idea of sputtering is to slowly remove the material layer by layer while measuring surface spectra, providing an elemental resolved depth profile in the end. Sputtering and measuring is done alternating, whereby the sputter time and as a consequence material removal can be adjusted. Therefore it has to be considered that the sputter rate depends sensitively on the actual material.

b) Depth Information by Angle resolved Surface Spectra

For an angle between sample and electron detector of 90°, Auger electrons leave the sample perpendicular to the surface, thus the information depth equals the IMFP. With lower angles, electrons leave the sample not perpendicular, resulting in longer paths through the material. Thus the information depth d decreases with declining angles α for a specific IMFP λ:

$$d = \lambda \cdot sin(\alpha) \tag{2.10}$$

For small angles, the analysis becomes more sensitive to the surface. Starting at 90° and lowering the angle, at some point no Auger electrons from the structure under the superficial layer are penetrating the surface without energy loss. The information depth at this angle can be estimated as the layer thickness. If this angle is not accessible due to the experimental setup, it can be calculated from the progression at higher angles.

2.3.2 other Analysis Methods

AES is eminently suitable to gain a first impression of altered surfaces but in order to get further insight, additional analysis techniques are required. The strengths of these techniques (over AES) are briefly described below.

Although the lateral resolution of SEM-analysis with the AES setup is theoretically several hundred nm, it is in reality much worse and other methods are required in order to get precise topographic information of the surface. First of all SEM can be used, which works analogous to the AES-SEM, but is optimized for topographic information and enables much higher resolution. Another technique is atomic force microscopy (AFM), where a cantilever scans over the surface and thus not only leads to high resolution but also quantitative information about the height and depth of structures.

The depths of layers can be obtained by AES, but since the compositional information originates from an area in the range of μm^2 while surface structures are usually about three magnitudes smaller, additional techniques such as cross-sectional SEM and TEM are required

in order to obtain laterally resolved structures. Transmission electron microscopy (TEM) is similar to SEM with the difference that transmitted electrons are analyzed, leading to far higher resolutions down to atomic resolution. However, this requires very precise preparation of sample lamellas of a thickness of about 50 nm thickness.

For further elemental analysis energy-dispersive X-ray spectroscopy (EDX), which is available in SEM and TEM, and electron energy loss spectroscopy (EELS), available in TEM, are performed. For EELS the electron energy loss of electrons transmitting the thin sample is measured and due to the fact that every element has characteristic loss features (”ionization edges”), elemental analysis is achievable. The most important advantage of this method is its lateral resolution in the nm range.

X-ray photoelectron spectroscopy (XPS) works similar to AES with the difference that instead of electrons, X-rays are focused on the sample's surface. The lateral resolution of XPS is worse but in addition to information on the composition, chemical bonds can be distinguished and quantification is simpler and generally more accurate than for AES.

For crystallographic information selected area electron diffraction (SAED) analysis can be performed in the TEM. For this purpose, the electron microscopes focus is altered in a way that the diffraction pattern is obtained. This delivers not only the crystallinity and crystal structure but also lattice constants are obtained.

By combination of all techniques a complete physical and chemical characterization of surfaces and superficial layers can be achieved in all three dimensions.

3 Experimental

3.1 Sample Preparation

AlGaN/GaN structures are epitaxially grown on Si(111) by MOCVD, followed by cleaning in HCl/H_2O and further further processing:

3.1.1 Oxidation

Oxidation is achieved by exposing samples to specific atmospheres for specific parameters such as temperature, time and pressure. For this purpose, the three used oven forms are compared:

Rapid Thermal Annealing
The advantage of rapid thermal annealing (RTA) over other furnaces is its fast processing. Within this thesis, samples are oxidized in N_2 and O_2 atmosphere up to 1100 °C. As the walls of the used RTA oven are of graphite, the processing time is limited in order to prevent damage. Depending on the temperature, the maximum processing time is only in the range of several minutes.

As the wafer is mounted horizontally in the chamber, not only entire wafers but also wafer fragments, mounted on Si carrier wafers can be processed.

The O_2 and N_2 flow is 15 l/min and the chamber is always under atmospheric pressure.

Horizontal Oven
A second group of samples is oxidized in a horizontal oven, therefore they are annealed in O_2, H_2O vapor assisted O_2 (referred to as “H2O”), NH_3 and N_2O atmospheres. The processing temperature is varied up to 850 °C for durations up to 4 h. Horizontal oven processes can be performed for several wafers at once, but not for fragments.

O_2 and H_2O processes are in general analogous to RTA, the O_2-flow is also 15 l/min, but the pressure is only 750 mTorr. In N_2O the maximum flux is 0.2 l/min and the chamber pressure is limited to 350 mTorr.

Plasma Oven
A third group of samples is oxidized in plasma oven processes at a temperature of 300 °C and a chamber pressure of 1.2 Torr with durations up to 30 min.

3.1.2 Oxide Removal

Oxide removal is achieved by etching in a 2:1:1 $HCl:H_2O_2:H_2O$ solution at 85 °C for 2 h.

3.2 Surface sensitive Analysis by AES

Auger electron spectroscopy (AES) is known as a very surface sensitive method for investigating chemical components of samples. The information depth of AES for elements of interest similar to XPS is approximately between 1 and 3 nm (tab.5).

The AES device setup is schematically shown in fig. 3.1 and consists of an electron gun, an electron detector and a sputter gun to enable depth profiling as well as a sample holder in its center. The electron gun in the used setup is realized by a LaB_6 cathode and corresponding electron optics, the electron detector by a hemispherical electron energy analyzer and the sputter gun sputters with positive Ar ions. The whole setup is mounted in a UHV chamber with a pressure in the range of several 10^{-9} mbar. While the electron analyzer is perpendicular to the sample surface, the electron gun as well as the ion gun axes describe an angle of 30 ° with the sample surface and are perpendicular to each other (fig. 3.1).

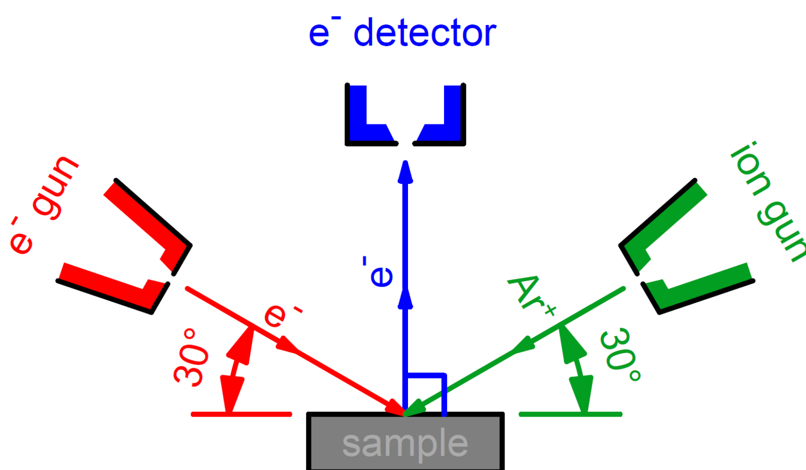

Figure 3.1: schematic view of the experimental AES setup showing the geometrical arrangement of the components

The electron gun produces electrons with energies of 1 to 10 kV, standard measurements are performed with 5 kV on a square area of 50·50 μm^2.

For depth profiling, samples are sputtered by Ar ions with an energy of 2 keV, yielding a sputter rate of 8 nm/min for SiO_2. To reduce the measurement time only an energy range of ±30 eV around the Auger peaks of relevant elements is analyzed.

For angle resolved measurements the sample can be tilted in order to increase or decrease the angle between sample and electron detector as shown in fig. 3.2. Due to the geometrical setup the angle can only be tilted 35 ° so that for a standard flat sample holder the mini-

mum angle is 55 °. In order to lower this value a special wedge-shaped sample holder with an incident angle of 30 ° can be used to achieve a minimum angle of 25 ° (fig. 3.2).

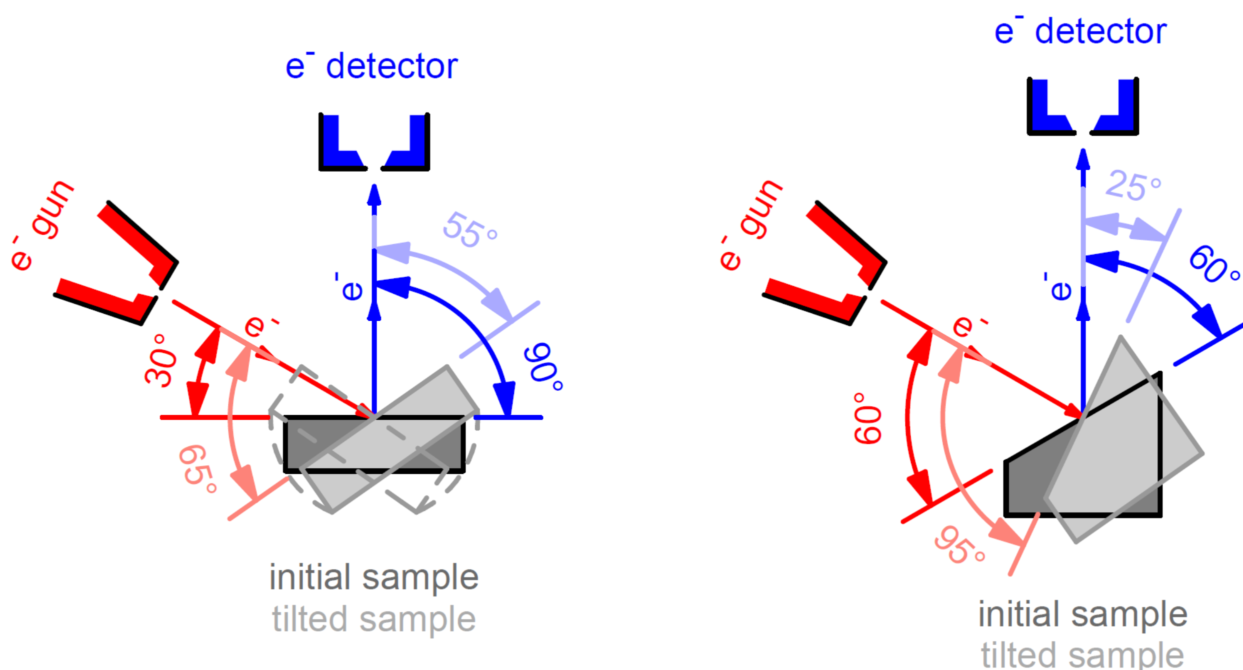

Figure 3.2: AES setup with different sample holders showing the achievable angles between electron gun, sample and electron detector for the initial position and the maximum tilted sample

3.3 other Analysis Methods

For SEM and SEM-EDX analysis, the incident electron energy is 5 keV.

AFM analysis is performed with a Si cantilever in tapping mode.

For TEM analysis an appropriate TEM lamella has to be prepared, what is done via FIB in situ lift-out technique in order to achieve a lamella thickness of 50 nm. To protect the top layers, a 600 nm thick Si layer is deposited on top of the sample. The beam electron energy is usually 10 keV, for EDX analysis it is increased to 20 keV.

For XPS analysis a square area of 100·100 μm^2 is excited by monochromatic Al K-α X-rays with an energy of approximately 1.5 keV. The angle between the ion gun and the sample surface is 67.5 ° and between the sample surface and the electron detector 45 °. The ion gun works analogous to the one used in AES, but with an ion energy of 1 keV, yielding a sputter rate of 1 nm/min for SiO_2.

4 Results

The procedure of investigating the oxidation process is simplified shown in fig. 4.1:

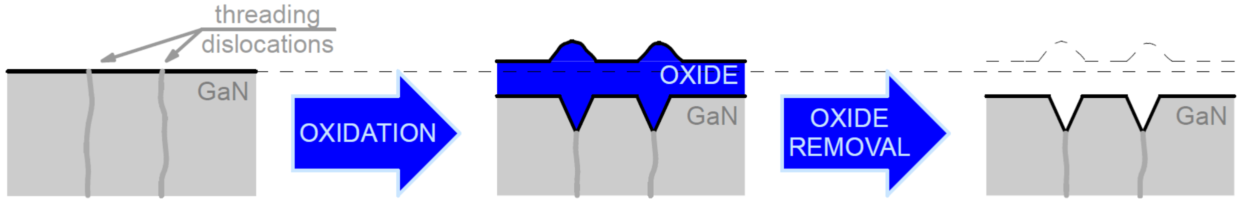

Figure 4.1: simplified procedure for the investigation of the oxidation process

4.1 Raw Sample

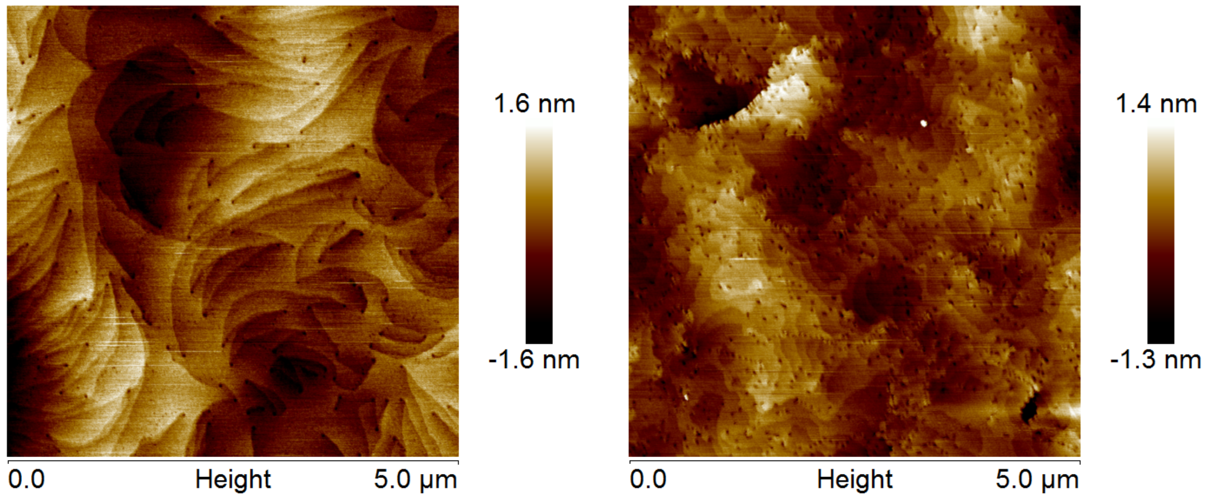

Figure 4.2: AFM analysis of the as-grown a) GaN and b) AlGaN surface

The epitaxial growth of GaN on Si substrates causes stress and further threading dislocations that result in observable pits and terraces at the surface as revealed by AFM analysis in fig. 4.2a. There are three different forms of threading dislocations. While screw and edge types are not observed at the as-grown surface, there is a great number of mixed dislocations. They can be distinguished from other types since they form pits and are due to their screw component corner points of terrace-shaped structures (fig. 4.2a) [HTE+99] [WM04] [Che27], which originate from the layered GaN growth and are related to layer steps. Screw dislocations form larger pits while edge types lead to smaller ones, which are located within terrace structures [Che27] but are not recognized at the raw surface in fig. 4.2a. The reason is presumably the small lateral size of edge dislocation pits, which cannot be resolved by the existing AFM setup and the low density of screw dislocations. However, as oxidation is preferred at dislocations, regardless of their type, their amount can be estimated from fig. 4.5.

The dislocation density of mixed types are similar to edge ones approximately $5{\cdot}10^{8}$ cm^{-2} on these samples.

With an AlGaN barrier layer of a few nm thickness on top of GaN terraces are also observed, but with different shapes (fig. 4.2b). All types of dislocations are found and in addition large terrace-shaped holes with a major dimension of up to 300 nm and a depth of up to 10 nm (fig. 4.2b in the bottom right corner). The overall dislocation density is $4{\cdot}10^{9}$ cm^{-2}, clearly higher compared to the GaN layer. Large holes have a low density which is hard to quantify but in the range of $1{\cdot}10^{7}$ cm^{-2}.

Besides dislocations the surface exhibits enhanced oxygen concentrations up to 8 at.% (fig. 4.3), that decrease to values beyond the detection limit of AES of approximately 2% within 0.3 min of sputtering (mos) in GaN and 0.6 mos in AlGaN. The unit mos is used for depths as direct conversion to length units is not adequately possible due to the lack of exact sputter rates; rough estimations are given in tab. 3. The increased O amount originates from O adsorption due to exposure to atmosphere.

In addition to O, on the very surface carbon in an amount of up to 18 at.% is observed, which decreases below the detection limit after the first sputter cycle, which equals less than 0.05 mos. This is referred to as carbonaceous contamination due to the exposure to air.

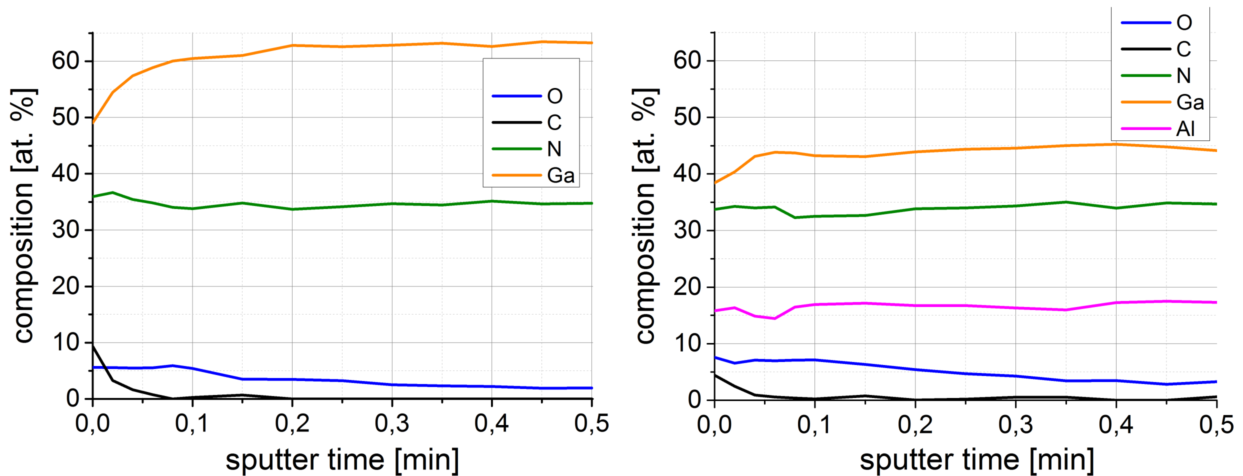

Figure 4.3: AES depths profiles of raw reference samples: a) GaN and b) AlGaN

4.2 Surface Treatments

4.2.1 Oxidation

a) Rapid Thermal Annealing

For standard investigations RTA is superior over annealing in horizontal ovens due to the possibility to handle not only entire wafers but also wafer fragments. As every wafer shows small differences even under identical growth conditions, the ability to process fragments means that reference samples as well as variously processed fragments, originating from

the same wafer, can be investigated. In fact, all RTA investigations are done on a single wafer. However, annealing of fragments on a Si carrier wafer requires modification of the temperature profile during processing as shown in fig. 4.4.

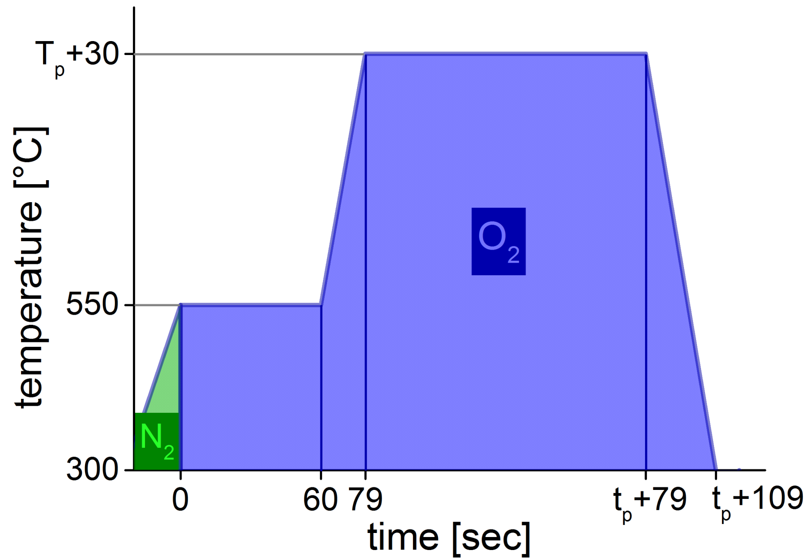

Figure 4.4: temperature profile during processing (T_p... processing temperature, t_p... processing time)

After sample mounting the temperature is ramped to 550 °C, where no damage of the surface is assumed to occur. To ensure that not only the carrier wafer but also the fragments reach this temperature, it is held for 60 sec. Subsequently the temperature is ramped up to the desired temperature within 19 sec, held for the requested time and then cooled down within 30 sec. As the temperature is measured by a pyrometer from below, it evaluates the carrier wafer temperature instead of the desired sample temperature. In the relevant range between 800 and 1100 °C the actual surface temperature is on average lower by 35 °C lower. To compensate this effect, the Si carrier wafer temperature is ramped 35 °C higher than the desired value (fig. 4.4).

In order to minimize oxidation during ramping, pure N_2 with an N_2-flow of 15 l/min is used up to the 550 °C level. Then N_2 is exchanged by O_2 with the same flow rate until temperature-down-ramping is finished and the chamber is again flooded by N_2.

This RTA process alters the III-N surface as discussed in detail in the following:

RISE OF SURFACE HILLOCKS:

The start of the complex oxidation behavior can be seen by comparison of fig. 4.5 with fig. 4.2a. Surface pits due to threading dislocations with both, screw- and edge-components ("mixed"), become hillocks and furthermore smaller hillocks with an amount similar to mixed dislocations rise within terraces. Location, size and density suggest that these hillocks rise from edge dislocation sites [HTE+99]. The oxidation on threading dislocation sites originate from their enhanced chemically reactivity as the Gibbs energy reaches its local minimum. However, other chemical reactive sites, especially grain boundaries, cannot be excluded for acting as protrusion sites [RKP+15] [Rei15].

With increasing oxidation time, the hillock density stays constant, while they grow in size, as seen in fig. 4.6. Eventually they coalesce, causing decreasing density, while their growth

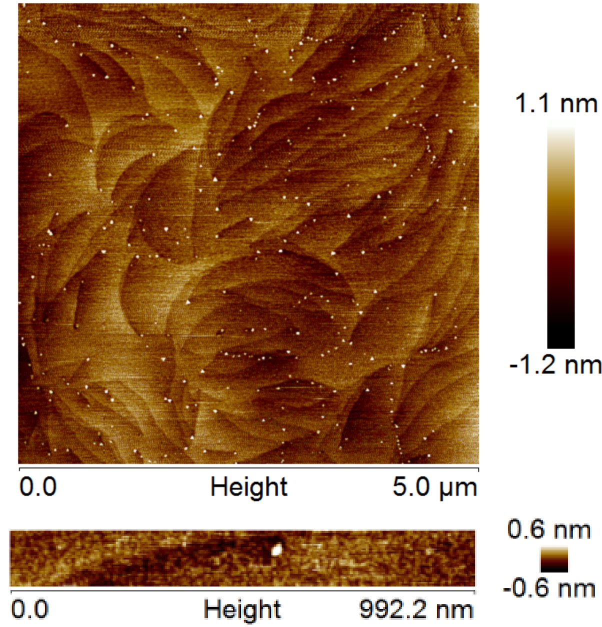

Figure 4.5: AFM analysis of the GaN surface after oxidation at 900 °C for 1 min: rise of hillocks at threading dislocation sites

in height stays rather linear.

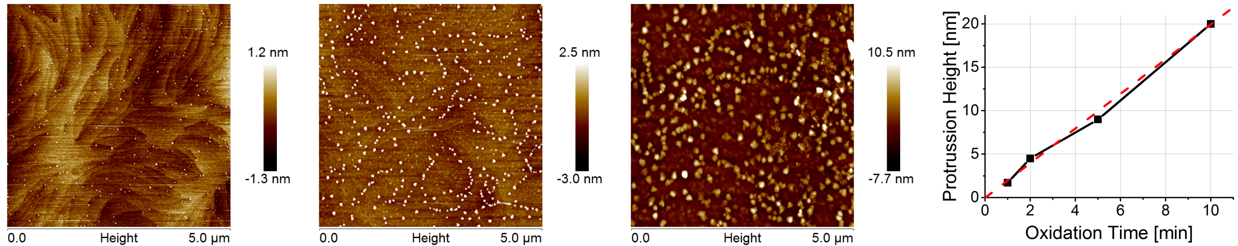

Figure 4.6: AFM analysis of the GaN surface after oxidation at 900 °C for a) 2 min, b) 5 min and c) 10 min, revealing d) the linear hillock height growth with ongoing oxidation time

Increasing temperature also introduces higher hillocks, but instead of a linear dependency the hillock height rise follows Arrhenius-law as shown in fig. 4.7.

Besides the hillock growth on threading dislocations, relatively flat structures are formed at defect free areas (fig. 4.7c). These oxide structures have distinctive edges, pointing in only three directions with adjacent angles of 60°, indicating high crystallinity of the oxide. At special conditions (e.g. fig. 4.6b), defect-induced hillocks show equilateral triangular basis, all of them parallel or mirrored to each other. More clearly these triangular structures are observed for wet oxidation in fig. 4.25. For large oxide thicknesses the triangular basis blurs continuously until it cannot be recognized anymore as shown in fig. 4.7b. The observation of these forms of structures with its distinctive edges attributed to the β-Ga_2O_3 crystal structure of the oxide:

O^{2-} ions in the β-Ga_2O_3 unit cell can be approximated as slightly distorted fcc structures [KM03] as depicted in fig. 2.4. Oriented in (111)-direction, oxide growth leads to triangular-

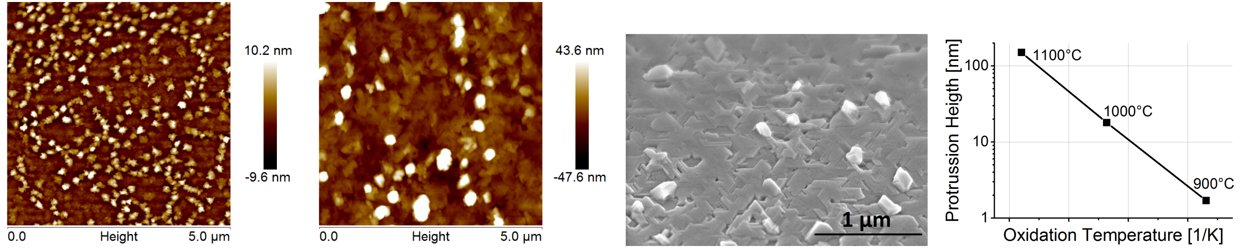

Figure 4.7: AFM and SEM analysis of the GaN surface after oxidation for 1 min at a) 1000 °C and b+c) 1100 °C; d) Arrhenius-plot of the hillock heights

based hillocks or terraces with edges with adjacent angles of 60°, as seen for the investigated oxides.

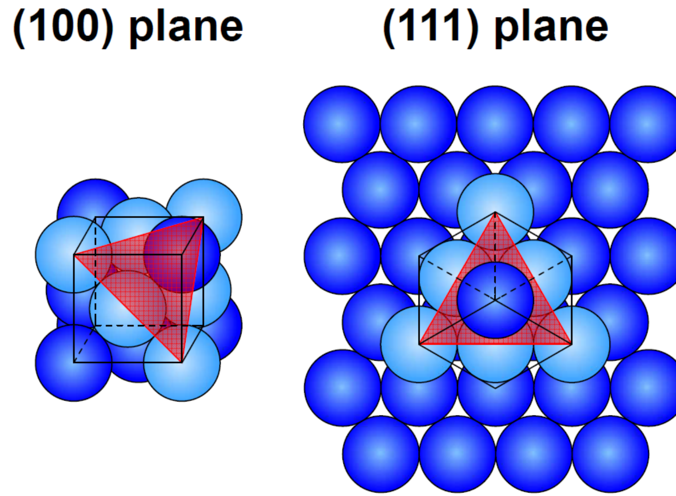

Figure 4.8: O^{2-}-ions arrange within the monoclinic β-Ga_2O_3 crystal structure in a slightly distorted fcc structure [KM03], enabling the formation of crystalline protrusions with equilateral triangular base on (111)-planes

Ga_2O_3 is created by the conversion of GaN and the associated volume expansion of 40%
Compared to surface hillocks, interface craters are observed to be larger in size, show quite perfect hexagonal basis and are all aligned in parallel. Base edges are therefore oriented in only three directions with adjacent angles of 60°. The origin is the hexagonal wurtzite crystal structure of the underlying GaN. Defect-free areas are almost entirely flat, comparable to the initial surface.

The same characteristics are found for GaN surfaces after defect etching in KOH and H_3PO_4 (fig. 4.10) [RRB+15]. The etching process is assumed to react with the GaN surface in analogy to the oxidation process, with the difference that for etching the converted material desorbs into the environment while for oxidation the converted GaN forms a solid Ga_2O_3 overlayer. Both processes show enhanced vertical reaction rates at dislocation sites, resulting in vertical contact areas where the material gets also horizontally etched or oxidized with a different rate. The horizontal reaction rate depends significantly on the direction so that only the most resistive planes remain. For etching, these most resistive planes are besides the horizontal {0001} plane only angular $\{10\bar{0}1x\}$ planes with varying values for x, no other

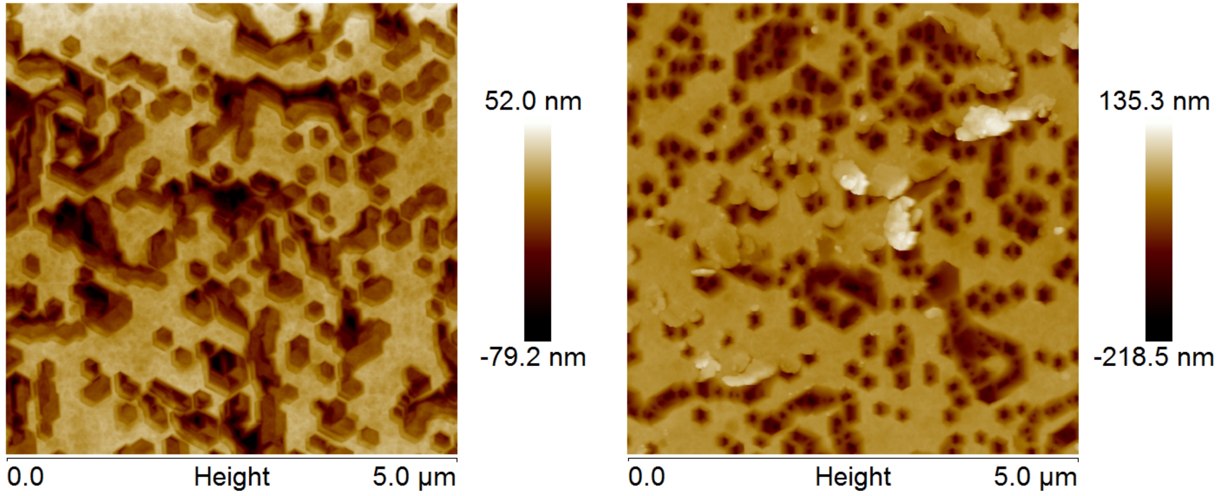

Figure 4.9: AFM analysis of the Ga_2O_3/GaN interface after oxidation at a) 900 °C for 10 min and b) 1100 °C for 1 min and subsequent oxide removal; protrusions in b) are related to contamination due to HCl etching

planes are observed. Due to the similarities between etching and oxidation, the same planes are assumed to be most resistive against oxidation. The high resisitivity of the $\{10\bar{0}1x\}$ planes is surprising since considerations as demonstrated in fig. 4.11 would suggest $\{110\bar{2}x\}$ planes to be more stable.

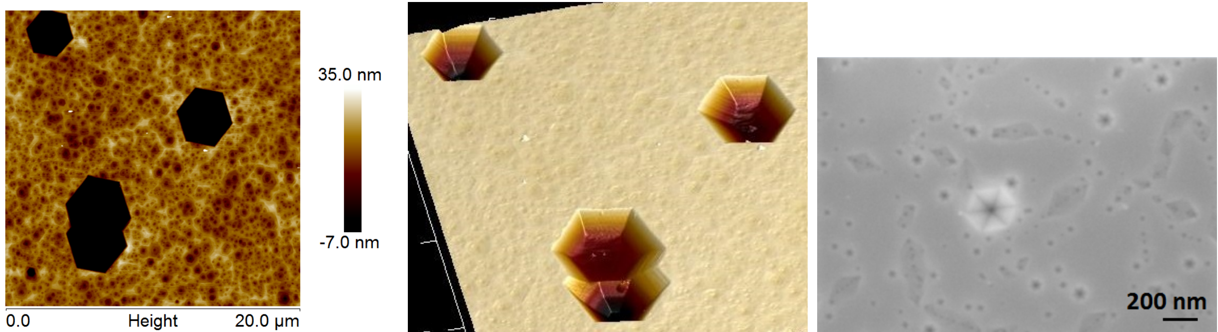

Figure 4.10: AFM analysis of surfaces after defect etching in a) H_3PO_4 [RRB+15] and b) KOH

Planes in crystals are stable if they intersect with as many atoms of the crystal as possible. Since N is not stable at the surface in GaN, Ga ions are more important. Therefore $\{110\bar{2}x\}$ planes should be most resistive as for every even value of x every Ga ion and further for every value divisible by 6 an N ion of every layer intersects with the plane. For $\{10\bar{1}x\}$ planes on the other hand, independent of the value of x no planes intersect with Ga ions of every horizontal layer and furthermore no layers intersect additionally with N ions of every layer. Fig. 4.11 shows the most stable vertical angles and the corresponding values of x.

Furthermore V-shaped defects, occurring in GaN epitaxial layers at threading dislocation sites during growth show only $\{110\bar{2}x\}$ planes [WSE+13]. Up to now, the origin of this observation is unclear and not covered in literature.

Analogous to the growth of surface hillocks, interface craters also increase in size with ongoing oxidation. With increasing temperature the vertical/horizontal oxidation ratio at

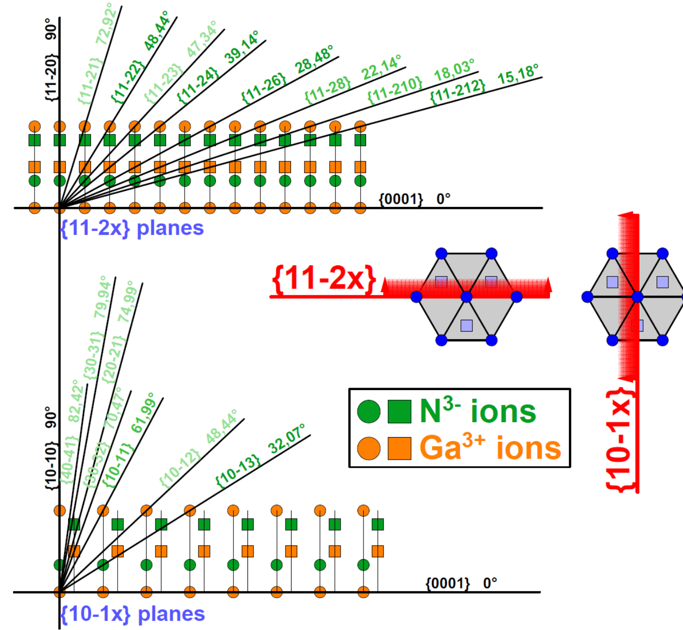

Figure 4.11: demonstration of $\{11\bar{2}x\}$ and $\{10\bar{1}x\}$ planes in GaN crystals suggest greater stability of $\{11\bar{2}x\}$ over $\{10\bar{1}x\}$ planes

defect sites increases, resulting in steeper craters and therefore rougher interfaces. The same is observed for increasing oxidation time, but to a lesser extent. This is demonstrated in fig. 4.9, which shows samples, oxidized at 900 °C for 10 min and at 1100 °C for 1 min. While the crater width of both samples is similar, the crater depth of the high-temperature-oxide is more than four times higher.

BULK OXIDE GROWTH:

Bulk Oxide Growth with Time:
Besides the growth of the superficial and interfacial structures, a rather uniform oxide layer is growing between these structures as well as on defect-free areas.

In some literature [WDM+00], the oxide growth is described to start with an oxynitride overlayer, on which discrete oxide crystallites form, which increase in size and eventually coalesce in order to form a uniform oxide layer. In this thesis a different approach is proposed:

First of all it has to be considered that the observation of the overall oxide layer growth is far more challenging than of surface hillocks and interface craters, especially in the early growth stage. The only available technique for thickness estimations is AES, which is only limited applicable for the thin inhomogeneous oxide layers, as described in detail in chapter 4.4. A reasonable way to compare oxide layer thicknesses is to analyze the O content's FWHM in AES depth profiles (fig. 4.12b), considering the continuous layer as well as in surface hillocks and interface craters contained oxide to some part. This thickness value is referred in the following to as “overall oxide thickness”. To exclude inaccuracy due to wrong sputter rates, values for thicknesses are given in mos (minutes of sputtering). For the thinnest oxide layers not only AES depth profiles but also surface spectra (fig. 4.12a) are

used for thickness estimations.

Unlike the linear increase of hillock and crater size at defect sites, the uniform oxide growth is strongly nonlinear and passes several stages as demonstrated in fig. 4.12b for oxidation at 900 °C:

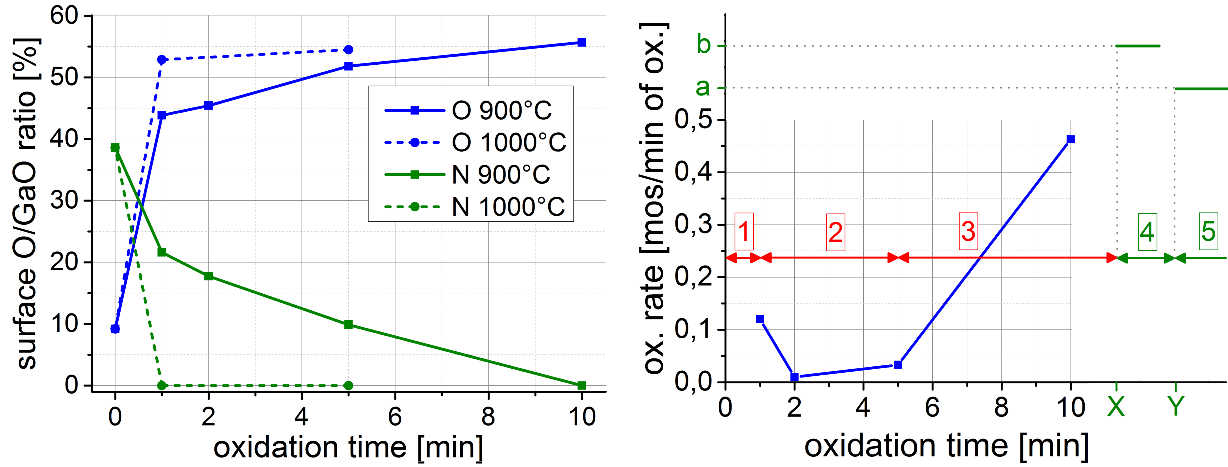

Figure 4.12: a) surface O and N concentration and b) oxidation rate* of GaN samples for oxidation at 900 °C as a function of the oxidation time; *oxidation rates based on FWHM in AES depth profiles; green lines are schematic (no quantitative values) and based on [ZAIS+08] [CZX+00]

1. As shown in fig. 4.12a, the oxygen concentration increases significantly already after oxidation for 1 min, which is accompanied by a decreasing N signal. Due to the small lateral size of the hillocks, as obtained in AFM analysis of the sample surface (fig. 4.5), they cannot solely cause the observed change in AES signal. Therefore the AES signal has to originate from the rise of an oxygen containing layer at defect-free areas. Since in AES surface measurements there is still a significant N signal, this layer thickness has to be below the information depth for N of 1.2 nm (tab. 5) in the range of few monolayers.

   This first increase in oxygen concentration is supposed to come from oxygen adsorption at the surface. The topmost Ga adlayer is expected to oxidize easily due to its chemically reactivity because of the missing N-bonds at the surface.

2. After the oxygen coverage of this first Ga adlayer, for ongoing oxidation GaN has to oxidize instead of Ga, requiring more energy and resulting in decreasing oxidation rates. In addition N and O have to diffuse through the overlying oxide layer but as observed in [ZAIS+08] [CZX+00] this should not be relevant in this early stage of growth.

   This leads to the low oxidation rate between 1 and 5 min. The oxide layer reaches a thickness that is observable in AFM only after 5 min (fig. 4.6b) and is still lower than 1.2 nm (fig. 4.12a).

3. Between 5 and 10 min, the N peak at the surface eventually vanishes and a significant oxide layer thickness is observed. Therefore detailed cross-sectional TEM- and

corrected (sec. 4.3.2) SEM-EDX analysis of the layers can be performed, which reveal a stoichiometry of 60±3% for all oxide layers, regardless of the thickness and spot within the structure. Even the surface and interface structures show no deviations in stoichiometry. Cross-sectional energy-filtered (EF) TEM and-TEM-EDX line-scans do not show N and O simultaneously, even for larger layers so that a possibly existing oxynitride layer does not exceed the lateral resolution of these methods. As observed in fig. 4.12b the oxidation rate at 10 min exceeds the oxidation before 5 min by a significant factor. Up to now, this observation has not been described in literature, probably because oxidation processes for comparable temperatures and times below 10 min are not covered. The reason for this observation is supposed to originate from defect-enhanced oxidation, which concerns more and more also defect-free areas as explained in the following:

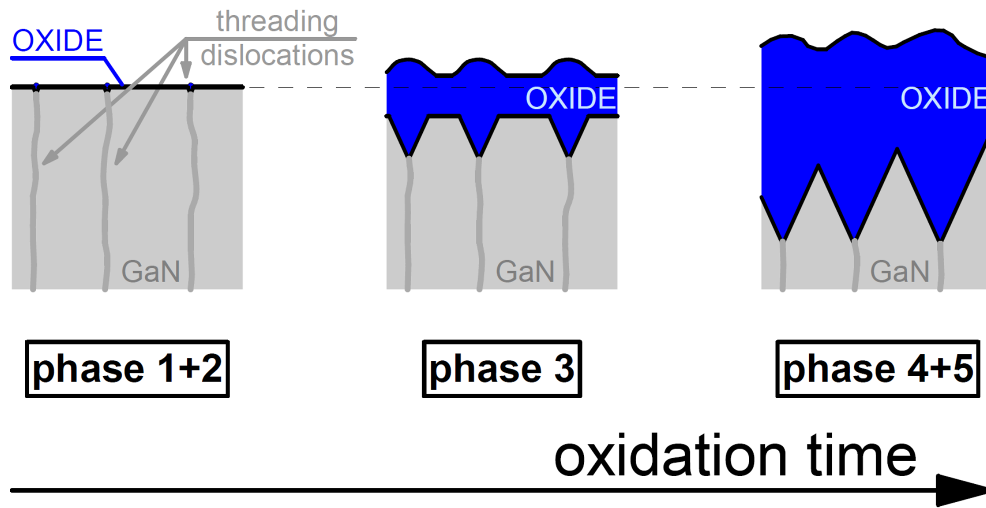

Figure 4.13: schematic oxide layers in different phases of oxide growth (fig. 4.12b) for the proposed oxide growth model

After the superficial O adsorption at defect-free areas, oxidation proceeds very slowly, while interface craters appear at dislocation sites in parallel. The crater depth increases linearly, but much faster than the overall oxide thickness. However, in the beginning the oxide volume in craters and thus rising surface hillocks is negligible compared to the overall oxide layer/adsorbate. Due to the pyramidic form of oxides, induced by the fast horizontal reaction rate, its volume increases not linearly but almost cubic with depth (fig. 4.12b). Due to the increasing steepness of craters the volume increase is less than cubic. However, this causes the fast progressive increase in oxidation rate. As observed in fig. 4.9b, craters after 10 min do not fully coalesce so that the rate is supposed to further increase until at some point (X in fig. 4.12b) all craters are fully coalesced.

4. When all craters are connected, the continuing oxidation rate is only limited by the vertical reaction rate at dislocations (fig. 4.13c), which induces a constant oxidation rate. The constant oxidation rate is confirmed by [ZAIS+08] [CZX+00], who investigated the oxidation rate for longer times (sec. 2.2.1).

5. For ongoing oxidation the oxide thickness reaches a point (Y in fig. 4.12b) where the oxidation reaction is not the limiting factor anymore but the diffusion through the oxide

layer [ZAIS+08] [CZX+00]. The subsequent oxidation rate is smaller but still constant. However, below 950 °C even after 6 [CZX+00] or 12 h [ZAIS+08] the oxidation rate is still observed to be reaction-limited. For increasing temperature, the transition time decreases but due to the short oxidation times within this thesis, diffusion-limitation can be excluded for all investigated samples [ZAIS+08] [CZX+00].

- Besides the enhanced oxidation at defect sites, another effect might lead to a progressive oxidation rate. Since oxidation of GaN is an exothermic reaction [JW13], it introduces a rise in temperature which leads to enhanced oxidation. The enhanced oxidation leads again to higher temperature and introduces thermal runaway [RKP+15]. However, the temperature increase does not exceed several °C, which cannot be responsible for the change the oxidation rate in the observed amount.

Bulk Oxide Growth with Temperature:
Besides the dependency of the oxide growth on the oxidation duration the second main parameter is the process temperature. Literature [OC12] [ZAIS+08] reports a threshold between 750 and 800 °C, where oxide growth starts and further follows an Arrhenius-law (eq. 2.2) [ZAIS+08] [OC12]. Due to the long oxidation times quoted in the literature, all data comes from the linear oxidation-time-region (region 4 or 5 in fig. 4.12b).

Due to the usage of RTA and the associated short oxidation time the temperature threshold for oxide growth cannot be determined directly since generated oxide layers are negligible compared to the adsorbed oxygen on the surface. However, due to the temperature dependence at higher temperatures (fig. 4.14) the threshold can be assumed to be in the region between 750 and 800 °C, as reported in the literature. Fig. 4.14 shows all obtained oxidation rates regardless of the oxidation-time-range in an Arrhenius-plot. The oxide growth seems to approximately follow an Arrhenius-law, distortions are supposed to originate from the different oxidation-time-ranges as shown in fig. 4.12b. It has to be considered that with increasing temperature the durations of oxidation-time-ranges decrease. Therefore comparisons are supposed to be more accurate for oxide layers of different oxidation temperatures with similar interface crater widths instead of similar oxidation times, since the crater width is assumed to be a better indicator for the oxidation-stage. The red values in fig. 4.14 are observed to have similar crater widths (fig. 4.9), therefore activation energy calculation is based on these samples. The activation energy can be directly gained from the slope in the Arrhenius plot (eq. 2.2). The observed value of 3.7 eV is in the range of literature data with 3.1 eV [OC12]. For more accurate values more data points for longer oxidation times would be required, but this is beyond the scope of this thesis.

Bulk Oxide Structure:
As shown in fig. 4.14, oxidizing at 1100 °C for 1 min delivers the thickest oxide layer, thick enough to be analyzed in cross-section by SEM and TEM (fig. 4.15). It clearly reveals the growth of about 140 nm deep interface craters at dislocation sites, an continuous oxide layer of about 100 nm thickness and up to 80 nm high surface hillocks on top. The coalescence of surface hillocks and the existence of the continuous oxide layer lead to a surface where hillocks are no longer directly above craters. The additional fact that the TEM-lamella is only 50 nm thick explains why the TEM image in fig. 4.15b does not contain a surface hillock.

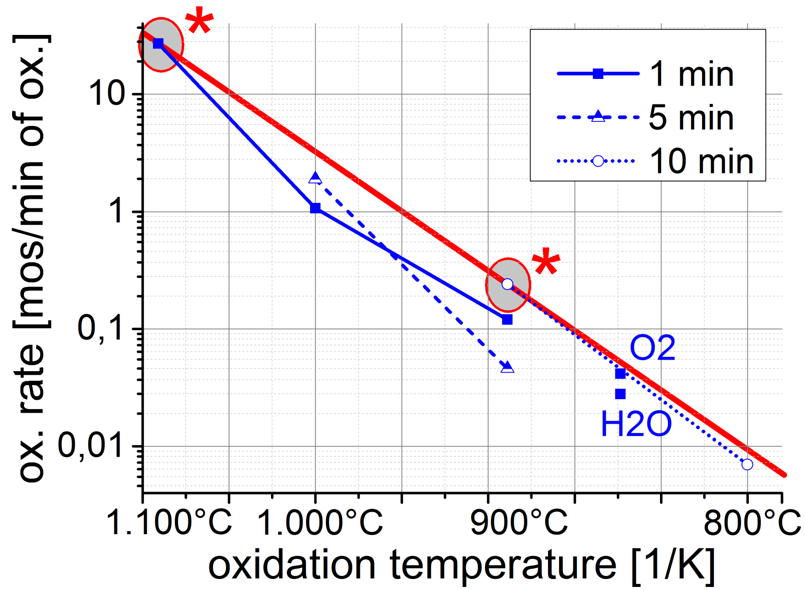

Figure 4.14: Arrhenius plot: oxidation rate (FWHM in AES depth profiles) as a function of the oxidation temperature (for various durations); "H2O" and "O2" are referred to wet and dry oxidation in the horizontal oven; *calculation of activation energy based on these data giving a value of 3.7 eV, as represented by the red line

This thin lamella makes it possible to clearly distinguish between two different structures (fig. 4.15b), which have not been reported yet. The topmost layer is a homogeneous oxide with a thickness of approximately 40 nm, which includes also the surface hillocks. The entire oxide layer beyond this limit in interface near regions including craters forms a porous inhomogeneous layer, filled with up to 50 nm large voids. TEM-EDX measurements reveal that voids are empty and more accurately, Raman spectroscopy shows that they are filled with N_2 or O_2. With ongoing oxidation the homogenous oxide layer thickness on top stays rather constant while the inhomogeneous layer thickness increases.

Voids are assumed to come from an enhanced decomposition rate of GaN that exceeds the diffusion rate of N_2, especially at threading dislocations (see sec. 4.2.2). Decomposition generates metallic Ga, which oxidizes during the further procedure, and gaseous N_2. If N_2 diffusion rates are lower than the decomposition rate, voids are formed. This might also be related to the observation of pits in the center of surface hillocks after oxidation at 900 °C for 10 min as shown in SEM-images in fig. 4.16. The volume increase due to the limited diffusion of N_2 might “crack” the overlying oxide layer to build a path for N_2 molecules to reach the atmosphere. Furthermore, it appears that voids are connected to ensure a direct path from newly created voids to atmosphere. As most material decomposes at craters at dislocation sites, pits are located in the center of surface hillocks.

It further has to be considered that probably not all oxide is formed at the interface but that some Ga diffuses to the surface and oxidizes there. This explains why no cracks occur despite the volume expansion of 40% [CZX$^+$00] during oxidation. A strong indication for this assumption is the Al concentration in depth profiles of oxidized AlGaN samples as shown in fig. 4.17:

The untreated reference sample as well as samples processed at 900 °C, which show negligible oxidation, reveal an Al concentration (Al/(Ga+Al)) of 25-30% (fig. 4.17) and a FWHM

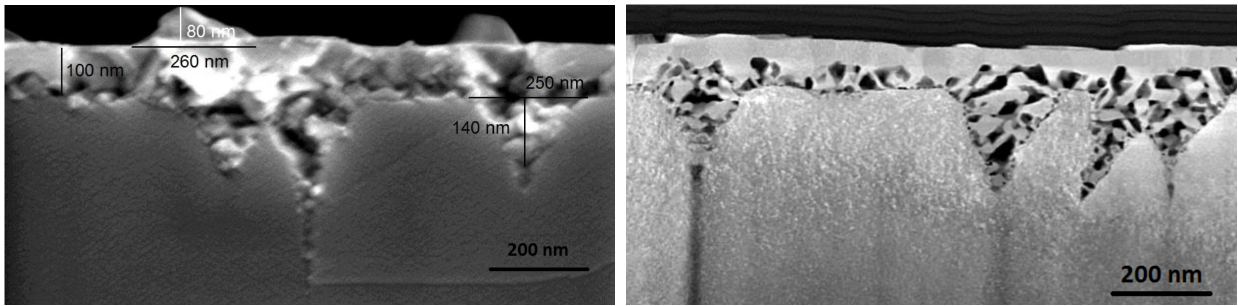

Figure 4.15: cross-sectional a) SEM and b) dark-field TEM analysis [RKP+15] of a GaN sample oxidized at 1100 °C for 1 min

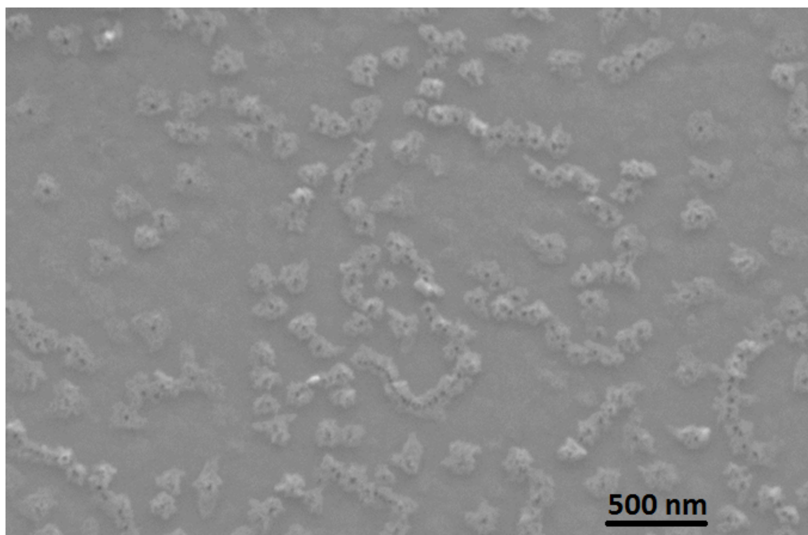

Figure 4.16: SEM and EDX analysis of the GaN surface after oxidation at 900 °C for 10 min

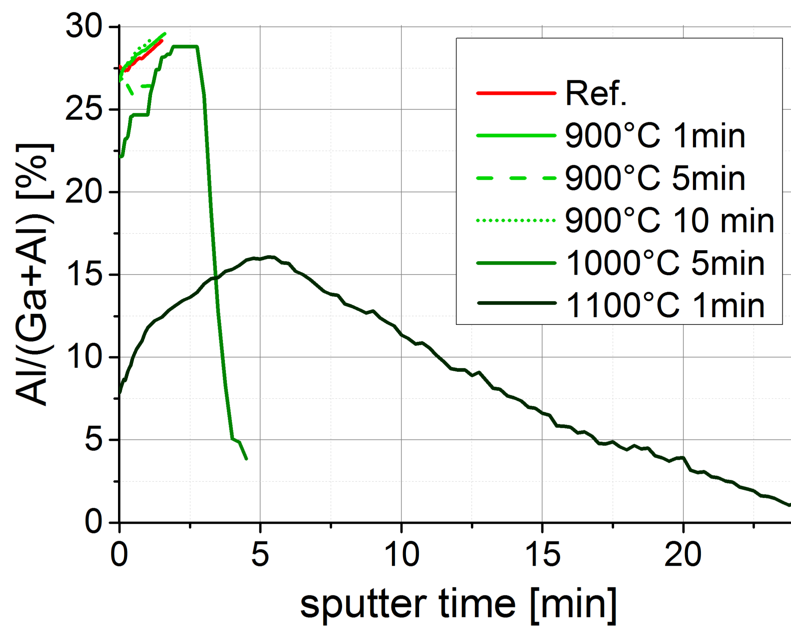

Figure 4.17: Al/(Ga+Al) ratio for AlGaN samples oxidized at different temperatures for various times

of approximately 2.8 mos (not shown). As explained in sec. 4.3.1 the Al concentrations are not corrected and show enhanced values. With increasing oxide thickness the Al concentration decreases and reaches deeper into the material in terms of higher mos. It has to be considered that the sputter rate in oxidized material is only half that of untreated AlGaN so that the FWHM should be doubled. However the Al-FWHM of the 1100 °C oxidized sample is at approximately 15 mos, which is a factor of 6 instead of 2. This discrepancy as well as the lowered Al concentration, especially at the surface and its development with sputter time suggest the Ga-diffusion assisted oxide growth:

In the beginning the oxidation proceeds analogous to GaN oxidation until at some point the entire AlGaN layer is converted and the underlying GaN layer starts to oxidize. Since the GaN layer does not only oxidize at the interface, but Ga is assumed to further diffuse to the surface, superficial Ga_2O_3 without Al content forms. After 1 min of oxidation the overall oxide layer is only slightly thicker than the former AlGaN layer so that only a negligible Al-free layer covers the Al-containing oxide at defect free areas and AES still recognizes Al at the surface. Craters at defect sites are much deeper so that from these sites already at early stages only Ga diffuses to the surface and hillocks therefore contain less Al. This explains the low Al concentration down to deep regions in the AES depth profiles. As in the beginning of profiling the superficial continuous layer and hillocks are sputtered, only low Al concentration is observed. With increasing sputter time the Ga_2O_3 adlayer is sputtered away and more Al containing oxide contributes to the signal causing increased Al concentration. After 5 mos the continuous oxide layer starts in some regions to be entirely sputtered and more and more only the Al containing oxide below former hillocks remains, resulting in the slow decrease of the Al concentration. After approximately 25 mos only pure Ga_2O_3 in craters remains up to 40 mos, fitting well to the depths of craters observed in SEM and AFM.

AlGaN:

Besides obtaining the oxidation behavior of GaN, the main scope of this thesis, the influence of an additional AlGaN barrier layer, as used for HEMTs, is examined. The procedure is analogous to the investigation of GaN samples, but it has to be considered that the superficial AlGaN layer is only few tens of nm thick.

The most significant difference to GaN is the higher resistivity against oxidation. Oxidation starts at higher temperatures and has lower oxidation rates. While for GaN samples oxidation at 900 °C causes the rise of hillocks at dislocation sites already after 1 min, AlGaN shows no significant surface alteration until 10 min of oxidation (fig. 4.18). However, eventually hillocks rise, which increase in size and coalesce to form a rough surface. The dislocation density of initial samples is several times higher than in GaN and furthermore the hillock density is also significantly higher than the dislocation density. In contrast to GaN their distribution is rather random over the surface (fig. 4.18). Some rise at surface pit sites, but not exclusively and not every pit is covered by a hillock. This suggests no or less enhanced oxidation. The shape of hillocks is analogous to GaN and also triangular structures are found, indicating high crystallinity. The increase of the hillock height with temperature is shown in fig. 4.19.

As in GaN, oxidation of AlGaN causes craters at the oxide/semiconductor interface, whereby their form is different. The investigation of interface structures is complicated by severe etching artifacts that inhibit obtaining oxide/AlGaN interfaces as explained in sec. 4.2.3. Solely the interface gained after oxidation at 1100 °C is supposed to be free of artifacts as

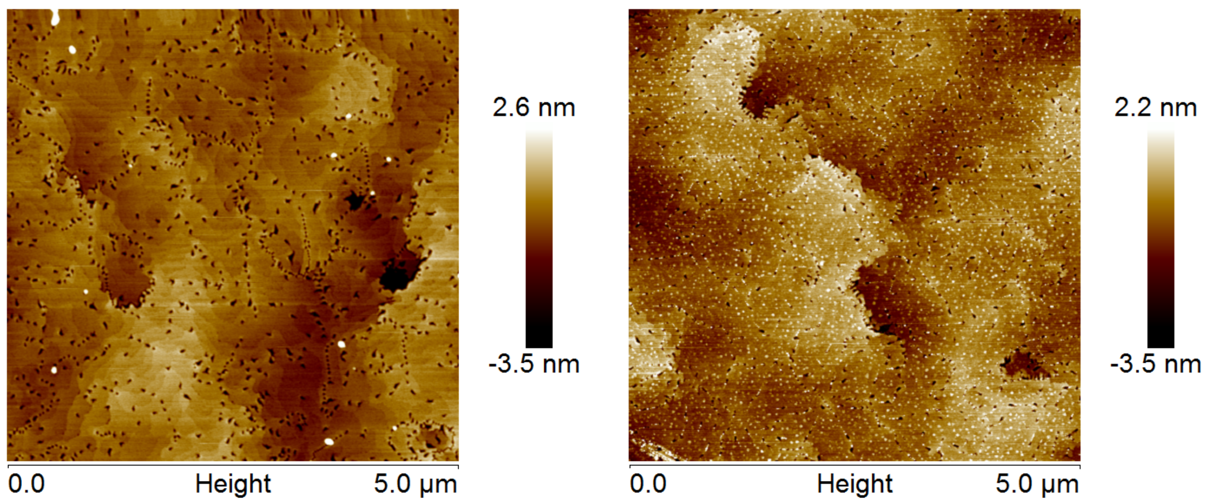

Figure 4.18: AFM analysis of the AlGaN surface after oxidation at 900 °C for a) 1 min and c) 10 min

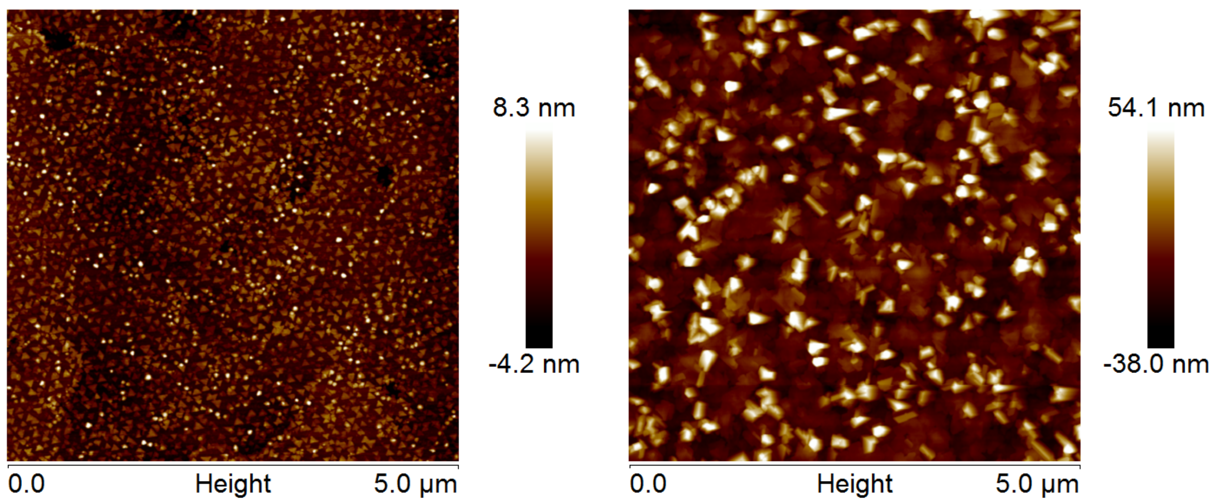

Figure 4.19: AFM analysis of the AlGaN surface after oxidation for 1 min at a) 1000 °C and b) 1100 °C

the oxide layer is thicker than the AlGaN layer and the interface is a Ga_2O_3/GaN interface. This is confirmed by AFM images (fig. 4.20) as well as AES and cross-sectional SEM data (fig. 4.21). Although AFM analysis of the sample oxidized at 1100 °C shows the Ga_2O_3/GaN interface instead of an interface in the AlGaN layer, information on oxide/AlGaN interfaces can be gained. Instead of hexagonal shaped craters, two different crater forms are observed:

There are long and broad crater lines with no preferred orientation, meaning that they do not follow any crystal planes. It is assumed that these structures are the dominant structures at oxide/AlGaN interfaces. This is encouraged as the same structures are found after decomposition studies (sec. 4.2.2).

Within these crater lines there are steep craters, which are assumed to appear because of the limited thickness of the AlGaN layer. As with ongoing oxidation after a certain oxidation time crater lines in AlGaN reach the AlGaN/GaN interface and GaN oxidation is enhanced at dislocation sites, within these crater lines singular craters appear at dislocations. Crater depths are much larger than the AlGaN layer thickness and exceed 100 nm, comparable to crater depths in GaN.

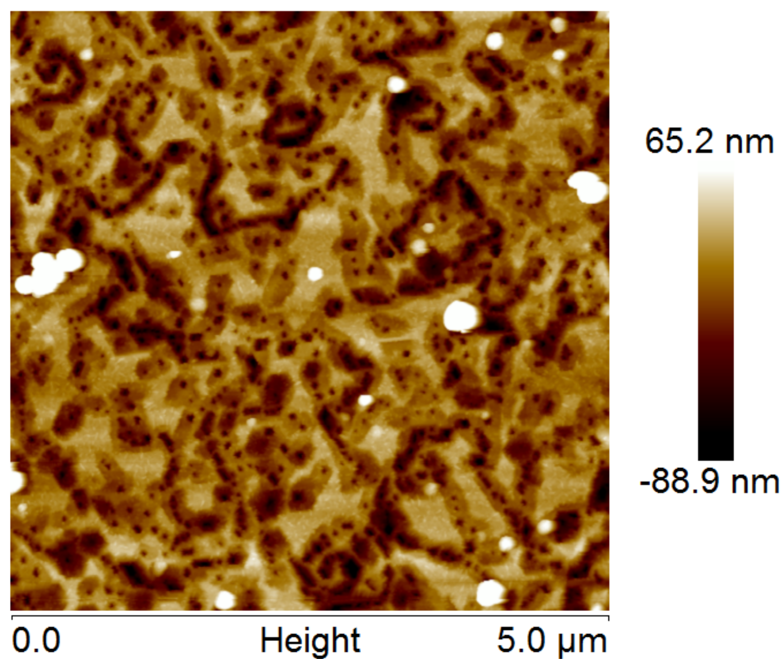

Figure 4.20: AFM analysis of the oxide/semiconductor interface after oxidation at 1100 °C for 1 min and oxide removal

Due to the small AlGaN layer thickness, gaining information on the nature of the uniform oxide layer is challenging. In order to perform cross-sectional SEM analysis, layers have to be tens of nm thick. In fig. 4.21 an at 1100 °C for 1 min oxidized sample is shown, where the uniform oxide thickness is slightly larger than the former AlGaN barrier. Analogous to GaN a homogeneous oxide layer is found near the surface, while interface near regions and craters consist of an inhomogeneous structure perforated with voids as in GaN. However it is not clear if these voids just appear in the GaN layer or also in AlGaN on top.

AES depth profiles reveal that within the oxide layer, shown in fig. 4.21, the entire Al part is oxidized, as indicated by a shift of the Al peak in AES spectra (fig. 4.40). Beyond the Al containing oxide there is further a thin layer of Al-free oxide found. XPS analysis

on less oxidized AlGaN layers (900 °C, 10 min) reveal that with increasing sputter depth within the oxide the ratio of the bondings Ga-O and Ga-N decreases significantly faster than the ratio between Al-O and Al-N bondings. Therefore, although AlGaN is more resistant against oxidation than GaN, the AlN part within the AlGaN compound is easier oxidized.

The higher oxidation rate of GaN is assumed to originate from the enhanced oxidation at threading dislocations, whose influence on the oxidation is observed to be different in AlGaN. Furthermore detailed investigation thicker AlGaN layers are required, but with the used structure the AlGaN layer cannot be extended as cracks would occur due to the differences in the lattice constant of AlGaN and GaN.

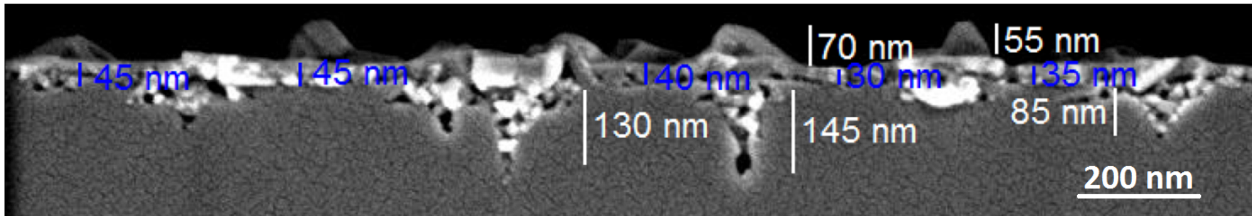

Figure 4.21: cross-sectional SEM analysis of an AlGaN sample after oxidation at 1100 °C for 1 min

b) Horizontal Oven:

Within this thesis a horizontal oven is used for long term experiments with annealing durations of 30 min up to several hours. Instead of wafer fragments, entire wafers have to be processed and for comparison with RTA it has to be considered that the oven form might influence the outcome significantly.

Besides standard oxidation in pure O_2 gas, which is referred to as “dry” oxidation, “wet” oxidation with additional H_2O-vapor is performed as well as oxidation in N_2O.

DRY OXIDATION:

In RTA investigations the oxidation rate even for the longest possible durations is still increasing with increasing processing time so that in order to reach saturation (region 4/5 in fig. 4.12b) longer oxidation times of 240 min are performed in the horizontal oven. The drawback of this annealing method is the low upper temperature limit of 850 °C.

The surface after oxidizing (fig. 4.22) looks similar to oxidation in RTA with the characteristic oxidic hillocks. Their oxidic nature is confirmed by EDX measurements. Taking exponential growth with temperature and linear growth with time into account as observed in RTA, hillocks are much smaller than expected. It is assumed that due to the coalescence of hillocks their growth saturates increasingly.

Surprisingly, the oxide/GaN interface (fig. 4.23a) surprisingly shows different structures than the ones observed in RTA. Instead of the hexagonal basis, craters show large parallelogram-shaped craters with depths exceeding 200 nm, even deeper than for the sample oxidized at 1100 °C for 1 min.

It is not clear if these structures are related to etching artifacts (sec. 4.2.3). While AES depth profiles confirm the existence of deep craters, they cannot be observed in SEM cross-sections (fig. 4.23a).

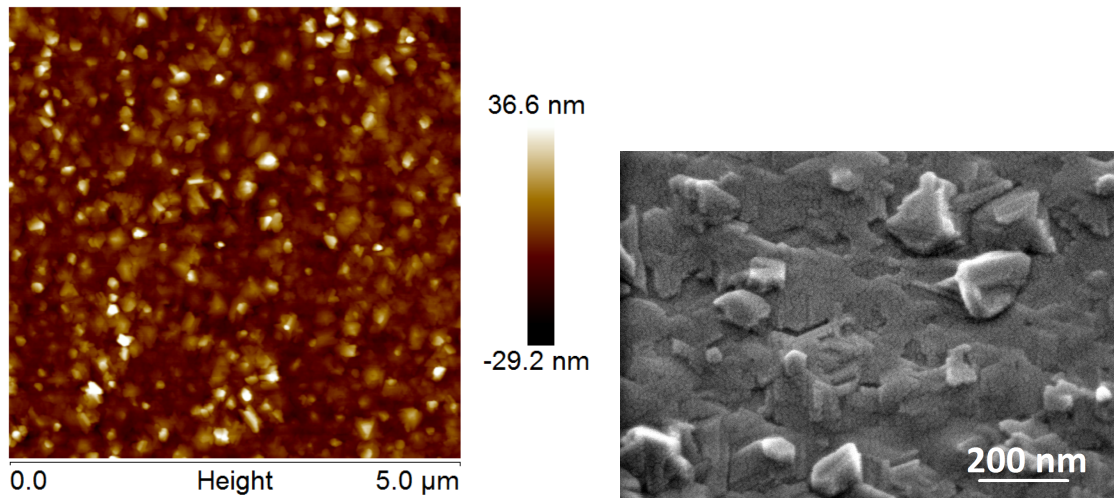

Figure 4.22: a) AFM and b) SEM analysis of the GaN surface after oxidation in horizontal oven at 850 °C for 240 min

The uniform oxide layer has a thickness of approximately 35 nm, fitting well to a calculation based on an Arrhenius-temperature and linear-time behavior. This supports the constant-oxidation-rate-model for long oxidation times as found in literature [OC12] [ZAIS+08] [CZX+00].

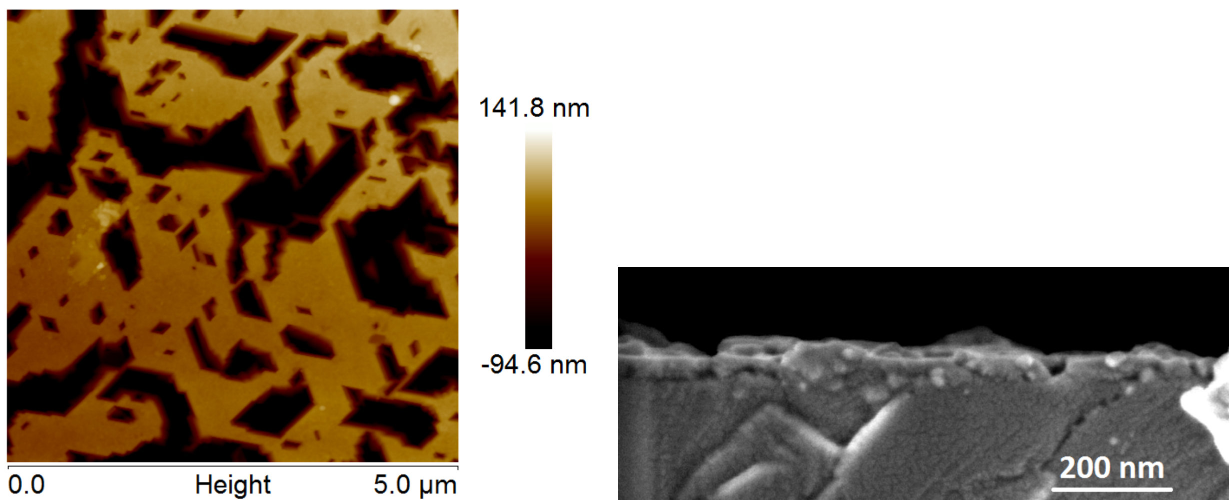

Figure 4.23: a) AFM analysis of the Ga_2O_3/GaN interface after oxide removal and b) cross-sectional SEM analysis after oxidation in horizontal oven at 850 °C for 240 min

AlGaN:
Oxidation of an AlGaN layer results in the surface being covered by flat equilateral triangles with an edge length of approximately 450 nm as shown in fig. 4.24a. They are all oriented in the same direction or its mirrored form. The triangles look like ramps, whereby one corner point forms the top and the two adjacent edges are covered by several round hillocks which are higher than the ramp. The entire surface is covered by these structures and no special distribution is observable.

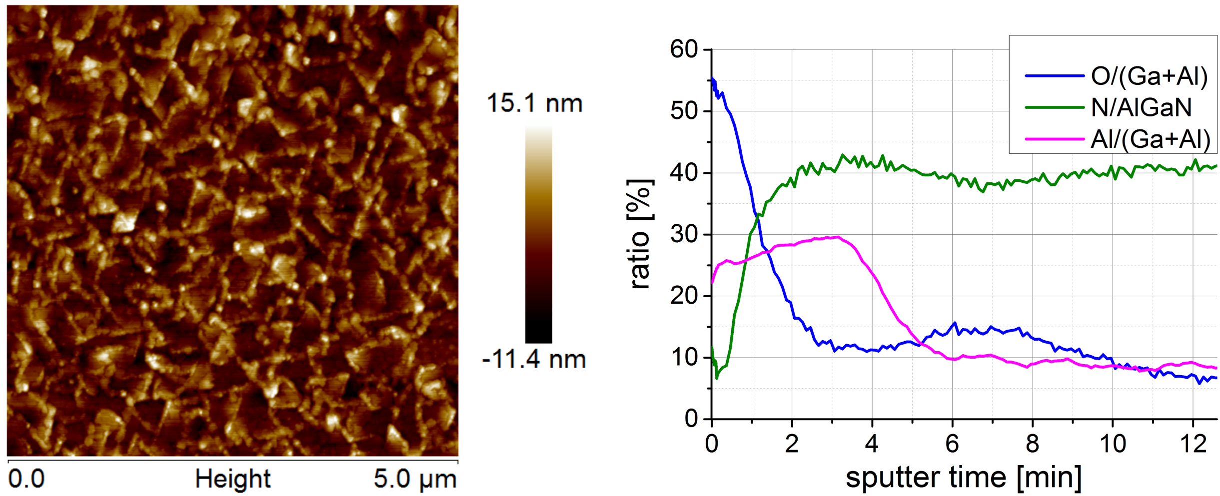

Figure 4.24: AlGaN sample after oxidation in horizontal oven at 850 °C for 240 min: a) AFM analysis and b) AES depth profile

The AES depth profile in fig. 4.24b reveals that the uniform oxide layer with approximately 1 mos has a thickness of about a quarter of the AlGaN barrier and only a fraction of the thickness observed for GaN. There are even areas with thicknesses not exceeding the information depth of AES for N of 1.2 nm.

On the other hand, fig. 4.24b reveals the existence of laterally small but very deep interface crater structures exceeding 12 mos. Due to etching artifacts, the obtained AFM images (fig. 4.34) are unlikely to represent the actual oxide/semiconductor interface and the form of these interface crater structures is unknown.

WET OXIDATION:
By adding H_2O vapor to the annealing chamber, Oon et al. [OC12] reports a oxidation rate higher by a factor of 15. This cannot be confirmed within this investigation where processing at 850 °C for 60 min results in an uniform thickness falling below the information depth of AES of 1.2 nm. Besides, there are large oxide structures at the surface and interface, containing almost the entire oxide volume. The large thickness of surface and interface structures compared to the overall thickness gained in wet against dry oxidation is impressively shown in AES depth profiles in fig. 4.26b.

The surface is covered by distinctive, randomly distributed, equilateral-triangle-shaped terraces with edge lengths up to 150 nm and heights up to 50 nm as shown in fig. 4.25. EDX analysis confirms the oxide nature of the triangular structures as well as the small thickness of the overall oxide thickness on structure-free smooth areas.

The oxide/GaN interface (fig. 4.26a) exhibits a far higher roughness in wet processes, as also found by Readinger et al. [RWW+99]. The tremendous roughness originates from large protrusions and potholes, which do not show straight edges or a distinguished distribution as for dry oxidation. It cannot be excluded that the observed interface is a result of severe etching artifacts, but AES depth profiles confirm the existence of craters, covering a similar area with depth in the obtained range.

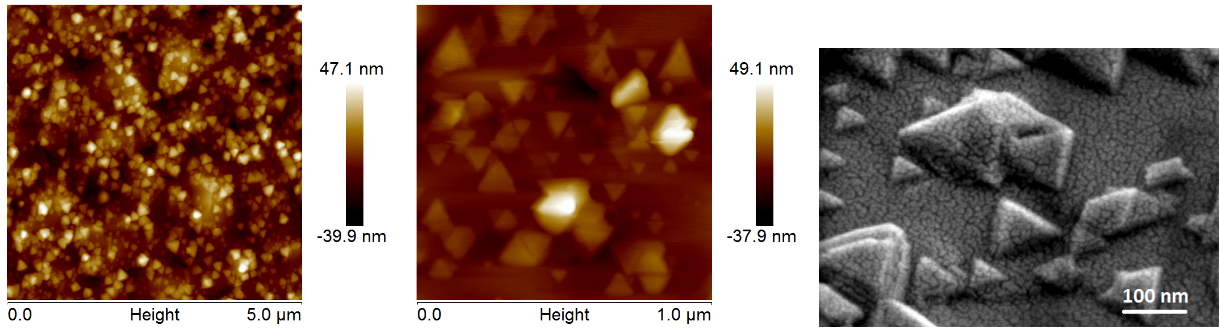

Figure 4.25: a+b) AFM and c) SEM analysis of the surface of GaN samples oxidized in a wet oxidation process at 850 °C for 60 min

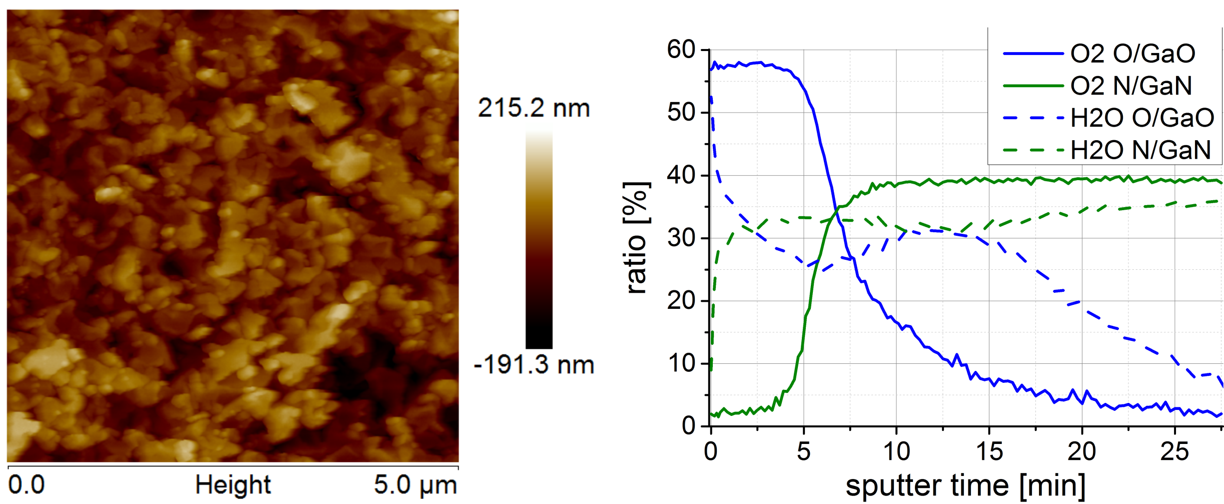

Figure 4.26: GaN sample oxidized in a wet oxidation process at 850 °C for 60 min: a) AFM analysis of the oxide/GaN interface and b) AES depth analysis

AlGaN:
The surface of the oxidized AlGaN sample looks similar to the dry process with their triangular ramps and heights of up to 50 nm, but they are laterally larger with typical length of 500 nm as shown in fig. 4.27.

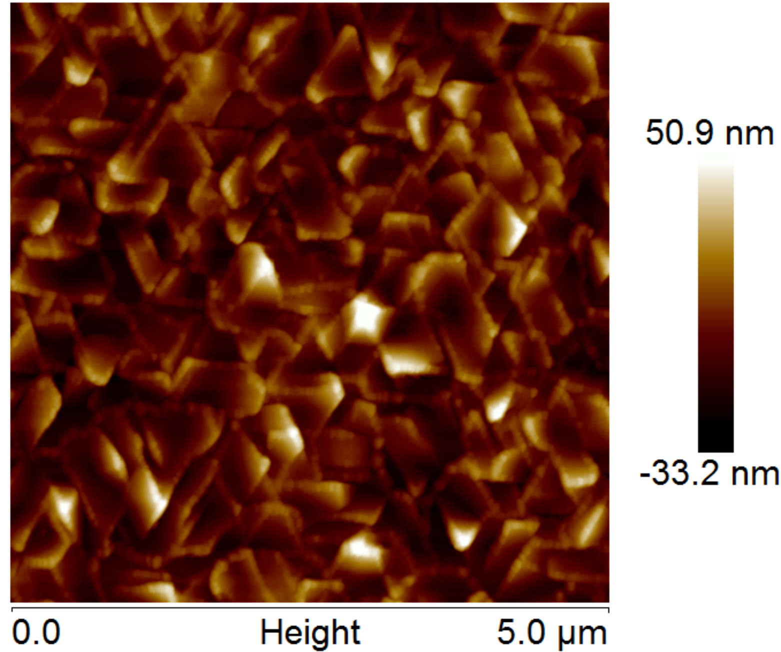

Figure 4.27: AFM analysis of the surface of an AlGaN sample oxidized in a wet oxidation process at 850 °C for 60 min

Etching artifacts inhibit AFM imaging of the interface, but comparison of AES depth profiles (fig. 4.39b, fig. 4.26b) suggests similar interface structures as for GaN, but of approximately half the depth. The uniform oxide layer is comparable to the GaN sample below 1.2 nm.

OXIDATION IN N_2O:
Besides wet oxidation also oxidation in N_2O is reported to enhance the oxidation rate [OC12]. Unfortunately due to the horizontal oven design the process is limited to a maximum temperature of 800 °C, processing duration of 30 min and a pressure of 350 mTorr.

Fig. 4.28 demonstrates that no sample shows surface alterations observable by AFM. AES depth profiling reveals an increase of the oxygen concentration on the very surface but only within less than 1 nm. The enhanced concentration is likely to origin from adsorbing oxygen.

The discrepancy between the literature [OC12] and data within this thesis is probably a result of the low chamber pressure. Due to the low pressure of 350 mTorr desorption of N_2 might be enhanced but on the other hand too little molecules are present to participate in the actual reaction.

It is notable that oxidized GaN samples reveal lower oxygen concentration than AlGaN samples. It is assumed that although GaN oxidizes easier, adsorbation is proceeding faster on AlGaN.

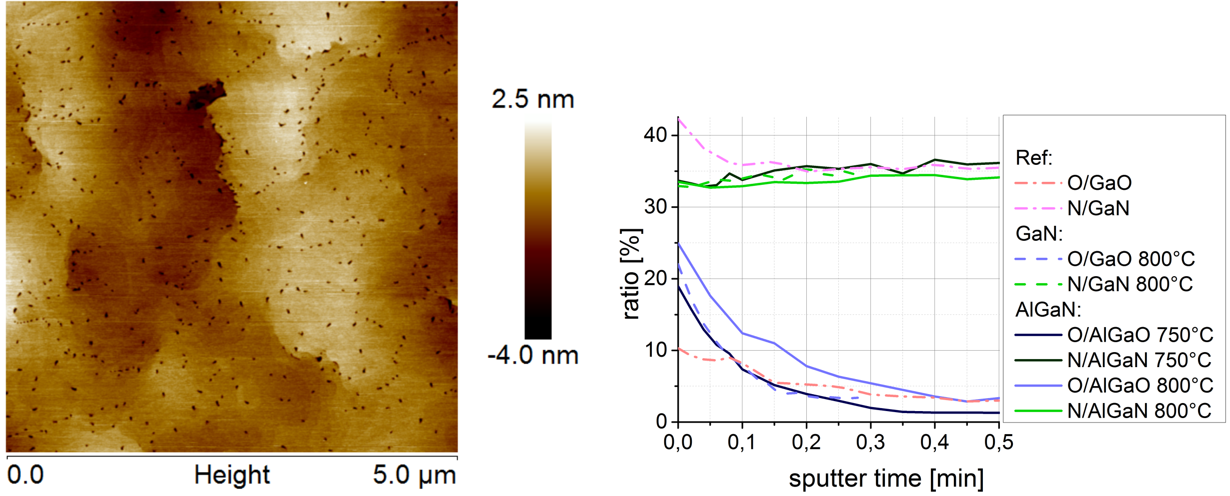

Figure 4.28: oxidation of GaN and AlGaN in N_2O at 750 and 800 °C for 30 min: a) AFM analysis and b) AES depth profiless

Plasma Oxidation

Analogous to RTA plasma processes can be performed for wafer fragments so that besides all RTA samples also all samples for plasma oxidation originate from the same wafer, excluding influences from differences in the initial material.

Processing properties as well as the gained oxide thickness are listed in tab. 3 and compared to literature data.

RF power [W]	RF frequency [MHz]	chamber pressure [Torr]	gas flow rate [sccm]	temperature [°C]	time [min]	oxide thickness [nm]
60	13.56	10^{-6}	100	300	60	200
700	2450	10^{-3}	12	150-200	20	10
60	13.56	0.3	O_2: 20, He: 200	250-300	30	3.5
900	**13.56**	**1.2**	**5000**	**300**	**5**	**1.5**

Table 3: process conditions for plasma oxidation and the resulting oxide thicknesses from literature data (first three rows) [LKS+08] [PMR+03] [Bae03] and from investigations within this thesis (fourth row); green fields mark saturation durations

As for oxidation in N_2O, process conditions were not harsh enough to cause surface alterations, observable by AFM. AES analysis (fig. 4.29) reveals a relatively homogenous oxygen-containing layer of up to 1 or 2 nm. As the thickness increases only insignificantly between 5 and 20 min, saturation can be assumed to be achieved already between 1 and 2 nm. This saturation phenomenon is found by various authors at different oxidation times and oxide thicknesses, depending on their process parameters (tab. 3).

Since plasma oxidation can be affected by many parameters it is not apparently clear which one is the limiting factor. However, the data in tab. 3 suggests that with decreasing pressure the oxide thickness as well as the saturation time increases. This might correlate with

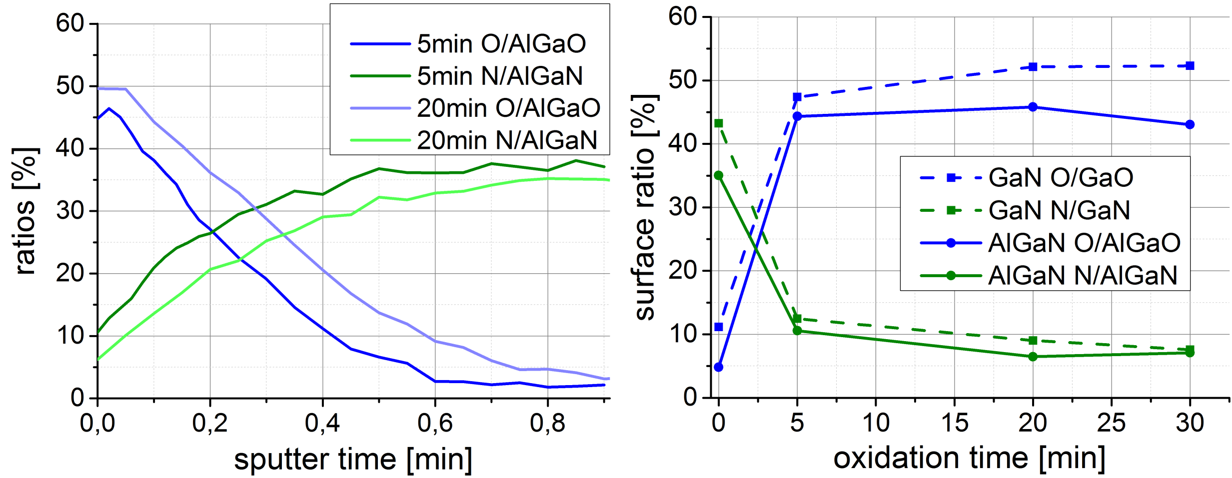

Figure 4.29: GaN and AlGaN samples oxidized in plasma oven for various oxidation times: a) AES depth profiles and b) surface analysis

enhanced GaN decomposition and N desorption but a consistent model is currently lacking.

As for N_2O processes, plasma oxidation shows slightly enhanced oxygen concentration for AlGaN compared to GaN. This origins probably from the thin oxygen containing layers, where only adsorption occurs. Furthermore it has to be considered that the higher temperature threshold for AlGaN is no criterion for plasma oxidation as the reaction is not thermally controlled.

4.2.2 Decomposition

As decomposition of GaN is supposed to play a major role for its oxidation, this phenomenon is investigated separately by annealing samples in N_2 and NH_3 in RTA ovens. It is expected to help clarifying the role of dislocations for the oxidation process by revealing if decomposition is enhanced at dislocation sites.

N_2:
Annealing of GaN and AlGaN samples at 900 °C for 1 min does not cause any surface alteration, observable in AES and AFM. Direct comparison of dislocation pits on the surface shows that not even these spots are harmed.

Increasing the processing temperature to 1100 °C on the other hand leads to severe surface alteration, observable with the bare eye. Microscopic analysis (fig. 4.30) reveals the emergence of large-sized droplet-like structures. EDX analysis in fig. 4.31 exhibits that these droplets consist of pure Ga and since no N signal is remaining the hillock height has to exceed the information depth for Ga of approximately 70 nm. It has to be considered that this observation is made on an only 3 μm broad droplet and large droplets have diameters of up to 10 um, therefore their height can be expected to be much higher than 70 nm. The liquid nature of Ga droplets is confirmed as they can not only be etched away, but also easily wiped away for instance with cotton sticks or washed off with H_2O. The observed O concentration in EDX analysis originates from oxidation of surface near Ga. Since Ga oxidizes easily, pure

Ga is not stable in open air and therefore there will always be a superficial oxide layer on Ga droplets, if exposed to ambient air.

The liquid nature of these droplets inhibits analyzing droplets in cross-sections as well as AFM analysis.

The topography of the solid GaN below Ga droplets partly follows the droplet-covered surface. Regions covered by large droplets form rather flat plateaus with a concave bow, protruding approximately 150 nm from the surroundings. Despite the concave bow, borders have enhanced heights of up to 50 nm.

The observed topography can be explained by the GaN decomposition model of Pisch et al. [PSF98]. Decomposition takes place at the GaN/Ga interface on the edge of a droplet, probably because liberation of N_2 is easier. Once a droplet of sufficient size exists above the GaN surface, this region is decomposing to a lesser extent, leading to the enhanced height of the plateaus under droplets. Since outer areas of droplets are later covered by the droplet, they decompose for a longer time and cause the concave bow. Ga droplets do not exclusively grow in size by decomposition but also by coalescence so that especially smaller droplets are not perfectly round.

An interesting observation is that there is not only the region with large droplets but three different ones referred to as “inner zone”, “intermediate zone” and “outer zone”. The approximately 1 mm broad intermediate zone shows same characteristic as the inner zone but with smaller droplets. The outer zone reveals optically no structures at all and SEM and EDX analysis exhibit small oblong meander-shaped structures without oxygen and gallium droplet coverage.

The origin of these zones is likely to be related to a temperature gradient during processing or cooling down, but a comprehensive model is outstanding.

Due to the large size of droplets and their strong influence, no information is gained on the role of dislocations for decomposition. Further experiments could be performed at temperatures between 900 and 1100 °C in order to find a temperature where resulting droplets are in an appropriate size to draw conclusions about the role of dislocations. However, it seems more reasonable to change the atmosphere in order to prevent Ga droplet formation and their associated distortions.

NH_3:
While only N desorbs in N_2, leaving behind liquid Ga on the surface, in NH_3 not only N but also Ga can desorb, probably by forming gaseous gallium hydroxides. This guarantees that the decomposition reaction is not distorted by any byproducts. For observable decomposition low pressure is required, fig. 4.32 shows an AlGaN sample annealed at 700 °C at 235 mTorr for 30 min. Decomposition is clearly seen to occur at dislocation sites causing the transition of point-like pits to oblong craters. This fits perfectly to the oblong craters described for the oxide/AlGaN interface after oxidation. Therefore it is assumed that the faster oxidation at dislocation sites originates from enhanced decomposition.

Besides the standard oxidation reaction of GaN (eq. 4.1), decomposition initializes an alternative way of oxidation (eq. 4.2)). Therefore GaN decomposes, whereby N_2 desorbs and the liquid Ga remains and is in further consequence oxidized with an enhanced oxidation rate. The higher negative reaction enthalpy causes increased temperature and further enhanced oxidation.

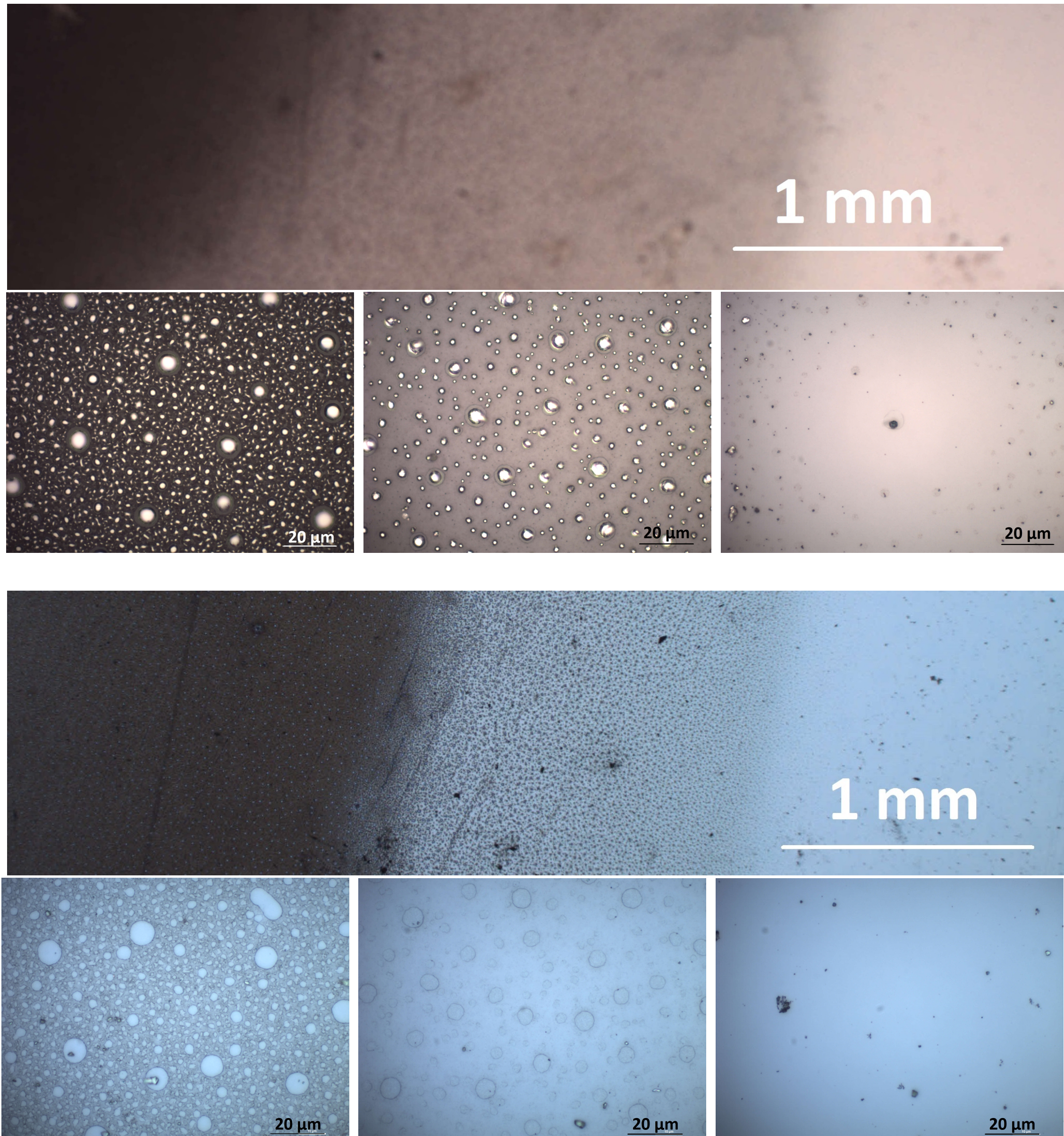

Figure 4.30: optical analysis of GaN surfaces after annealing in N_2 at 1100 °C for 1 min reveals severe decomposition and due to enhanced desorption of N over Ga remaining liquid Ga droplets, whose sizes decrease near the sample's edge (inner/intermediate/outer zone from left to right); top/bottom: before/after droplet removal

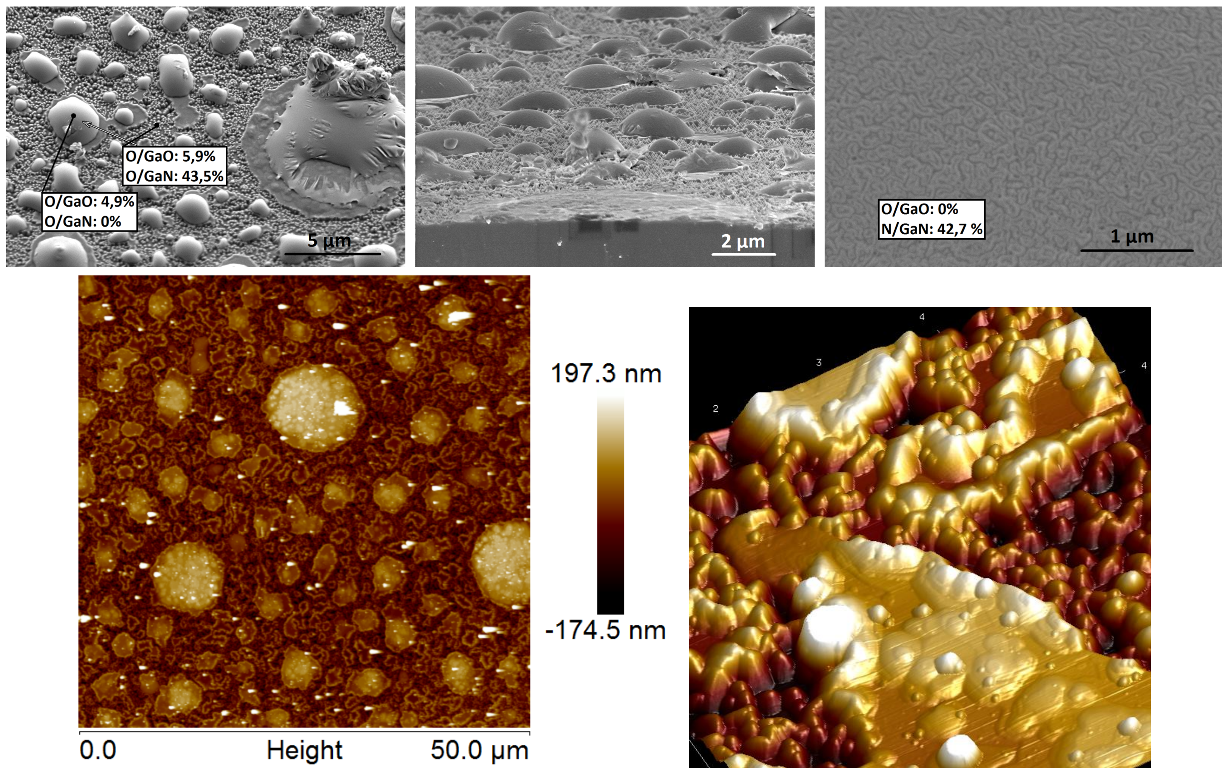

Figure 4.31: GaN surface after annealing in N_2 at 1100 °C for 1 min: top: SEM and EDX analysis of the inner (a+b) and outer zone; bottom: AFM analysis after liquid droplet removal

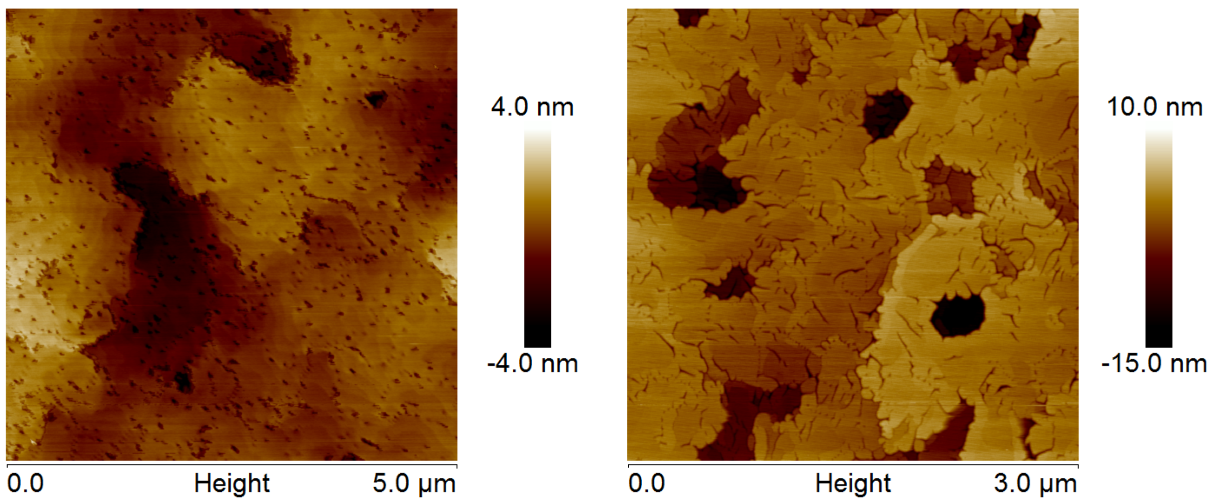

Figure 4.32: AFM analysis of a) an untreated AlGaN reference sample and b) annealed in NH_3 at 700 °C at 235 mTorr for 30 min

$$4\,GaN(s) + 3\,O_2(g) \Rightarrow\ 2\,Ga_2O_3(s) + 2\,N_2(g) \qquad \Delta H_{\Theta} = -343 kJ/mol \quad \text{[JW13][RTN}^{+}\text{00]} \tag{4.1}$$

$$\begin{aligned} &1. \quad Decomposition:\ 4\ GaN(s) \Rightarrow\ 4\ Ga(l) + 2\ N_2(g) \\ &2. \quad Oxidation:\ 4\ Ga(l) + 3O_2(g) \Rightarrow\ 2\ Ga_2O_3(s) \quad \Delta H_{\Theta} = -1092 kJ/mol \quad \text{[Hay10]} \end{aligned} \tag{4.2}$$

4.2.3 Oxide Removal/Etching Artifacts

Oxide removal is performed in hot HCl, which is observed to not harm raw GaN and AlGaN surfaces remove the entire oxide layer. However, after etching the surface is revealed to be not compulsory the former oxide/semiconductor interface. As no remaining oxide is found in AES depth profiles it can be concluded that in some samples etching proceeds in the semiconductor below the oxide although the raw semiconductor surface is not harmed. An explanation for this observation is currently missing.

For its clarification three different RTA processes are performed at different temperatures for two comparable samples. These samples are from the same region of the wafer, oxidized simultaneously adjacent to each other in the same process and etched in the same baker.

However, for GaN samples, these two samples show significantly different behavior (fig. 4.33). Additional AES, cross-sectional SEM and TEM analysis fit perfectly to the images in the bottom of fig. 4.33 so that these are considered as actual oxide/GaN interface. Images at the top look like the negative of the surface after a low temperature process. No structures show remaining oxygen so that incomplete etching can be excluded.

For AlGaN, the two investigated samples for every process show the same structures but nonetheless none of them shows an oxide/AlGaN interface. AES depth profiles exhibit no remaining Al concentration after etching, even if the oxide thickness is far smaller than the AlGaN layer. This means that not only the oxide is etched but also the entire AlGaN layer, although the raw AlGaN layer is seen to be resistive against etching.

As for the process at 1100 °C the entire AlGaN layer is oxidized and the oxide/semiconductor interface is entirely in the GaN buffer, this interface can be considered as artifact-free, as confirmed by cross-sectional SEM. As the crater depth at the interface after processes at lower temperature also exceeds the AlGaN layer thickness, these craters are also considered as right, while the flat areas do not show the actual interface. They should show the oxide/AlGaN interface but instead they are assumed to reflect the AlGaN/GaN interface.

4.3 Analysis

As the entire thesis is based on results of various analysis devices, critical reflection and detailed discussion of the obtained data is inevitable. Especially the determination, interpretation and prevention of artifacts are found to play a key role for many investigations.

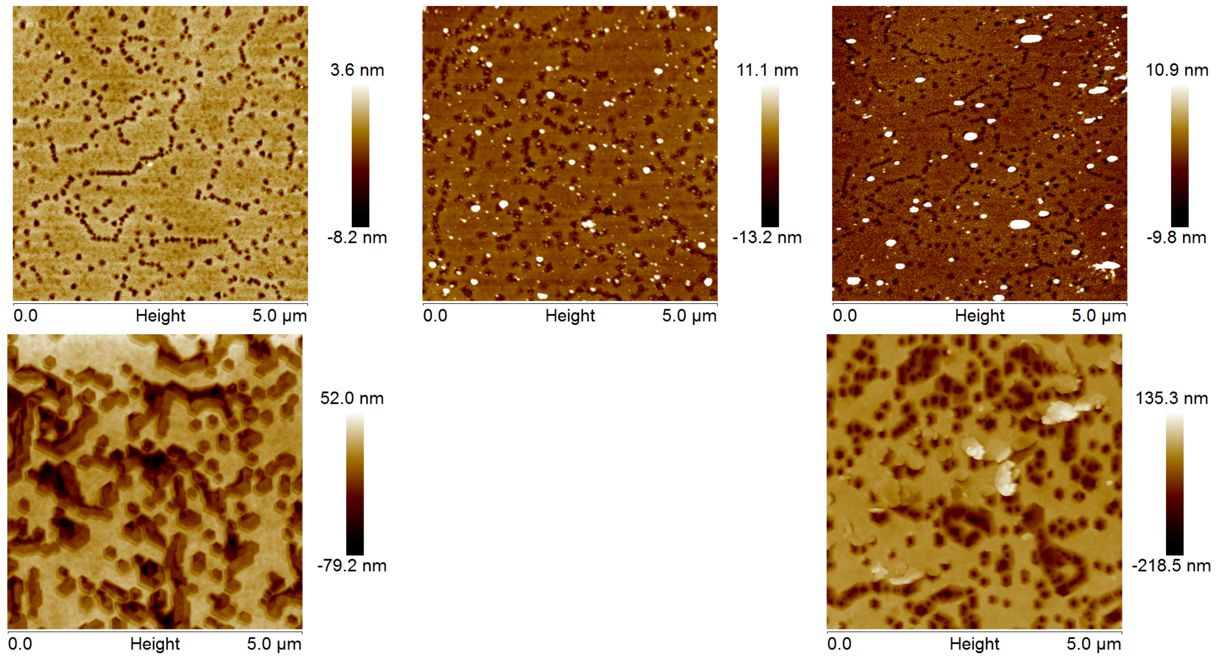

Figure 4.33: AFM analysis of the Ga_2O_3/GaN interface after oxidation at a) 900 °C for 10 min and b) 1000 °C and c) 1100 °C for 1min after subsequent oxide removal; top: etching artifacts occurring; bottom: no etching artifacts

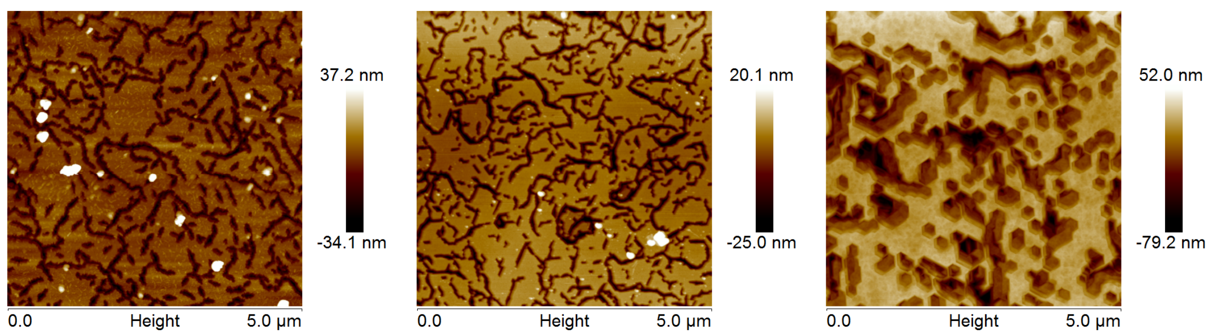

Figure 4.34: AFM analysis of the oxide/semiconductor interface after oxidation at a) 900 °C for 10 min and b) 1000 °C and c) 1100 °C for 1 min after subsequent oxide removal

4.3.1 AES Analyis

AES analysis is predestined for investigations on flat layers, consisting of well-known stable materials with similar IMFPs and sputter rates. As none of these properties applies for the observed samples, these aspects and the way how to handle them is discussed. To get the most out of this analysis method it is further shown how to gain information on chemical bonds as well as depth information by altering the angle of the sample.

a) Definition of Oxide Thickness:
For layered structures with flat interfaces between two materials and known sputter rates, AES depth profiles are suitable in order to obtain the layer thickness. The depth profile of such a structure is for instance formed by oxidation of Si as shown in fig. 4.35. The oxygen concentration decreases within a short sputter time from its maximum value down to zero, while the atomic Si concentration rises conversely from zero to 100%. For the sake of clarity fig. 4.35 contains only oxygen and atomic Si, while oxidic Si is not shown (see fig. 4.41). For these ideal conditions the FWHM represents the oxide thickness and multiplying this value with the sputter rate for SiO_2 delivers the oxide thickness.

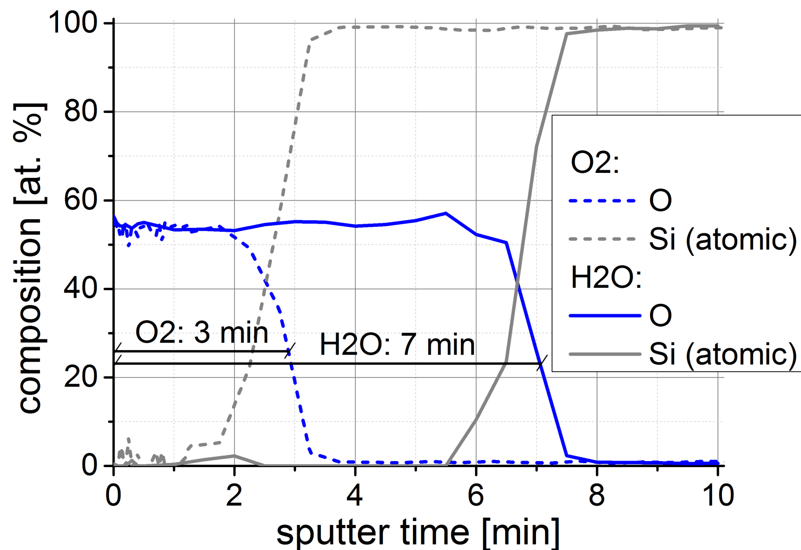

Figure 4.35: AES depth profile of a Si sample after oxidation in a dry (O2) and wet (H2O) oxidation process at 850 °C for 240 (O2) and 60 min (H2O)

However, the definition of layer thickness for GaN-based oxides is more complex. First of all, even if a three dimensional image would be available, it would not be possible to describe the thickness with a single value. There is the thickness of the uniform oxide layer but additionally there are the oxidic structures at the surface and interface, which often contain the majority of the oxide volume. Therefore it is considered as a reasonable compromise to use the FWHM as a value for the oxide thickness. However it has to be kept in mind that this value has no actual physical meaning and serves only for comparison of oxide thicknesses.

For thick oxide layers exceeding the information depth, the thickness of the uniform oxide layer can also be roughly approximated as the point, where N starts to be observed plus the

information depth for N. But as the thickness of many layers is below the information depth it is assumed reasonable to compare FWHM values.

Due to the presence of large interface craters, two materials with a large difference in their sputter rates (tab. 4) are sputtered simultaneously. The 30° angle between ion gun and surface worsens this issue. The semiconductor is sputtered approximately two times faster so that the semiconductor between oxidic structures is removed faster so that the remaining oxidic structures are not only sputtered from above but also from the side (sec. 4.3.1). Dependent on shape, size and location of oxide craters, this enhances the sputter rate. Combined with the uncertainty in sputter rate estimate, sputter rates cannot be directly converted into thicknesses. As a consequence and to prevent misinterpretation thicknesses obtained by AES are always given in the unit "mos".

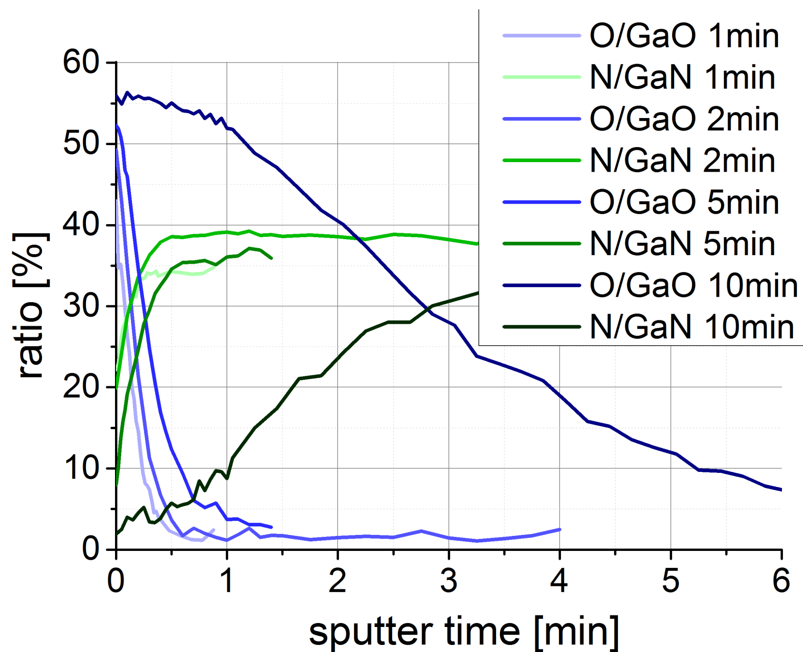

Figure 4.36: AES depth profiles of GaN samples after oxidation in RTA at 900 °C for various times

b) Calibration of material dependent parameters (sputter rates, information depths):

ESTIMATING SPUTTER RATES:

In order to convert sputter time into layer thickness, currently unknown sputter rates are estimated for GaN, AlGaN as well as their oxides. Sputter rates depend on a variety of experimental parameters such as the ion energy, the current density and the geometry of the setup and are therefore only valid within this thesis with the same parameters and setup. For exact determination, layers of known thickness are sputtered and the thickness divided by the sputter time delivers the sputter rate. As no GaN and AlGaN layers of known thickness are available and oxidic layers show severe roughness, only rough estimations can be made:

- The estimation of the sputter rate for GaN is probably the most challenging one because GaN is usually used as buffer which is too thick to be sputtered entirely. However, there are sandwich structures available that consist of an up to 6 nm thick GaN capping

layer on top of the AlGaN barrier. Sputter rates can be estimated by the emergence of the Al signal in depth profiles, but the large information depth of 3.2 nm for Al make estimations challenging. Measurements deliver a rate of approximately 16 nm/min but comparison to other sputter rates in tab. 4 suggests a lower rate of approximately 12 nm/min. However, within the scope of this thesis exact sputter rates are not critical, the relevant point is that the rate is significantly higher than for oxides.

- For the estimation of sputter rates for AlGaN the barrier layer with a thickness in the range of 30 nm, is investigated. The FWHM of 2.9 min delivers a sputter rate of approximately 10 nm/min. The sputter rate is supposed to depend on the Al concentration but as the Al concentration of the AlGaN barrier varies only in a small range, this influence can be ignored.

- For the estimation of Ga_2O_3 sputter rates only layers with severe roughness are available and solely one process (RTA, 1100 °C, 1 min) results in an oxide thickness, measurable by cross-sectional SEM or TEM (fig. 4.15). This layer has a uniform layer thickness of 100 nm and as the N signal rises in AES depth profiles after 17 min, a sputter rate of 6 nm/min is gained.

- Sputter rates for oxidized AlGaN are also estimated from samples oxidized at 1100 °C for 1 min in RTA. The oxide thickness, approximately 40 nm, is sufficient to be detectable in cross-sectional SEM. It has to be considered that not only the entire AlGaN layer is oxidized but also part of the underlying GaN. Analyzing the Al concentration within the oxide reveals that about 70% of the oxide layer is oxidized AlGaN while the rest is pure Ga_2O_3. Assuming an expansion during oxidation of 40% leads to a very rough estimation for the sputter rate of 5.5 nm/min. As the rate for Al_2O_3 is known to be 4 nm/min and Ga_2O_3 estimated to 6 nm/min, the oxidized AlGaN sputter rate of 5.5 nm/min seems reasonable.

Mat.	GaN	AlGaN	Ga_2O_3	$Al_{2x}Ga_{2(1-x)}O_3$	Al_2O_3	Si	SiO_2
[nm/min]	12*	10	6	5.5	4	8.5	8

Table 4: estimated sputter rates for the studied materials (green fields mark verified values) (* rough estimation based on comparison with rates of other materials)

Besides AES also XPS depth profiling is performed by sputtering and in analogy to AES, sputter rates for III-N-based materials are unknown. By comparison of rates for well-known materials such as SiO_2 the sputter rate in XPS is approximately an eight of the value for AES. As the O/GaO ratio in XPS drops to a certain concentration after 8 times longer sputter times (fig. 4.38), estimating all sputter rates an eight of the value for AES is assumed reasonable.

INFORMATION DEPTHS (AES AND XPS):

As theoretically explained in sec. 2.3.1, the information depth in AES and XPS equals about three times the IMFP, which depends on the electron energy and therefore on the element the electron is expelled from. Thus the information depth is strongly dependent on the element

as demonstrated in tab. 5 and fig. 4.37. While information depths for AES are independent on the excitation energy, they are linearly increasing with the excitation energy in XPS. XPS values are given for an excitation energy of 1.5 kV as used within this thesis.

While in standard AES analysis the electron detector is mounted perpendicular to the surface, it is tilted 45° in XPS leading to decreased information depth.

	kinetic energy AES [eV]	kinetic energy XPS [eV]	IMFP AES [Å]	IMFP XPS [Å]	IMFP XPS 45° [Å]
O	508	954	15	23	16
N	379	1089	12	26	19
Ga	1063	367	26	12	8
Al	1388	1410	32	32	23
C	275	1200	10	28	20

Table 5: kinetic energies of Auger- and photo-electrons (for 1.5 keV excitation energy) as well as the resulting IMFP* for relevant elements in GaN; in XPS the analyzing angle of 45° has to be considered; *information depths are higher by a factor of about 3

c) Artifacts (AES and XPS):

AES and XPS depth profiles of raw and processed III-N semiconductors are distorted by severe artifacts that affect the qualitative as well as the quantitative outcome. Based on the example in fig. 4.38, the origins and effects of these artifacts are discussed:

- A main source of artifacts is the great difference in “effective” sputter rates between Ga and N within the GaN crystal:
  - As N is not stable at the surface, GaN always finishes with a Ga adlayer, leading to decreased N/GaN ratios at the surface. As the bulk is measured by sputtering, former bulk layers become also surface layers by removing overlying layers. Therefore the measured values for N bulk concentrations are significantly reduced.
  - But N is not only not stable at the very surface, the ion bombardment generally favors sputtering of N over Ga due to the enhanced desorption of N.

  This behavior is confirmed by an observation made for the preparation of a 50 nm thin lamella, used for TEM analysis. These TEM lamellas are manufactured by a focused ion beam (FIB) that cuts out the lamella of a sample. Due to the usage of high energetic ions N is preferentially desorbed and the remaining Ga forms droplets, visible at the cross-section. It is seen that slower processing by lower energies results in less droplets. Since AES and XPS are performed with different excitation energies there might be a difference between both analysis techniques.

- Further artifacts, especially concerning the very surface, originate from the elemental- and technique-specific information length as shown in tab. 5/fig. 4.37. Due to air exposure every surface contains some organic contamination with a thickness up to

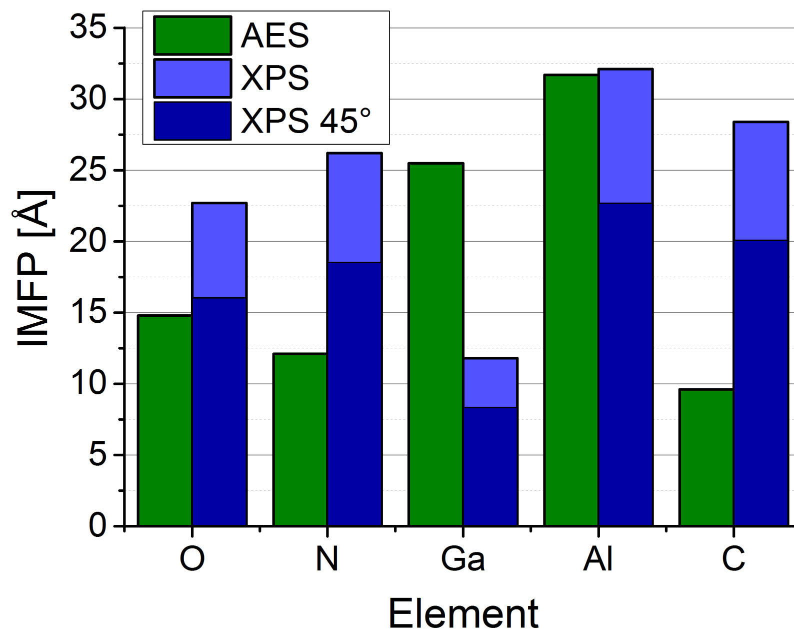

Figure 4.37: IMFP* for relevant elements for AES and XPS analysis; in XPS the analyzing angle of 45° has to be considered; *information depths are higher by a factor of about 3

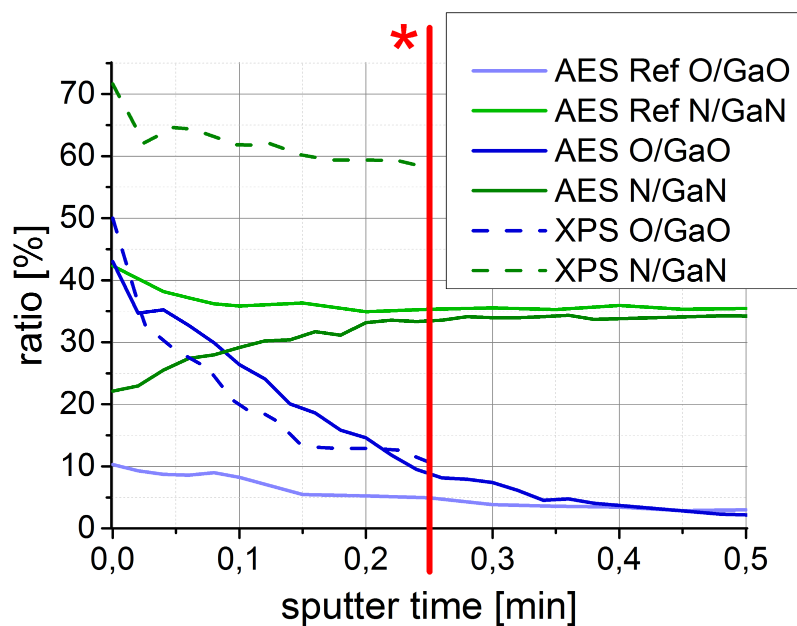

Figure 4.38: depth profiles of GaN samples oxidized in RTA at 900 °C for 1 min, obtained by AES (solid) and XPS (dashed) as well as of an untreated GaN reference; * XPS sputter times are adjusted to AES values

1 nm. For surface spectra only the material beyond this contamination layer contributes to the signal. If the information depths for all elements were equal, concentrations would decrease equally and no distortion would occur. But as information depths vary strongly, some element concentrations decrease more than others. For AES the information depth of N is approximately half the value of Ga resulting in reduced N/GaN ratios at the surface. For XPS on the other hand the information depth of Ga is less than half the value of N, heavily increasing the N/GaN ratio at the surface. Therefore in contrast to AES this artifact adds up to the one of the first point. The strong artifact influence is well demonstrated in fig. 4.38, where even the oxidized GaN sample with an additional superficial Ga_2O_3-layer the surface shows enhanced N/GaN concentration compared to the bulk.

This phenomenon is not limited to N/GaN ration but concerns also O/GaO ratios but as their difference in information length is smaller, it is not that distinctive, but still observable.

- While previous artifacts are hard to prevent, the following one can be prevented easily. For XPS analysis an excitation energy of 1.5 kV is used resulting in overlapping $N1s$ photoectron- and Ga $LMM1$ Auger-peaks. Due to the complexity of Auger peaks, originating from the involvement of three electrons in the Auger process, this peak cannot be subtracted adequately. Therefore the N/GaN concentration is enhanced during the entire depth profile.

  This artifact can be easily avoided by using a different X-ray source, resulting in a different excitation energy. As AES peaks do not shift and XPS peaks do shift with varying excitation energy, overlapping can be prevented.

  Due to the excitation by electrons instead of photons, this artifact cannot occur in AES. In AES Auger peaks can overlap but this is not observed for elements relevant in this thesis.

- A further artifact originates from the way of measuring and assessment. For sputtering the sample is bombarded with positive ions, causing charging of the sample. Although the samples are grounded, charge emerges on the surface due to the bad conductivity of the oxide. This charge vanishes after a short time, especially under electron bombardment. For AES depth profiles for every element a 30 eV range around the peak is measured ten times, averaged to one peak curve and followed by the measurement of the next element. After observing all elements the surface is sputtered and the next measurement cycle starts. The artifact occurs due to averaging of ten peaks. For charged samples the peak shifts to higher or lower energies and if charging dissipates within the ten averaged samples, the average peak is significantly lower than for peaks without shift. To prevent this artifact, a specific amount of time is waited after every sputter cycle before measuring in order to ensure that the sample is not charged. However, artifacts cannot be fully ruled out, especially as the electron bombardment for measuring also introduces charges and this cannot be prevented.

- Not only ion sputtering but also to a minor extent electron bombardment causes desorption of surface atoms. For most materials this is negligible but some, such as fluorine and possibly N and O show significant reduction in their concentration. To avoid this effect, easily desorbing elements are measured before stable ones.

- The large difference in sputter rate between III-N materials and their oxides (tab. 4) combined with the high roughness of oxide/semiconductor interfaces leads to the distortion of AES depth profiles. In extreme cases this can cause obscure depth profiles as shown in fig. 4.39, where the O/AlGaO ratio is increasing at greater depths:

  In the beginning of sputtering the uniform oxide layer is entirely sputtered and as a consequence besides the remaining oxide in interface craters the semiconductor below is removed, but with a higher sputter rate. Since sputtering is performed under an angle of 30° between ion gun and surface, oxide structures get increasingly uncovered, resulting in enhanced O signal. Therefore the oxygen concentration in this region is increased but simultaneously the gained oxide depth is decreased due to the enhanced area of sputtering.

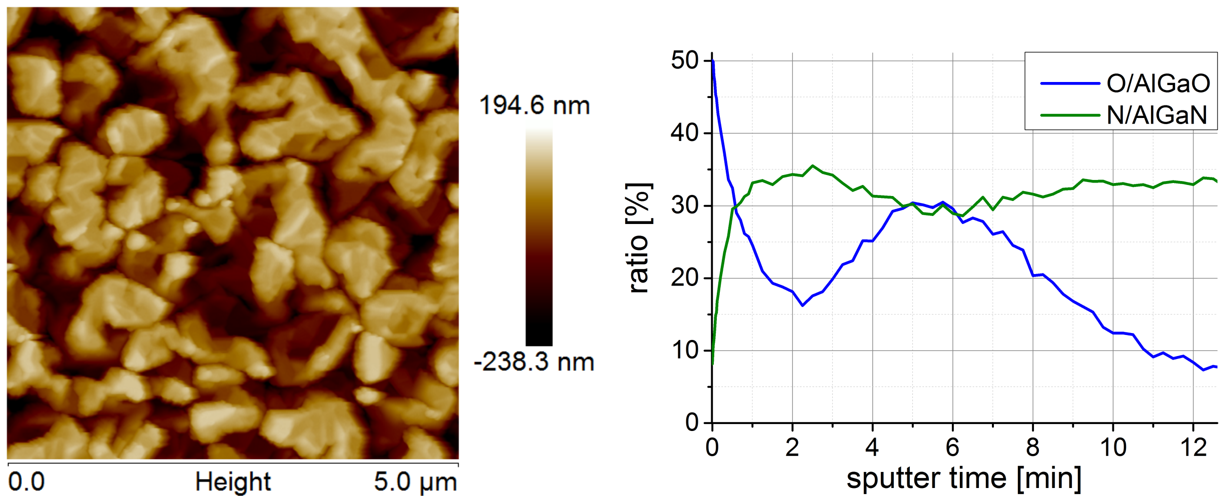

Figure 4.39: AlGaN sample oxidized in a wet oxidation process at 850 °C for 60 min: a) AFM analysis of the oxide/AlGaN interface and b) AES depth profile

- While Ga and Al are bound to N within the semiconductor, they are bound to O in the oxide. Both structures have different relative sensitivity factor and therefore the Ga and Al concentrations within the oxide are altered. Ga is calibrated for GaN but as Al is calibrated for its elementary form, even the RSF for Al in AlGaN is slightly wrong.

  A further artifact emerges for the simultaneous presence of elements in its nitride as well as its oxidic form as for both forms the peak is shifted as shown in fig. 4.40. The resulting peak height and thus the revealed concentration are therefore decreased. While in Si as well as in Al there is a noteworthy shift, this aspect has only neegligible influence on Ga.

d) Chemical Bonds:

Although XPS is predestined for gaining information on chemical bonds, AES analysis also allows some conclusions. Depending on the participating elements bonds can cause a shift in the electron energy obtained in AES. In AES spectra peaks shift and also the peak form changes and has to be compensated by an adaption of the RSF.

For Ga the change of the peak form from its nitride to its oxide form is negligible and cannot be recognized in the spectra. Si and Al on the other hand exhibit a large peak shift of 10 and 8 eV for the transition from their elemental to their oxidic form as depicted in fig. 4.40. The assessment of elements with large shifts affords treatment of both forms as different elements as the sum of two shifted peaks results in lower peak heights than the sum of the two peak heights. Furthermore the elemental and oxidic form have slightly different RSF. Especially in the transition region, where both forms are present this has to be considered in order to prevent artifacts as shown in fig. 4.41. fig. 4.41a reveals the decreased concentration in the transition region for oxidized Si. Al shows a comparable peak shift between its atomic and oxidic form, but as for the oxidation of AlGaN the shift is only 2.5 eV, treatment as two separated elements is not possible.

However, the shift is large enough to be obtained, which enables the determination if Al is in its nitride or oxide form.

It has to be considered that a peak shift does not compulsory originate from a change in bond but can also be caused by charging. However, if charging is the source of the shift all observed elements shift in a comparable amount.

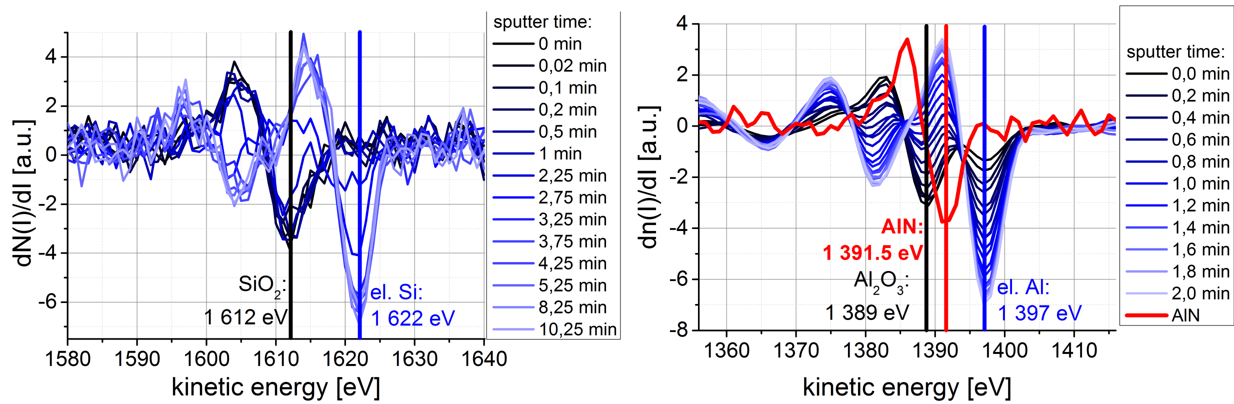

Figure 4.40: change of the a) Si- and b) Al-peak form in AES and shift to lower energies due to oxidation; in b) there is further the nitride form shown

e) Depth Information by Angle Resolved Surface Spectra:

As described by eq. 2.10 the information depth depends on the analyzing angle, which enables one to gain depth information by angle resolved measurements.

The information depth decreases with the sine of the analyzing angle with respect to the surface plane. Thus, for thin layers with thicknesses below the information depth, the analyzing angle can be reduced down to a point where no N signal is remaining. The sine of this angle multiplied by the information depth for N delivers an approximation for the uniform oxide layer thickness.

Due to the geometrical setup the minimum angle is 40° so that the information depth can only be decreased to 64% of its initial value. To enhance the range of observable thicknesses, a special wedge-shaped sample holder (fig. 3.2) with an incident angle of 30° can be used, enabling a minimum angle of 10° and a reduction in information depth down to 17%.

Fig. 4.43 shows the N/GaN ratio as a function of the analyzing angle and the information depths for a GaN sample oxidized at 800 °C for 10 min. Although there are many outliers,

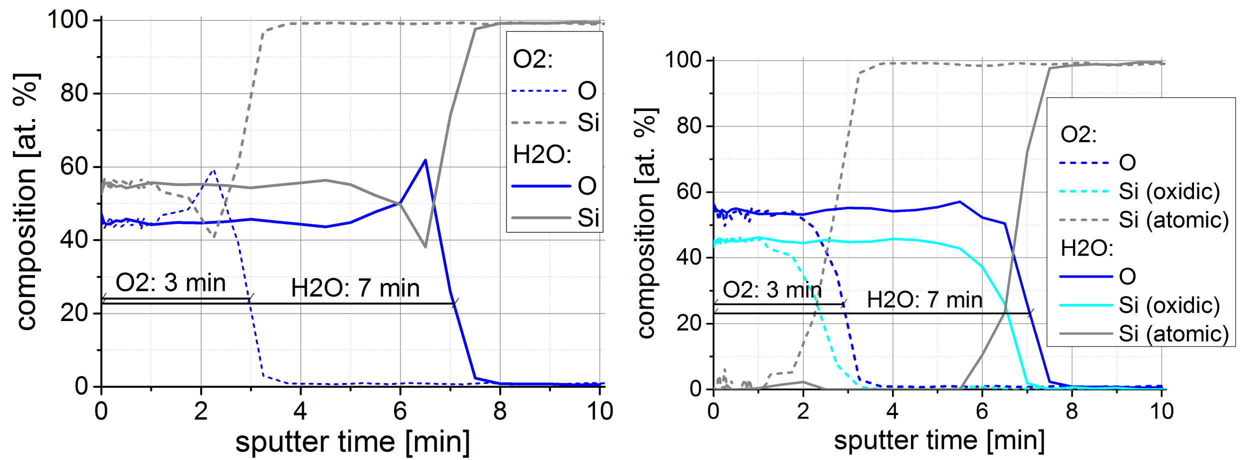

Figure 4.41: depth profiles for Si samples oxidized at 850 °C for 60 min wet (H2O) and for 240 min dry (O2) in a horizontal oven, whereby oxidic and atomic Si are a) not separated and b) strictly separated

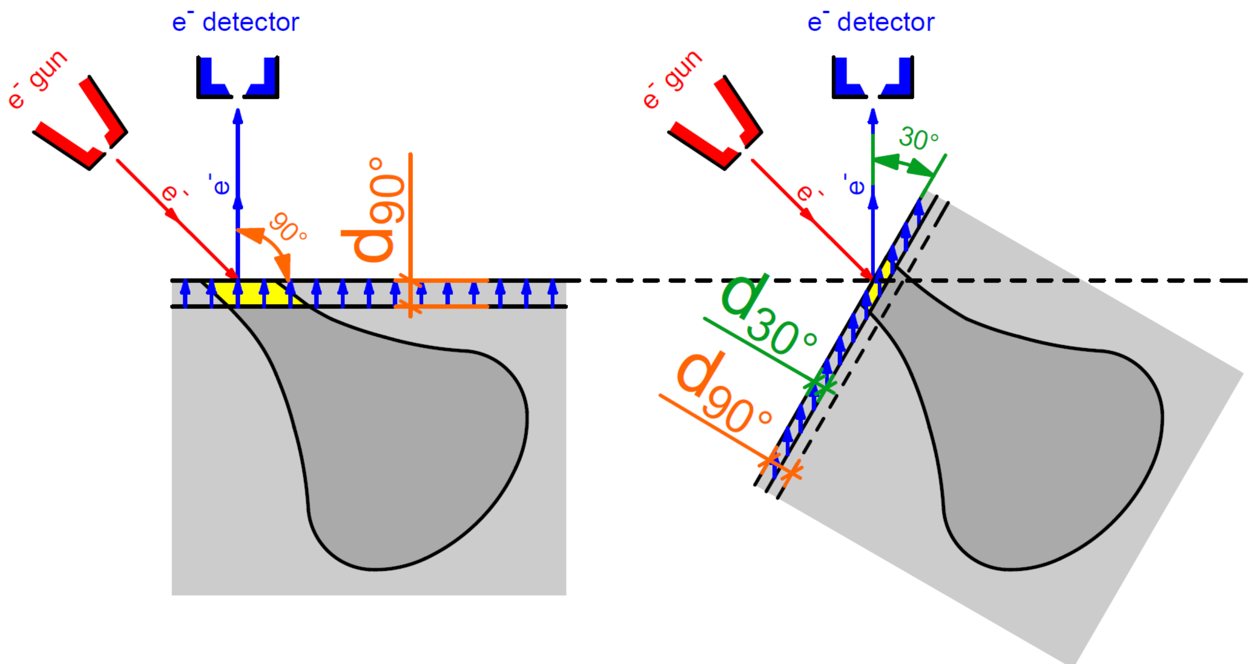

Figure 4.42: demonstration of the dependence of the information depth on the analyzing angle in AES; dark grey: activation volume, yellow: information volume for AES

a clear trend is observable. It is clearly seen that the O/GaO concentration rises as the N/GaN ratio drops with decreasing analyzing angle. However, for angles below 25° the absolute signal decreases to an amount where the peak cannot be distinguished from noise anymore. Therefore it can be estimated that the uniform oxide layer is thinner than 3 Å , which suggests that if there is a uniform oxide layer present, it can only consist of one or two monolayers O. Since there is a great amount of O observed at the surface, it can be assumed to exist concentrated at defect sites such as dislocations. The measured thickness also includes superficial contamination so that the O containing layer has to be even thinner.

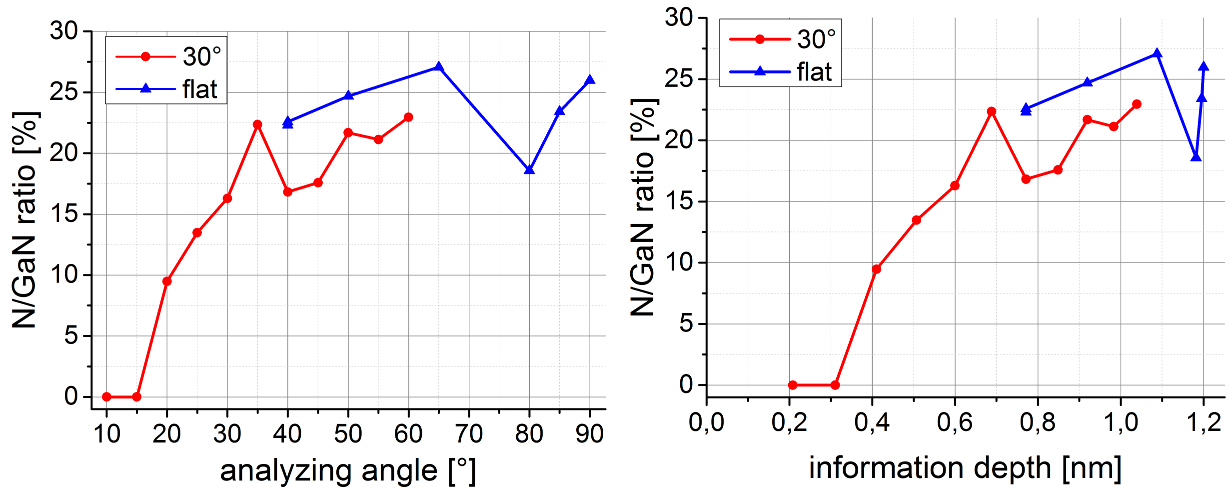

Figure 4.43: N/GaN ratio at the surface of a GaN sample after oxidation at 800 °C for 10 min in RTA as a function of a) the analyzing angle and b) the information depth for a flat and a wedge-shaped (30°) sample holder for an

4.3.2 EDX Analysis

EDX analysis can be performed within the SEM- as well as the TEM-setup, whereby in the SEM the electron gun ascribes an angle of 45° with the surface-plane and uses an initial electron energy of 5 keV instead of 20 keV as used in the TEM.

The information depth can be approximated by the Andersen-Hasler equation [LMX+06]:

$$R_z = 0.06\ E_0^{1.68} \frac{1}{\rho_0} \tag{4.3}$$

R_z ist the information depth (in μm), E_0 the initial electron energy (in keV) and ρ_0 the density (in g/cm^{-3}). For exact calculation the critical excitation energy for the characteristic X-ray line has to be subtracted from E_0 [New02], but within this thesis the Andersen-Hasler approximation is sufficient.

The resulting information depths for emerging materials are shown in tab. 6, whereby also the electron gun angle of 45° in SEM is considered. However, as TEM samples are only 50 nm thick, the calculated information depth of TEM has no practical relevance.

SEM-EDX analysis shows constantly reduced Ga concentrations. Due to the wurtzite crystal structure the bulk N/GaN ratio has to be quite exactly 50% and the form of the excitation volume ensures that the surface region with a lower N content has only negligible

information depth [nm]	GaN	Ga_2O_3	AlN	Al_2O_3
SEM (5 kV)	101	105	154	190
SEM 45° (5 kV)	71	74	109	134
TEM (20 keV)	468	489	715	882

Table 6: information depth of EDX for emerging materials (calculation by the Andersen-Hasler approximation (eq. 4.3) for different primary electron energies and electron gun angles used in SEM and TEM

influence. Ga_2O_3 is seen to be stoichiometric and has therefore a Ga-concentration of 40%. TEM-EDX as well as electron energy loss spectroscopy (EELS) confirms this values [Rei15], but SEM-EDX reveals a N/GaN ratio of 40±3% in GaN as well as a Ga/GaO ratio of 50±4% in Ga_2O_3. Both values can be perfectly corrected by dividing the Ga concentration by a correction factor of 1.5. An explanation for this discrepancy is currently missing.

4.3.3 AFM

Although AFM is very resistant against artifacts, due to the hardness of GaN tip artifacts are often occurring. The most common observed artifact is the so called double tip artifact which occurs after breaking of the tip, leaving a structure with two tips or more irregular forms. These artifacts are easy to obtain as seen in fig. 4.44, where the same shape is frequently appearing over the entire surface. Changing the cantilever solves this problem.

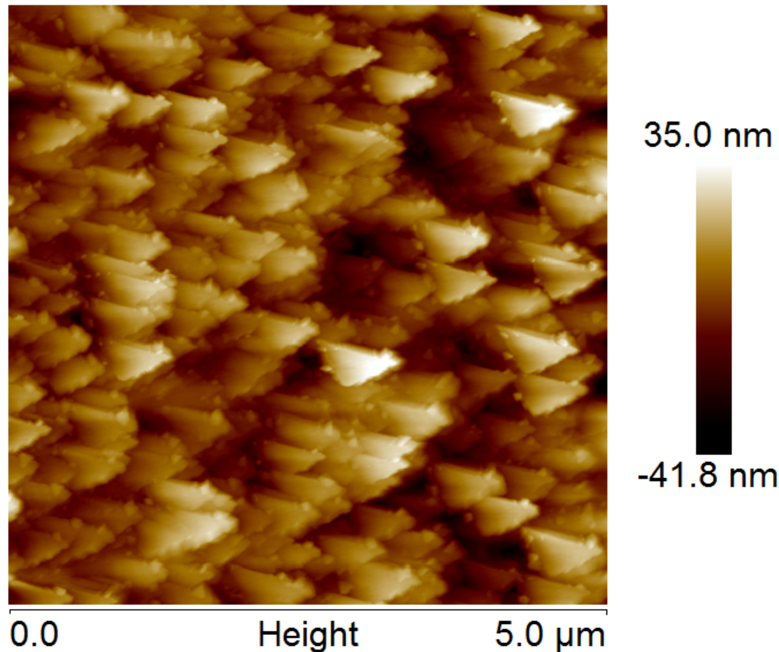

Figure 4.44: double tip artifact in AFM for a wet oxidized GaN sample at 850 °C for 240 min

4.3.4 Layer Thickness Measurements

Performed Layer Thickness Measurements:
Within this thesis many different methods are used to obtain oxide layer thicknesses in different regimes:

For the thinnest layers with thicknesses below the information depth for N of 1.2 nm, approximations are based on N concentrations in AES spectra. To enhance the accuracy and to expand measurements to thinner layers, angle resolved AES can be performed.

For thicknesses between 1.2 and about 10 nm, AES (and XPS) depth profiles are the only reasonable available option with great uncertainties due to unknown sputter rates and the complex interpretation of depth profiles due to the surface and interface structures.

Beginning with approximately 10 nm, cross-sectional SEM and TEM analysis can be performed, delivering reliable information on the continuous oxide layer as well as sizes of hillock and crater structures, which are additionally available for all GaN samples by AFM analysis.

Improved Layer Thickness Measurements:
While oxide hillocks at the surface as well as craters at the oxide/semiconductor interface can be measured accurately, for uniform oxide layers with thicknesses below 10 nm only rough estimations are available. For the objectives pursued in this thesis these estimations are sufficient but for further investigations more accurate thicknesses might be desired. Therefore the following method, similar to the one used by Zhou et al. [ZAIS+08] and shown in fig. 4.45, is recommended:

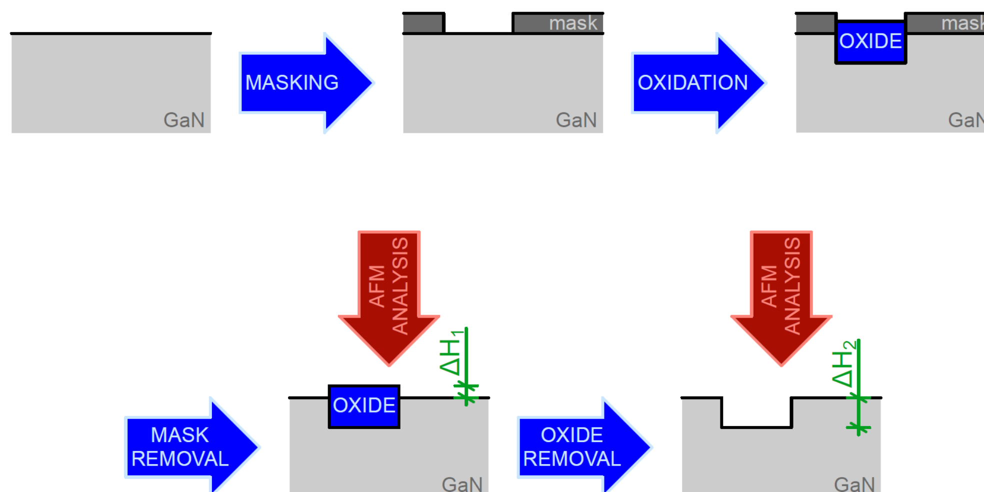

Figure 4.45: measurement tehcnique in order to obtain exact oxide thicknesses as well as the volume expansion due to oxidation of III-N materials

1. Raw wafers are partly covered by a superficial mask and subsequently cleaved.
2. The masked fragments are oxidized in an RTA process, whereby the mask prevents the underlying semiconductor to be oxidized and oxides are only growing at unmasked areas.

3. The mask is removed by etching and the height difference ΔH_1 obtained by AFM.
4. In a last step the oxide is removed and the height difference ΔH_2 measured by AFM. The sum of ΔH_1 and ΔH_2 delivers the oxide thickness and furthermore the volume expansion due to oxidation.

5 Conclusion

The high roughness of surfaces and interfaces of directly oxidized III-N layers is considered as a crucial aspect for the suitability as gate dielectric. In order to obtain the underlying reason for the roughness, this thesis covers the investigation of early stages of oxide growth.

Thermal oxidation is found to start at a thermal threshold of approximately 800 °C and the temperature dependence obeys an Arrhenius-law. Regardless of the processing parameters, oxidized GaN is obtained as stoichiometric and present in the form of crystalline Ga_2O_3. Besides a uniform oxide layer, large hillocks at the surface as well as craters at the oxide/semiconductor interface emerge. Oxidation is observed to be enhanced and start at threading dislocation sites, causing craters in the interface. Surface hillocks rise above these sites due to the volume expansion of 40% during oxidation [CZX+00]. Especially in early growth stages these structures are greater in size than the uniform layer and lead to tremendous roughness at surface and oxide/semiconductor interface.

Associated annealing studies in NH_3 show that decomposition also starts at dislocations and forms craters in the same shape as oxidation. Besides the standard oxidation reaction at defect-free areas, this suggests a decomposition a decomposition enhanced oxidation mechanism at dislocation sites. Instead of the direct conversion of GaN into Ga_2O_3, GaN first decomposes to Ga and N and after immediate desorption of N, the remaining Ga is oxidized with an increased rate.

Besides the horizontal planes enhanced oxidation at dislocation sites also causes vertical planes to be exposed to the environment and therefore additional oxidation in horizontal direction. Especially for early stages the oxide volume increases rapidly and results in a progressively increasing oxidation rate with ongoing oxidation. This behavior saturates as emerging craters coalesce and the oxidation rate becomes constant [ZAIS+08] [CZX+00] (fig. 2.5). With further ongoing oxidation time, the reaction is not limited by the oxidation reaction anymore but by the diffusion of N and/or O, resulting in a slower but still constant rate [ZAIS+08] [CZX+00]. Another factor enhancing the progressive behavior in early growth stages is the exothermicity of the oxidation reaction, especially at threading dislocations, that introduces a local temperature rise and therefore enhanced oxidation. It also has to be considered that in the very beginning of oxygen exposure the Ga adlayer, which always exists on top, is rapidly covered by adsorbing oxygen, even at temperatures below the temperature threshold. The sum of these aspects results in the complex oxidation rate as a function of the processing duration (fig. 4.12).

The limited diffusion rate of N is further assumed to be the origin for the occurrence of large voids within the oxide, which are obtained solely in regions exceeding a specific depth. As oxidation, especially at threading dislocations, proceeds faster than the emerging N can diffuse and desorb, N forms voids within the oxide. AlGaN layers have a higher temperature threshold and lower oxidation rate than GaN layers. While in GaN surface hillocks and hexagonally shaped interface craters emerge at dislocation sites, in AlGaN surface hillocks

additionally rise from defect-free areas and interface craters are oblong crater lines, originating from dislocations.

The main analysis method within this thesis is AES, which is designated for investigations on flat layers, consisting of well-known stable materials with similar IMFPs and sputter rates. However, investigated layers do not fulfil any of these requirements. Sputter rates (tab. 4) and information depths (tab. 5) are estimated for AES as well as XPS. Great differences between the effective sputter rates for GaN and its oxide Ga_2O_3 as well between Ga and N within the GaN crystal are revealed to cause severe artifacts in AES depth profiles. As the information depth equals the material-dependent IMFP, N and Ga show different values. This leads to further artifacts as well as charging of the surface due to sputtering and electron bombardment.

5.1 Outlook

The main advantage of using directly oxidized layers instead of deposited layers as gate dielectrics is the reduced amount of interface states, which cause dynamic effects such as threshold voltage drifts [Lag14].

However due to the observed interface roughness and the occurring voids it is doubtful, if these oxide layers are suitable as gate dielectrics. With optimized processing parameters the quality of thermal oxides can be increased and the emergence of voids can possibly be inhibited, especially as they are only observed for large thicknesses. But as the fabrication of dislocation-free layers is technically not feasible, dislocation enhanced oxidation will always cause high roughness. A potential solution might be the use of alternative oxidation methods such as plasma oxidation, which are performed at lower temperatures. Furthermore the combination of a directly oxidized layer and an additional deposited layer could have benefits.

In order to investigate the electrical behavior, especially regarding the threshold voltage drift, there is an ongoing project work [Kol15] that covers these issues for the obtained oxide layers. Thermal oxides are compared with deposited Si_3N_4 as well as with a combination of both layers.

Acronyms

Acronym	Meaning
2DEG	two-dimensoinal electron gas
AES	Auger electron spectroscopy
AFM	atomic force microscopy
Al	aluminium
Al_2O_3	aluminium oxide
ALD	atomic layer deposition
AlGaN	aluminium gallium nitride
AlN	aluminium nitride
Ar	argon
CBM	conduction band minimum
CVD	chemical vapor deposition
EDX	electron dispersive X-ray spectroscopy
EELS	electron energy loss spectroscopy
EFTEM	energy filtered transmission elecctron microscopy
fcc	face-centered cubic
FIB	focussed ion beam
FOM	figure of merit
FWHM	full width half maximum
Ga	gallium
Ga_2O_3	gallium oxide
GaAs	gallium arsenide
GaN	gallium nitride
GTO-thyristor	gate turn-off thyristor
H_2	dihydrogen
H_2O	water
H_2O_2	hydrogen peroxide
H_3PO_4	phosphoric acid
HCl	hydrogen chloride
hcp	hexagonal close packed
HEMT	high electron mobility transistor
HF	high frequency
HfO_2	hafnium oxide
IGBT	insulated gate bipolar transistor
IMFP	inelastic mean free path
InN	indium nitride

Acronym	Meaning
KOH	potassium hydroxide
La_2O_3	lanthanum oxide
LED	light emitting diode
MBE	molecular beam epitaxy
MFP	mean free path
mis	minutes of sputtering as a unit for thicknesses
MIS-HEMT	metal-oxide semiconductor high electron mobility transistor
MOCVD	metalorganic vapor phase epitaxy
MOSFET	metal-oxide semiconductor field effect transistor
N	nitrogen
N_2O	nitrous oxide
NH_3	ammonia
O	oxygen
PVD	physical vapor deposition
RMS	root mean square
RSF	relative sensistivity factor
RTA	rapid thermal annealing
SAED	selected area electron diffraction
SBH	surface barrier height
SEM	scanning electron microscopy
Si	silicon
Si_3N_4	silicon nitride
SiC	silicon carbide
SiO_2	silicon dioxide
SK	Stranski-Krastanov
TEGa	Triethylgallium
TEM	transmission electron microscopy
TMGa	Trimethylgallium
UHV	ultra-high vacuum
VBM	valence band maximum
XPS	x-ray photoelectron spectroscopy
XRD	x-ray diffraction

Symbols

Symbol	Unit	Meaning
α	[°]	angle
d	[m]	thickness
$\Delta H^{\ominus}$	[kJ/mol]	reaction enthalpy
E_A	[kJ/mol], [eV]	activation energy
E_F	[eV]	Fermi-level
E_{kin}	[eV]	kinetic energy
k	[m^2 kg s^{-2} K^{-1}]	Boltzmann constant
λ	[nm]	IMFP
n	[ ]	reaction orderr
q	[C]	elementary charge
r	[mol L^{-1} s^{-1}]	reaction rate
$R_{DS,on}$	[Ω]	specific on-resistance
R_z	[μm]	information depth in EDX
t	[s]	time
T	[K]	temperature
t_p	[s]	processing time
T_p	[K]	processing temperature
V_{br}	[V]	breakdown voltage

List of Figures

1.1 III-N wurtzite crystal structure [Wik14] (grey spheres: Ga^{3+}; yellow spheres: N^{3-}) . . . 2
1.2 demonstration of the origins and effects of spontaneous and piezoelectric polarization in an exemplary III-N stack [Hen14] . . . 3
1.3 Ga ([0001]) and N phase ([000$\bar{1}$]) GaN wurtzite crystal structures [Ost07] . . . 3
1.4 schematic band diagram of an idealistic AlGaN layer on top of GaN: formation of an electric dipole for layer thicknesses exceeding critical values [WJ07] [Lag14] 4
1.5 schematic band diagram for different surface donor states distributions: high density of states in a narrow energy range (left) vs. low density of states in a broad energy range (right) [GMC+10] . . . 5
1.6 comparison of material properties between wide band gap materials such as SiC and GaN with traditional semiconductors such as Si and GaAs (* values within the 2DEG) [Oku06] . . . 6
1.7 comparison of various FOMs of wide band gap materials such as SiC and GaN with traditional semiconductors such as Si and GaAs (FOMs are normalized to values for Si) [Oku06] . . . 6
1.8 demonstration of the superiority of GaN over other semiconductors for high power, high frequency applications due to a) the better R_{sp}/V_{BD}-characteristic (R_{sp}... specific on-resistance R_{DSon}) [HPE10] and b) the combination of high RF output power and frequency [Hon14] . . . 7
1.9 potential application fields for GaN devices in power electronics [Hon14] . . . 8
1.10 schematic structure of an AlGaN/GaN-MIS-HEMT . . . 8
2.1 schematic MBE-system [Wik14] . . . 13
2.2 scheme of the occuring processes during MOCVD [Bar14] . . . 14
2.3 unit cell of monoclinic β-Ga_2O_3: dark spheres represent Ga^{3+} and brighter ones O^{2-} ions [JW13] . . . 15
2.4 Ga_2O_3 unit cell showing that a) Ga^{3+} ions exist in tetrahedral and octahedral coordination [ASA96] and b) O^{2-} ions form a distorted fcc crystal structure (green) [KM03] . . . 16
2.5 intensity of the β-Ga_2O_3 peak in X-ray diffraction (XRD) analysis, which is proportional to the oxide layer thickness, as a function of the oxidation time for various temperatures (diamond: 800 °C; square: 900 °C; circle: 1000 °C; triangle: 1050 °C); the knee for temperatures greater than 900 °C indicates a change of the oxidation limiting process) [CZX+00] . . . 17
2.6 demonstration of the Auger effect a) in an atomistic model and b) in an energy band diagram [Wik14] . . . 23
2.7 activation volume due to electron bombardment [Phi14] . . . 24
2.8 inelastic mean free path as a function of the electron energy [Nix14] . . . 24
2.9 oxidation of an AlGaN sample at 900 °C 10 min (RTA): a) raw (blue) and differentiated (red) AES spectrum and b) the gained surface composition . . . 25
3.1 schematic view of the experimental AES setup showing the geometrical arrangement of the components . . . 29
3.2 AES setup with different sample holders showing the achievable angles between electron gun, sample and electron detector for the initial position and the maximum tilted sample . . . 30

4.1 simplified procedure for the investigation of the oxidation process 31
4.2 AFM analysis of the as-grown a) GaN and b) AlGaN surface 31
4.3 AES depths profiles of raw reference samples: a) GaN and b) AlGaN 32
4.4 temperature profile during processing (T_p. . . processing temperature, t_p. . . processing time) 33
4.5 AFM analysis of the GaN surface after oxidation at 900 °C for 1 min: rise of hillocks at threading dislocation sites 34
4.6 AFM analysis of the GaN surface after oxidation at 900 °C for a) 2 min, b) 5 min and c) 10 min, revealing d) the linear hillock height growth with ongoing oxidation time 34
4.7 AFM and SEM analysis of the GaN surface after oxidation for 1 min at a) 1000 °C and b+c) 1100 °C; d) Arrhenius-plot of the hillock heights 35
4.8 O^{2-}-ions arrange within the monoclinic β-Ga_2O_3 crystal structure in a slightly distorted fcc structure [KM03], enabling the formation of crystalline protrusions with equilateral triangular base on (111)-planes 35
4.9 AFM analysis of the Ga_2O_3/GaN interface after oxidation at a) 900 °C for 10 min and b) 1100 °C for 1 min and subsequent oxide removal; protrusions in b) are related to contamination due to HCl etching 36
4.10 AFM analysis of surfaces after defect etching in a) H_3PO_4 [RRB+15] and b) KOH 36
4.11 demonstration of $\{11\bar{2}x\}$ and $\{10\bar{1}x\}$ planes in GaN crystals suggest greater stability of $\{11\bar{2}x\}$ over $\{10\bar{1}x\}$ planes 37
4.12 a) surface O and N concentration and b) oxidation rate* of GaN samples for oxidation at 900 °C as a function of the oxidation time; *oxidation rates based on FWHM in AES depth profiles; green lines are schematic (no quantitative values) and based on [ZAIS+08] [CZX+00] 38
4.13 schematic oxide layers in different phases of oxide growth (fig. 4.12b) for the proposed oxide growth model 39
4.14 Arrhenius plot: oxidation rate (FWHM in AES depth profiles) as a function of the oxidation temperature (for various durations); "H2O" and "O2" are referred to wet and dry oxidation in the horizontal oven; *calculation of activation energy based on these data giving a value of 3.7 eV, as represented by the red line 41
4.15 cross-sectional a) SEM and b) dark-field TEM analysis [RKP+15] of a GaN sample oxidized at 1100 °C for 1 min 42
4.16 SEM and EDX analysis of the GaN surface after oxidation at 900 °C for 10 min 42
4.17 Al/(Ga+Al) ratio for AlGaN samples oxidized at different temperatures for various times 42
4.18 AFM analysis of the AlGaN surface after oxidation at 900 °C for a) 1 min and c) 10 min 44
4.19 AFM analysis of the AlGaN surface after oxidation for 1 min at a) 1000 °C and b) 1100 °C 44
4.20 AFM analysis of the oxide/semiconductor interface after oxidation at 1100 °C for 1 min and oxide removal 45
4.21 cross-sectional SEM analysis of an AlGaN sample after oxidation at 1100 °C for 1 min 46

4.22 a) AFM and b) SEM analysis of the GaN surface after oxidation in horizontal oven at 850 °C for 240 min . . . 47
4.23 a) AFM analysis of the Ga_2O_3/GaN interface after oxide removal and b) cross-sectional SEM analysis after oxidation in horizontal oven at 850 °C for 240 min . . . 47
4.24 AlGaN sample after oxidation in horizontal oven at 850 °C for 240 min: a) AFM analysis and b) AES depth profile . . . 48
4.25 a+b) AFM and c) SEM analysis of the surface of GaN samples oxidized in a wet oxidation process at 850 °C for 60 min . . . 49
4.26 GaN sample oxidized in a wet oxidation process at 850 °C for 60 min: a) AFM analysis of the oxide/GaN interface and b) AES depth analysis . . . 49
4.27 AFM analysis of the surface of an AlGaN sample oxidized in a wet oxidation process at 850 °C for 60 min . . . 50
4.28 oxidation of GaN and AlGaN in N_2O at 750 and 800 °C for 30 min: a) AFM analysis and b) AES depth profiless . . . 51
4.29 GaN and AlGaN samples oxidized in plasma oven for various oxidation times: a) AES depth profiles and b) surface analysis . . . 52
4.30 optical analysis of GaN surfaces after annealing in N_2 at 1100 °C for 1 min reveals severe decomposition and due to enhanced desorption of N over Ga remaining liquid Ga droplets, whose sizes decrease near the sample's edge (inner/intermediate/outer zone from left to right); top/bottom: before/after droplet removal . . . 54
4.31 GaN surface after annealing in N_2 at 1100 °C for 1 min: top: SEM and EDX analysis of the inner (a+b) and outer zone; bottom: AFM analysis after liquid droplet removal . . . 55
4.32 AFM analysis of a) an untreated AlGaN reference sample and b) annealed in NH_3 at 700 °C at 235 mTorr for 30 min . . . 55
4.33 AFM analysis of the Ga_2O_3/GaN interface after oxidation at a) 900 °C for 10 min and b) 1000 °C and c) 1100 °C for 1min after subsequent oxide removal; top: etching artifacts occurring; bottom: no etching artifacts . . . 57
4.34 AFM analysis of the oxide/semiconductor interface after oxidation at a) 900 °C for 10 min and b) 1000 °C and c) 1100 °C for 1 min after subsequent oxide removal . . . 57
4.35 AES depth profile of a Si sample after oxidation in a dry (O2) and wet (H2O) oxidation process at 850 °C for 240 (O2) and 60 min (H2O) . . . 58
4.36 AES depth profiles of GaN samples after oxidation in RTA at 900 °C for various times . . . 59
4.37 IMFP* for relevant elements for AES and XPS analysis; in XPS the analyzing angle of 45° has to be considered; *information depths are higher by a factor of about 3 . . . 62
4.38 depth profiles of GaN samples oxidized in RTA at 900 °C for 1 min, obtained by AES (solid) and XPS (dashed) as well as of an untreated GaN reference; * XPS sputter times are adjusted to AES values . . . 62
4.39 AlGaN sample oxidized in a wet oxidation process at 850 °C for 60 min: a) AFM analysis of the oxide/AlGaN interface and b) AES depth profile . . . 64
4.40 change of the a) Si- and b) Al-peak form in AES and shift to lower energies due to oxidation; in b) there is further the nitride form shown . . . 65

4.41 depth profiles for Si samples oxidized at 850 °C for 60 min wet (H2O) and for 240 min dry (O2) in a horizontal oven, whereby oxidic and atomic Si are a) not separated and b) strictly separated 66
4.42 demonstration of the dependence of the information depth on the analyzing angle in AES; dark grey: activation volume, yellow: information volume for AES 66
4.43 N/GaN ratio at the surface of a GaN sample after oxidation at 800 °C for 10 min in RTA as a function of a) the analyzing angle and b) the information depth for a flat and a wedge-shaped (30°) sample holder for an 67
4.44 double tip artifact in AFM for a wet oxidized GaN sample at 850 °C for 240 min 68
4.45 measurement tehcnique in order to obtain exact oxide thicknesses as well as the volume expansion due to oxidation of III-N materials 69

List of Tables

1 comparison of relevant substrate properties [Vis11] 12

2 processing parameters for plasma oxidation and the resulting oxide thickness [LKS+08] [PMR+03] [Bae03] 20

3 process conditions for plasma oxidation and the resulting oxide thicknesses from literature data (first three rows) [LKS+08] [PMR+03] [Bae03] and from investigations within this thesis (fourth row); green fields mark saturation durations 51

4 estimated sputter rates for the studied materials (green fields mark verified values) (* rough estimation based on comparison with rates of other materials) 60

5 kinetic energies of Auger- and photo-electrons (for 1.5 keV excitation energy) as well as the resulting IMFP* for relevant elements in GaN; in XPS the analyzing angle of 45° has to be considered; *information depths are higher by a factor of about 3 61

6 information depth of EDX for emerging materials (calculation by the Andersen-Hasler approximation (eq. 4.3) for different primary electron energies and electron gun angles used in SEM and TEM 68

References

[ABD+96] O. Ambacher, M. S. Brandt, R. Dimitrov, T. Metzger, M. Stutzmann, R. A. Fischer, A. Miehr, A. Bergmaier, and G. Dollinger. Thermal stability and desorption of Group III nitrides prepared by metal organic chemical vapor deposition. *Journal of Vacuum Science & Technology B*, 14(6):3532–3542, 1996.

[AKBKO93] M. Asif Khan, A. Bhattarai, J. N. Kuznia, and D. T. Olson. High electron mobility transistor based on a GaN-AlxGa1-xN heterojunction. *Applied Physics Letters*, 63(9):1214–1215, 1993.

[ASA96] J. Ahman, G. Svensson, and J. Albertsson. A Reinvestigation of β-Gallium Oxide. *Acta Crystallographica Section C*, 52(6):1336–1338, Jun 1996.

[Bae03] C. Bae. *GaN-dielectric interface formation for gate dielectrics and passivation layers using remote plasma processing.* PhD thesis, North Carolina State University. 2003.

[Bal89] B. Jayant Baliga. Power semiconductor device figure of merit for high-frequency applications. *Electron Device Letters, IEEE*, 10(10):455–457, Oct 1989.

[Bar14] A.R. Barron. *Mechanism of the Metal Organic Chemical Vapor Deposition of Gallium Arsenide.* [ONLINE] available at: http://cnx.org/content/m25614/1.6/, [accessed on 21.11.2014].

[Bri08] Michael A Briere. GaN based power devices: Cost-effective revolutionary performance. *Power Electronics Europe*, (7):29–31, 2008.

[Che27] Z. Chen, L.W. Su, J.Y. Shi, X.L. Wang, C.L. Tang and P. Gao (2012). AFM Application in III-Nitride Materials and Devices, Atomic Force Microscopy - Imaging, Measuring and Manipulating Surfaces at the Atomic Scale, Dr. Victor Bellitto (Ed.), ISBN: 978-953-51-0414-8, InTech, DOI: 10.5772/37527.

[CRC+02] H W Choi, M A Rana, S J Chua, T Osipowicz, and J S Pan. Surface analysis of GaN decomposition. *Semiconductor Science and Technology*, 17(12):1223, 2002.

[CZX+00] P. Chen, R. Zhang, X.F. Xu, Y.G. Zhou, Z.Z. Chen, S.Y. Xie, W.P. Li, and Y.D. Zheng. The oxidation of gallium nitride epilayers in dry oxygen. *Applied Physics A*, 71(2):191–194, 2000.

[DFN06a] Y. Dong, R. M. Feenstra, and J. E. Northrup. Electronic states of oxidized GaN(0001) surfaces. *Applied Physics Letters*, 89(17):–, 2006.

[DFN06b] Y. Dong, R. M. Feenstra, and J. E. Northrup. Oxidized GaN(0001) surfaces studied by scanning tunneling microscopy and spectroscopy and by first-principles theory. *Journal of Vacuum Science & Technology B*, 24(4):2080–2086, 2006.

[EBW+96] N. V. Edwards, M. D. Bremser, T. W. Weeks, R. S. Kern, R. F. Davis, and D. E. Aspnes. Realtime assessment of overlayer removal on GaN, AlN, and AlGaN surfaces using spectroscopic ellipsometry. *Applied Physics Letters*, 69(14):2065–2067, 1996.

[EKN+11] Michele Esposto, Sriram Krishnamoorthy, Digbijoy N. Nath, Sanyam Bajaj, Ting-Hsiang Hung, and Siddharth Rajan. Electrical properties of atomic layer deposited aluminum oxide on gallium nitride. *Applied Physics Letters*, 99(13):–, 2011.

[Gel60] S. Geller. Crystal Structure of beta-Ga2O3. *The Journal of Chemical Physics*, 33(3):676–684, 1960.

[GMC+10] Luke Gordon, Mao-Sheng Miao, Srabanti Chowdhury, Masataka Higashiwaki, Umesh K Mishra, and Chris G Van de Walle. Distributed surface donor states and the two-dimensional electron gas at AlGaN/GaN heterojunctions. *Journal of Physics D: Applied Physics*, 43(50):505501, 2010.

[Hay10] William M Haynes. *CRC handbook of chemistry and physics.* CRC press, 2010.

[HCSM10] Masataka Higashiwaki, Srabanti Chowdhury, Brian L. Swenson, and Umesh K. Mishra. Effects of oxidation on surface chemical states and barrier height of AlGaN/GaN heterostructures. *Applied Physics Letters*, 97(22):–, 2010.

[Hen14] R. Hentschel. Influence of device geometry, buffer doping conditions and terminal potentials on the dynamic RDSon and breakdown voltage of GaN power HEMTs. Master's thesis, Technische Universität Bergakademy Freiberg. 2014.

[Hon14] Emerging Technology: SiC and GaN. School of Electronic and Electrical Engineering, Hongik University. [ONLINE] available at: http://huniv.hongik.ac.kr/∼hcha/introduction_laboverview.html, [accessed 26.11.2014].

[HPE10] P.L. Hower, S. Pendharkar, and T. Efland. Current status and future trends in silicon power devices. pages 13.1.1–13.1.4, Dec 2010.

[HTE+99] B. Heying, E. J. Tarsa, C. R. Elsass, P. Fini, S. P. DenBaars, and J. S. Speck. Dislocation mediated surface morphology of GaN. *Journal of Applied Physics*, 85(9):6470–6476, 1999.

[IFN+00] J. P. Ibbetson, P. T. Fini, K. D. Ness, S. P. DenBaars, J. S. Speck, and U. K. Mishra. Polarization effects, surface states, and the source of electrons in AlGaN/GaN heterostructure field effect transistors. *Applied Physics Letters*, 77(2):250–252, 2000.

[Jar06] A.H. Jarndal. *Large-Signal Modelling of GaN Device for High Power Amplifier Design.* PhD thesis, University of Kassel. 2006.

[JW13] Adam J. Jackson and Aron Walsh. Oxidation of GaN: An *ab initio* thermodynamic approach. *Phys. Rev. B*, 88:165201, Oct 2013.

[KBB+98] S. W. King, J. P. Barnak, M. D. Bremser, K. M. Tracy, C. Ronning, R. F. Davis, and R. J. Nemanich. Cleaning of AlN and GaN surfaces. *Journal of Applied Physics*, 84(9):5248–5260, 1998.

[KM03] Ulrich Koops and Manfred Martin. Kinetics of Oxidation Processes in the System Co/Ga studied by in situ X-Ray Diffraction. *Zeitschrift für anorganische und allgemeine Chemie*, 629(10):1688–1700, 2003.

[Kol15] Christian Koller. *Electrical Characterization of thermal gate oxides in III-N MIS-HEMTs*. 2015.

[KP15] Ryszard Korbutowicz and J. Prazmowska. *Wet thermal oxidation of GaAs and GaN*. Wroclaw University of Technology. 2010; [ONLINE] available at: http://www.intechopen.com/books/semiconductor-technologies/wet-thermal-oxidation-of-gaas-and-gan/, [accessed on 10.01.2015].

[KRL+02] M. Kočan, A. Rizzi, H. Lüth, S. Keller, and U.K. Mishra. Surface Potential at as-Grown GaN(0001) MBE Layers. *physica status solidi (b)*, 234(3):773–777, 2002.

[KVHKO91] M. Asif Khan, J. M. Van Hove, J. N. Kuznia, and D. T. Olson. High electron mobility GaN/AlxGa1xN heterostructures grown by lowpressure metalorganic chemical vapor deposition. *Applied Physics Letters*, 58(21):2408–2410, 1991.

[KWH+01] D.D. Koleske, A.E. Wickenden, R.L. Henry, J.C. Culbertson, and M.E. Twigg. GaN decomposition in H2 and N2 at MOVPE temperatures and pressures. *Journal of Crystal Growth*, 223(4):466 – 483, 2001.

[L0] Boris V L'vov. Kinetics and mechanism of thermal decomposition of GaN. *Thermochimica Acta*, 360(1):85 – 91, 2000.

[Lag14] Peter Willibald Lagger. *Physics and Characterization of the Gate Stack in Gallium Nitride based MIS-HEMTs*. PhD thesis, Vienna University of Technology, 2014.

[LKS+08] HJ Lee, SM Kang, TI Shin, JW Shur, and DH Yoon. Growth and structural properties of β-Ga2O3 thin films on GaN substrates by an oxygen plasma treatment. *J Ceram Process Res*, 9(2):180–183, 2008.

[LLLL06] L.M. Lin, Yi Luo, P.T. Lai, and Kei May Lau. Influence of oxidation and annealing temperatures on quality of Ga2O3 film grown on GaN. *Thin Solid Films*, 515(4):2111 – 2115, 2006.

[LM12] Rathnait D. Long and Paul C. McIntyre. Surface Preparation and Deposited Gate Oxides for Gallium Nitride Based Metal Oxide Semiconductor Devices. *Materials*, 5(7):1297–1335, 2012.

[LMX+06] Shen Liya, Liu Mingjian, Liu Xiaozhen, Deng Lei, and Li Bo. Multi-layered adsorption of 3Y-ZrO2 nanoparticles on polystyrene microsphere. *Materials Research Bulletin*, 41(10):1891 – 1901, 2006.

[Mar08] Hadis Markoç. *Handbook of Nitride Semiconductors and Devices.* WILEY-VCH Verlag. 2008.

[MKA+05] M.A. Mastro, O.M. Kryliouk, T.J. Anderson, A. Davydov, and A. Shapiro. Influence of polarity on GaN thermal stability. *Journal of Crystal Growth*, 274(1-2):38 – 46, 2005.

[MWVdW10] M. S. Miao, J. R. Weber, and C. G. Van de Walle. Oxidation and the origin of the two-dimensional electron gas in AlGaN/GaN heterostructures. *Journal of Applied Physics*, 107(12):–, 2010.

[New02] Dale E Newbury. Barriers to quantitative electron probe X-ray microanalysis for low voltage scanning electron microscopy. *Journal of Research - National Insitute of Standards and Technology*, 107(6):605–620, 2002.

[Nix14] R.M. Nix. *An introduction to surface chemistry.* [ONLINE] available at: http://www.chem.qmul.ac.uk/surfaces/scc/, [accessed 21.11.2014].

[NJ03] Yoshitaka Nakano and Takashi Jimbo. Interface properties of thermally oxidized n-GaN metal–oxide–semiconductor capacitors. *Applied Physics Letters*, 82(2):218–220, 2003.

[OC12] Hooi Shy Oon and Kuan Yew Cheong. Effect of oxidation temperature on physical properties of thermally grown oxide on GaN in N2O ambient. *Materials Chemistry and Physics*, 137(1):381 – 388, 2012.

[OC13] Hooi Shy Oon and KuanYew Cheong. Effect of Oxidation Time on Thermally Grown Oxide on GaN. *Journal of Materials Engineering and Performance*, 22(5):1341–1347, 2013.

[Oku06] Hajime Okumura. Present Status and Future Prospect of Widegap Semiconductor High-Power Devices. *Japanese Journal of Applied Physics*, 45(10R):7565, 2006.

[Ost07] C. Ostermaier. Interface Characterization Methods and Properties of GaN Metal-Insulator-Semiconductor Structures. Master's thesis, Kyungpook National University. 2007.

[Phi14] [ONLINE] available at: https://www.phi.com/surface-analysis-techniques/aes.html, [accessed 21.11.2014].

[PMR+03] S Pal, R Mahapatra, S.K Ray, B.R Chakraborty, S.M Shivaprasad, S.K Lahiri, and D.N Bose. Microwave plasma oxidation of gallium nitride. *Thin Solid Films*, 425(1-2):20 – 23, 2003.

[PSF98] A. Pisch and R. Schmid-Fetzer. In situ decomposition study of GaN thin films. *Journal of Crystal Growth*, 187(3–4):329 – 332, 1998.

[PST+03] A. Pakes, P. Skeldon, G.E. Thompson, J.W. Fraser, S. Moisa, G.I. Sproule, M.J. Graham, and S.B. Newcomb. Anodic oxidation of gallium nitride. *Journal of Materials Science*, 38(2):343–349, 2003.

[Rei15] Maria Reiner. *Chemical Modification and Analysis of Group-III-Nitride Surfaces*. PhD thesis, CINSat, University of Kassel, Germany, expected 2015.

[RKP+15] Maria Reiner, Christian Koller, Kurt Pekoll, Rudolf Pietschnig, and Clemens Ostermaier. Relevance of Threading Dislocations for the Thermal Oxidation of GaN (0001). In *Materials Research Society Spring Meeting*, 2015.

[ROC+03] M.A. Rana, T. Osipowicz, H.W. Choi, M.B.H. Breese, and S.J. Chua. A study of the material loss and other processes involved during annealing of GaN at growth temperatures. *Chemical Physics Letters*, 380(1–2):105 – 110, 2003.

[RRB+15] Maria Reiner, Marcus Reiss, Thorge Brünig, Lauri Knuuttila, Rudolf Pietschnig, and Clemens Ostermaier. Chemical understanding and utility of H3PO4 etching of group-III- nitrides. *physica status solidi (b)*, 2015.

[RTN+00] M. R. Ranade, F. Tessier, A. Navrotsky, V. J. Leppert, S. H. Risbud, F. J. DiSalvo, and C. M. Balkas. Enthalpy of Formation of Gallium Nitride. *The Journal of Physical Chemistry B*, 104(17):4060–4063, 2000.

[RWW+99] E.D. Readinger, S.D. Wolter, D.L. Waltemyer, J.M. Delucca, S.E. Mohney, B.I. Prenitzer, L.A. Giannuzzi, and R.J. Molnar. Wet thermal oxidation of GaN. *Journal of Electronic Materials*, 28(3):257–260, 1999.

[Vet00] R. Vetury. *Polarization Induced 2DEG in AlGaN/GaN HEMTs: On the origin, DC and transient characterization*. PhD thesis, University of California, Sainta Barbara. 2000.

[Vis11] Domenica Visalli. *Optimization of GaN-on-Si HEMTs for High Voltage Applications*. PhD thesis, Katholieke Universiteit Leuven, 2011.

[WDM+00] S.D Wolter, J.M DeLucca, S.E Mohney, R.S Kern, and C.P Kuo. An investigation into the early stages of oxide growth on gallium nitride. *Thin Solid Films*, 371(1–2):153 – 160, 2000.

[Wik14] Wikipedia. [ONLINE], http://www.wikipedia.org/, [Accessed 21.11.2014].

[WJ07] Colin Wood and Debdeep Jena. *Polarization Effects in Semiconductors: From Ab Initio Theory to Device Applications*. Springer Science & Business Media, 2007.

[WM04] JL Weyher and L Macht. Defects in wide band-gap semiconductors: selective etching and calibration by complementary methods. *The European Physical Journal Applied Physics*, 27(1-3):37–41, 2004.

[WSE+13] P. H. Weidlich, M. Schnedler, H. Eisele, U. Strauß, R. E. Dunin-Borkowski, and Ph. Ebert. Evidence of deep traps in overgrown v-shaped defects in epitaxial GaN layers. *Applied Physics Letters*, 103(6):–, 2013.

[WWG99] N. J. Watkins, G. W. Wicks, and Yongli Gao. Oxidation study of GaN using x-ray photoemission spectroscopy. *Applied Physics Letters*, 75(17):2602–2604, 1999.

[ZAIS+08] Yi Zhou, Claude Ahyi, Tamara Isaacs-Smith, Michael Bozack, Chin-Che Tin, John Williams, Minseo Park, An jen Cheng, Jung-Hyun Park, Dong-Joo Kim, Dake Wang, Edward A. Preble, Andrew Hanser, and Keith Evans. Formation, etching and electrical characterization of a thermally grown gallium oxide on the Ga-face of a bulk GaN substrate. *Solid-State Electronics*, 52(5):756 – 764, 2008.

[ZNS99] Tosja K. Zywietz, Jörg Neugebauer, and Matthias Scheffler. The adsorption of oxygen at GaN surfaces. *Applied Physics Letters*, 74(12):1695–1697, 1999.